

**Appendix G**  
**FLAC<sup>3D</sup> Local Modeling**

---



# FLAC<sup>3D</sup> Local Modeling

---

This appendix provides additional details regarding local models used to evaluate tailwall interlock pullout and wall defects within the OCSP® system. The intent of these evaluations was to determine:

- Whether the knuckle used in the OCSP® tailwall contributed significant extra pullout capacity to the tailwall as load developed on the facewall, and
- Whether defects within the existing OCSP® system represented significant additional risk to local stability during seismic loading.

Results of these analyses are summarized in Section 7.5 of the suitability study report. In the following two sections, additional details regarding the tailwall interlock pullout and local defect models and the results of each analysis are provided. These results were used to form the conclusions given in Section 7.5 of the suitability study report.

## G.1 Tailwall Interlock Pullout Model

The study of tailwall pullout was performed to address uncertainties in the PND design approach for interlock pullout resistance. The PND pull-out resistance information was considered proprietary by PND (2008), and therefore assumptions had to be made by CH2M HILL during the suitability study regarding the amount of reaction that could be developed by each tailwall. It is CH2M HILL's understanding from discussions with the Port of Anchorage (POA) and United States Army Corps of Engineers (USACE) that PND had conducted numerical analyses to show that the knuckles along the tailwall resulted in additional pullout capacity, relative to what would be developed from interface friction of backfill soil on flat steel sheet piles. Available information from PND also suggested that field tests have validated this additional reaction. Realizing this, a local numerical model was developed to investigate whether higher resistance would develop by pulling a knuckle through the backfill. The numerical modeling was conducted using FLAC<sup>3D</sup> to simulate a physical model test where the knuckle of the tailwall is pulled through granular backfill. The following subsections describe the geometry used in the model, steel and soil properties assigned to the model, the interface representation, boundary and initial conditions for the model, and the imposed loading. The final subsection summarizes results from the modeling effort.

### G.1.1 Geometry

The FLAC<sup>3D</sup> model used to investigate the influence of interlocks on pullout resistance is based on pulling connected sheet piles from a box containing soil. Specifically, the model represents a series of connected sheet pile elements 1-inch high that is pulled from a 1-inch-thick box containing soil. The numerical model allows the sheet piles to pass through openings in opposing walls in the box. The box sides facing the sheet pile elements in the model are open so that the upper and lower parts of the box can be filled with soil.

The model has the ability to apply a uniform normal stress to the surface of the soil on the open sides of the box through a device similar to an inflatable diaphragm, which is held against the two sides of the sheet pile elements. The sheet pile geometry used in the models is based on PS31 sheet pile section geometry obtained from a CAD drawing from the web site of L.B. Foster, a sheet pile supplier. Figure G-1 illustrates the sheet pile section geometry used in the pullout models. Figure G-2 shows a section view of the test device when configured to contain one full sheet pile and two half-sheets.

Three different sheet pile-interlock configurations were investigated:

- Two sheet pile halves
- One full sheet pile joined with two sheet pile halves
- Two full sheet piles with each one connected to the other and a sheet pile half

Figures G-3, G-2, and G-4 illustrate the three configurations, respectively. These configurations are subsequently referred to by the number of interlocks contained in the test specimen; that is, one, two, and three.

Because the geometry in the pullout test model contains curves and small details, an automatic mesh generation software program was used to create unstructured finite element meshes of the model that could be imported into FLAC<sup>3D</sup>. Creating the meshes in FLAC<sup>3D</sup> would have taken considerable effort using FLAC<sup>3D</sup>'s built-in structured meshing tools. Figure G-5 illustrates a mesh of approximately 350,000 tetrahedron elements and 70,000 nodes created for the two interlock models. Element sizes were graded from small sizes at the sheet pile to larger sizes at the soil boundaries opposite the sheet pile elements.

Because the depth of the upper and lower soil boxes in the model is a boundary condition that can influence the test results, it was also varied for the three sheet pile configuration models in order to investigate its effect on pullout resistance. A second set of models was created to increase the depth of the upper and lower soil boxes by 4 inches each. Table G-1 summarizes the geometry of the pullout models.

The models were run in FLAC<sup>3D</sup>'s large-strain mode, which means that element geometry is updated at each calculation step to be consistent with the accumulated displacements. In addition, stress corrections were made for element rotations. Large-strain mode was used because the pullout displacements in the test are large compared to the finite element sizes near the sheet pile.

TABLE G-1

**Summary of Pullout Model Geometry**

Number of Interlocks	Length, $l_{box}$ inches	Thickness, $t$ inches	Height, $h$		Number of Tetrahedron Elements	
			inches			
			Shallow Soil Box	Deep Soil Box	Shallow Soil Box	Deep Soil Box
One	20.7	1	14.9	22.9	240,306	258,736
Two	40.5	1	14.9	22.9	356,882	531,299
Three	60.3	1	14.9	22.9	606,697	656,226

## G.1.2 Material Models

There are multiple soil models in FLAC<sup>3D</sup> worth consideration for use in the pullout test model. However, in modeling it is generally best to begin with the simple and add complexity incrementally. This facilitates developing an understanding of the influence of particular factors. Beginning with a complex model of a system can hinder the modeling effort because it tends to flood the modeler with too much new information. Therefore, the Mohr-Coulomb (MC) elastic-plastic model was used to represent the material response of the soil. The model parameters used are listed in Table G-2.

TABLE G-2

**Material Parameters for Pullout Test**

Physical Entity	Material Model	Parameters
Soil	Mohr-Coulomb	$G=1540$ psi $K=3330$ psi $\phi=32^\circ$ $\psi=0^\circ$
Steel	Rigid	N/A
Soil/Steel Interface	Mohr-Coulomb	$k_n=2.5 \times 10^5$ lbf/in <sup>3</sup> $k_s=2.5 \times 10^6$ lbf/in <sup>3</sup> $\psi=12^\circ$

Although using steel for the sheet pile elements is the obvious modeling choice for a physical pullout test, the decision for numerical modeling requires more careful consideration. The choice of material model for the sheet piles has ramifications in numerical modeling, particularly with FLAC<sup>3D</sup>, which uses an explicit solution algorithm.

Using actual steel elastic material parameters for the sheet pile elements in the FLAC<sup>3D</sup> model would result in dramatically increased run-times because of the large stiffness contrast between the soil and the steel.

Models with large stiffness contrasts in general converge much slower than models with modest stiffness contrasts. There is not a precise definition of “modest stiffness contrast,” but generally it would involve ratios of maximum to minimum stiffness of 10 or less. The ratio of the elastic stiffness of steel to soil is much greater than this; therefore, because the steel is much stiffer than the soil, the sheet pile was modeled as a rigid material. This is a reasonable choice because the deformations of the steel sample under the test loads are several orders of magnitude less than the soil deformations.

### G.1.3 Interface Model

The interface between the soil and the steel sheet pile also requires consideration. One modeling choice is to connect the soil elements directly to the steel sheet pile surface. This corresponds to an assumption of a no-slip condition between the steel and soil, and experience indicates that slip does occur when soil is against a structural steel surface. In design, this interface is generally assigned a friction factor corresponding to a friction angle that is one-half to two-thirds of the soil. An interface friction angle of 12 degrees, which is a little less than one-half of the soil friction angle for the backfill material, was used for most of the model tests. However, a few models were run with different values to study the effect of this parameter on the model results. Normal and shear stiffness values are also required in the FLAC<sup>3D</sup> interface material model. Unlike material parameters for solid constitutive models, the selection of interface stiffness values is more about achieving a computational goal; for example, limiting penetration across the interface. The normal stiffness value was set to about 10 times the smallest apparent normal stiffness of the adjoining soil elements in accordance with recommendations in the FLAC<sup>3D</sup> User’s Guide. The shear stiffness value was set to one-tenth of the normal stiffness because the interface should be more compliant in shear.

One issue was identified during modeling regarding the soil-steel interface. During initial model development, interface elements were attached to the steel sheet pile on the element faces adjoining the soil. In FLAC<sup>3D</sup> interface elements are said to be one-sided, which means that they work by detecting penetration of neighboring elements into the element faces that they are attached to. Figure G-6 illustrates a zoomed view of the deformations at an interlock joint. It is apparent that some of the soil elements are penetrating quite far through the interface.

Examination of the results indicates that this penetration is simply not detected by the interface elements. This issue seemed to be limited to areas of curvature on the interface and sharp corners. Based on commentary in the FLAC<sup>3D</sup> User’s Guide, a second opposing interface was added to the faces of the soil elements adjoining the steel elements. This effectively solved the issue, as illustrated in Figure G-7, with the exception of some spurious results at the sharp interior corner in the interlock connection. However, because the elements involved are small, the forces involved are small, and the pullout force versus displacement relationship became much smoother after implementing the opposing interface elements, this approach was adopted.

### G.1.4 Boundary and Initial Conditions

Boundary conditions are typically an important consideration in numerical modeling. One aspect of boundary conditions is the size of the test specimen, which was previously discussed under the heading Geometry. Also, the modeling approach taken was to view the pullout test as an adaptation of a direct shear test used in soil mechanics. Therefore, the sides of the soil box transverse to the sheet pile sample were modeled as being held by frictionless, rigid walls similar to a direct shear box. A confining stress was imposed on the soil by applying a uniform normal stress to the soil surface of the upper and lower soil boxes. These boundary conditions are illustrated in Figure G-8. In addition, the sheet pile and soil are sandwiched between two parallel frictionless rigid surfaces, so no out-of-plane movements occur. In other words, the pullout test takes place under plane strain conditions.

A normal stress of 10 psi was applied to the upper and lower soil boxes for all model tests; that is,  $\sigma_{yy}=10$  psi. The sand was initialized to at-rest conditions with the normal stress on the two orthogonal planes set to 5 psi; that is,

$\sigma_{xx} = \sigma_{zz} = 5$  psi. These conditions roughly correspond to stress conditions 15 feet below the ground surface if the groundwater table is at least 10 feet below the ground surface.

Because the sheet pile sample is pulled out through an opening in the left-hand wall of the device, it is difficult to envision any practical variation of the boundary condition for the left wall of the pullout device box other than to increase the distance from the nearby interlock joint. On the other hand, variations on the boundary conditions on the upper and lower soil surfaces and the right-hand side of the device are more feasible. For instance, a confining stress could be applied through rigid platens resting on the soil. Similarly, a uniform normal stress can be applied to the right-hand side of the soil boxes.

Changing the right-hand soil box boundary condition to an applied normal stress from a displacement condition (that is, smooth frictionless rigid wall) is easy to implement. On the other hand, modeling the confining load as being applied through rigid platens is more difficult to implement. Therefore, several models were run with the right side boundary condition changed to an applied normal stress of 5 psi. This was also done because the model results with the rigid right side boundary condition indicated loads were being transmitted to the right-hand soil box side during the test; that is, the reaction on the right wall of the soil box decreased during the pullout test.

### G.1.5 Loading

The pullout test was conducted by smoothly accelerating the steel sheet pile elements to a constant velocity and monitoring the reaction forces on the mesh. Through several trials it was found that a constant velocity of  $2 \times 10^{-6}$  inches/step kept the unbalanced force ratio generally at or below  $1 \times 10^{-4}$  during the test. Because FLAC<sup>3D</sup> uses an explicit solution algorithm, it is important to keep the unbalanced force ratio to a small value when material models with plasticity are present in the model as in this case. Otherwise, the transient stress waves transmitted through the model during solution could cause spurious solutions to develop.

The acceleration of the sheet pile to the constant test velocity was controlled by the following interpolation function based on the trigonometric sine function:

$$v = \frac{v_{constant}}{2} \left[ \sin \left( \left( \frac{step - step_0}{N_{steps}} \right) \cdot \pi - \frac{\pi}{2} \right) + 1 \right]$$

where:

*step* – is the current FLAC<sup>3D</sup> calculation step number

*step<sub>0</sub>* – is the calculation step number acceleration begins at

*N<sub>step</sub>* – is the user-specified number of steps to accelerate from 0 to *v<sub>constant</sub>* over

A similar function based on the cosine function is used to decelerate the sheet pile elements to zero velocity; that is, stop pulling. The models were generally set to pull the sheet pile out in 0.1-inch increments and test for equilibrium at the stop points.

### G.1.6 Results

One motivation for developing one, two, and three interlock pullout models was to examine the influence of sample length on pullout resistance. Another goal was to examine the influence of the boundary condition at the left side of the soil box; that is, a rigid frictionless wall. Figure G-9 illustrates the results from the one, two, and three interlock models with a 12-degree soil-to-steel interface friction angle.

Several things are apparent from Figure G-9. First, the ultimate pullout resistance of the single interlock model is between the theoretical ultimate pullout values of a rectangular bar having the same length and width as the sheet pile samples for interface friction angles of 12 degrees and 32 degrees. The theoretical pullout resistance of a rectangular bar is the product of the surface area of the bar times the normal stress, 10 psi, times the tangent of the interface friction angle times 2, because there are two sides in contact with the sand. The value of 12 degrees corresponds to the actual interface element shear strength, and the value of 32 degrees corresponds to the soil friction angle. Second, the increase in ultimate pullout resistance from the one interlock model to the two

interlock model is slightly smaller than a value equal to the increase in model length (one sheet pile width) times the friction force associated with 32 degrees. Third, the increase in ultimate pullout resistance from the two interlock model to the three interlock model is very small. Figure G-10, which shows the displacement vectors at an approximate test displacement of 0.2-inch, suggests why the increase in pullout resistance between the two and three interlock models is so small. It is apparent that a significant amount of soil is riding along with the third interlock.

Figure G-11 illustrates pullout results from the single interlock model for various values of the soil-to-steel interface friction angle. Although the interface friction angle influences the results, it is readily apparent that it is not a controlling factor. Specifically, the ultimate pullout resistance with an interface friction angle of 6 degrees is much larger than the theoretical value of a rectangular bar's pullout resistance with the same interface friction. The increase in pullout resistance above the theoretical pullout resistance with low interface friction angles is a result of the interlocks engaging soil. Similarly, although the ultimate pullout resistance with an interface friction angle of 30 degrees is appreciably larger than with 6 degrees, it is still less than the theoretical pullout resistance on a rectangular bar with an interface friction angle of 32 degrees.

The results from several pullout tests with the two-interlock model are shown Figure G-12. The models presented represent several different boundary condition cases, including shallow and deep soil boxes and using a stress boundary rather than displacement boundary on the right side of the soil box. Figure G-13 presents similar results obtained with the one-interlock model. As with the two-interlock model, the one interlock model results show that although the boundary conditions influence the initial portion of the pullout displacement curve, the ultimate pullout resistance is essentially the same for the models.

Figure G-14 shows a deformed mesh and displacement contours from a two interlock model with the stress boundary condition on the right side of a deep soil box. The displacements, which are magnified by a factor of 10 in the figure, show the soil piling up against the left side of the model, which is fixed against displacement. This illustration highlights the significant role that the left side boundary condition has on the model test results. The majority of the reaction on the soil mass to the applied pullout load occurs on this boundary for cases in which a displacement boundary condition is used on the right side of the soil box. All of the reaction occurs on this boundary for the cases in which a stress boundary condition is used on the right side of the soil box. This observation, in conjunction with the effect of soil box depth on results, as illustrated in Figures G-12 and G-13, suggests that the soil box depth should be greater than the sheet pile sample length.

## G.2 Local Defect Model

The second local model was developed to determine the potential effects of existing defects in the OCSP® facewall and tailwall. As discussed in Section 8 of this suitability study report, a number of construction defects occurred during installation of the sheet piles. These defects involved the sheets coming out of interlock during installation, caused by either driving on rock or by the effects of lateral dike loads on the sheets during driving. Gaps were identified in the facewall by divers during underwater inspections, and there were concerns that similar conditions could exist along the tailwall. These defects were identified as a potential source of further “unzipping” as the sheet piles reacted to additional loads from final dredging and during a seismic event. At the facewall, the unzipping would likely result in more loss of fill behind the wall, and if the amount of unzipping was large, could result in failure of the cell. For the tailwall unzipping could result in more load being transferred from the facewall to shorter intact sections of the tailwall, causing greater potential for complete unzipping as stresses progressively became higher. The following subsections discuss the geometry considered in the models, the method of modeling the OCSP® system, steel and soil properties used in the model, and the results of the evaluation. As part of this discussion, the differences between the local model used to evaluate these defects and the global model described in Sections 7.2 through 7.4 of the suitability study report are also summarized.

### G.2.1 Geometry

It is possible to identify many different scenarios of a facewall or tailwall defect based on differences in OCSP® geometry, subsurface conditions, and so on for the project. It is not practical to attempt to model all of the

different scenarios because this could easily lead to many hundreds of model instances and a modeling effort that might take a year or more to complete. Therefore, the approach taken was to use modeling to analyze a basic problem and develop a better fundamental understanding of system performance. This approach provides a better basis for making engineering judgments when addressing the issues.

Two basic models with different geometry were developed. The first model serves as a reference or baseline model for the second model. The first model represents an infinitely long OCSP® wall at the maximum design section without any defects. Because of the symmetry of an infinitely long wall, this model is limited to two half cells and one tailwall, the same as the previously presented FLAC<sup>3D</sup> primary model. This first model is referred to by the nomenclature “2h” as shorthand for “two half-cell” in this section. Figure G-15 illustrates the FLAC<sup>3D</sup> mesh for the 2h model. The 2h model contains 65,400 zones (soil elements) and 5,656 structural elements.

The second model is used to model isolated defects in a facewall and tailwall. Because the defects are intended to be isolated, the model must encompass a greater reach of the wall than the reference model; however, a large model means increased model run time and memory requirements. Therefore, the need to model a larger reach of wall must be balanced with the need to obtain a model that does not exceed the memory capacity of the software and modeling platform and runs in a reasonable period of time. In this case, this balance meant limiting the second model to two cell widths; that is, a width of 55 feet. The second model is arranged so that one complete cell and two half cells with two tailwalls are modeled. The nomenclature “1w+2h” is used as shorthand for “one whole cell and two half-cells” to identify the second model in this section. Figure G-16 illustrates the FLAC<sup>3D</sup> mesh for the 1w+2h model, which contains 130,800 zones (soil elements) and 11,344 structural elements.

Because the focus of the local defect modeling effort is on OCSP® stresses, emphasis was placed on attaining a high resolution of the numerical model mesh in the vicinity of the OCSP® face and tailwalls. There are seventeen PS31 steel sheet piles in the facewall of each of the ±27-foot-wide cells. The aspect ratio of elements influences the accuracy of the numerical solution and a hexahedron element with height to width and width to depth ratio of 1 provides the most accurate solution. Therefore, in order to maintain an aspect ratio as close to 1 as possible, an element width slightly less than one PS31 sheet was used in order to divide each whole cell into 16 elements and each half cell into 8 elements.

Maintaining this mesh resolution throughout the model required many elements and thus quickly escalated run time and memory requirements. Therefore, the mesh size away from the wall was increased. FLAC<sup>3D</sup> allows unconfining meshes (that is, meshes with different element sizes) to be attached together along common planar boundaries. The gridpoints (nodes) of the finer mesh are slaved to the displacements of the coarser mesh along the common boundary. This slaving works best when the coarse and fine meshes are related by an integer multiple of elements along each boundary segment. In the 2h and 1w+2h models, coarse meshes with element sizes double that of the finer mesh around the OCSP® bulkhead were attached between the inner finer mesh and the model boundaries.

## G.2.2 OCSP® System

The facewall and tailwall were modeled using three-noded, flat membrane type plate structural shell elements. The membrane elements have four degrees of freedom (DOF) at each node, three of which are translational and one is an in-plane (also referred to as drilling) rotation, and use a stiffness formulation known as constant strain triangle hybrid stress. The element formulations in FLAC<sup>3D</sup> allow isotropic, orthotropic, or anisotropic elastic material response.

As previously described in this section, structural elements in FLAC<sup>3D</sup> interact with the three-dimensional continuum mesh via linkages at the structural element nodes to the zones. The linkages are created automatically for various classes of structural elements. The tailwall is modeled with the geogrid class of elements for which the structural nodes are slaved to the movements of the continuum mesh in the direction normal to the face of the geogrid elements; however, in the transverse or shearing direction, a coupling shear spring allows relative movement between the geogrid elements and the continuum mesh. The shear stresses that develop in the coupling spring are limited by a Coulomb-type strength law with cohesion and friction. The effective normal

stresses in the adjacent three-dimensional soil zones are used with the assigned link friction angle and cohesion to calculate the frictional strength component of each spring. The shear spring parameters for the tailwall in the local defect models are given in Table G-3.

TABLE G-3  
Structural Element Linkage Parameters for Local Defect Models

Parameter	Name	Value
$k_n$	Normal stiffness	$2 \times 10^7$ lbf/ft <sup>3</sup>
$k_s$	Shear stiffness	$2 \times 10^5$ lbf/ft <sup>3</sup>
$c$	Cohesion	0
$\delta$	Friction angle	30°
$c_{res}$	Residual cohesion	0
$N_{cut}$	Tension cutoff strength	0

The normal stiffness of the linkage springs was selected so that the normal movements between the soil zones and the structural elements is small and insignificant relative to the soil movements, but not so stiff as to create a large stiffness contrast in the model that would adversely affect convergence. The shear stiffness was set to a fraction of the normal stiffness in order to have more compliance in the shear direction, similar to a real interface. A friction angle of 30 degrees was used for shear strength of the interface because the pullout model results described in Section G.1 suggest it is reasonable to use a friction angle slightly less than the granular backfill's 36-degree friction angle.

The facewall is modeled using the liner element class. For the tailwall, the structural element is a 3-noded membrane element. The embedded liner option is used, which means that each liner element can interact with soil elements on each face of the element. The soil elements on either side of an embedded liner element are not joined to the elements on the opposite side. On each side of the liner, normal and shear springs couple the liner to the adjoining soil elements. The shear spring formulation for the liner element is the same as for the geogrid element except the normal stress for the Coulomb-type shear strength equation comes from the normal spring response.

In FLAC<sup>3D</sup>, structures composed of different structural element classes do not interact with each other unless linkages are made between the structural nodes. In the local defect model, linkages are made at the nodes of the facewall and tailwall that lie on the vertical line corresponding to the wye connection in the physical OCSP<sup>®</sup> system. In the local defect model, the linkages made are to rigidly slave the facewall nodes to the tailwall geogrid nodes at the wye location in the two transverse translational DOF in the horizontal plane. However, in the vertical direction the nodes are allowed to move independently. This corresponds to an assumption of a sheet pile interlock that has no slack and that is also perfectly smooth; that is, offers no frictional resistance to sliding. This condition is analogous to a sliding hinge. The alternative would have been to rigidly slave the two nodes in the vertical direction, but this was not done because this would correspond essentially to a fixed hinge. Because membrane type shell elements, which only utilize translation degrees of freedom and an in-plane rotation, were used, the hinge action is insignificant to the model behavior. As often happens in numerical modeling, the behavior of the real system lies between the two bounding cases available in the numerical model. In these situations, a choice must be made to use one of the bounding cases or to create two models and judge where the real system response is relative to the two bounding cases.

The discussion about the wye-connection interlock is related to the issue of how to model all of the interlocks in the OCSP<sup>®</sup> system. An actual interlock connection between sheet piles is characterized by several important mechanical characteristics. First, the opposing “finger-and-thumb” of two sheet piles that interlock do not fit perfectly; therefore, some slack must be taken up before tension or compression can be transmitted across the

connection. Also, because bearing surfaces in the interlock become larger at the points of contact when the interlock forces increase as a result of elastic and inelastic deformation at the contact, the force-displacement relationship of the interlock stiffens as the force increases. The ability of the finger and thumb to bend also contributes to compliance of the interlock. The second important characteristic of a sheet pile interlock is for friction along the points of contact to resist shearing/sliding action on the interlock; that is, one sheet moving up or down relative to the other.

The wye connection is the only interlock in the OCSF<sup>®</sup> system that is directly modeled with a mechanism in the local defect model. It is easy to look at a visualization of the FLAC<sup>3D</sup> meshes and misinterpret the columns of structural elements in the facewall and tailwall as representing individual sheet piles. However, this is not the case and the elements and nodes on the facewalls and tailwall represent a discretization of continuous steel plate structures. It would obviously be desirable to directly model all the interlocks, and some effort was expended on several concepts for how to do this using the built-in link mechanisms augmented by some customizations with FLAC<sup>3D</sup>'s built-in programming language. However, several obstacles were encountered that could not be overcome in the time available. Therefore, an indirect means of modeling the effect of interlocks on sheet pile structures was used.

The indirect means of modeling interlocks is to use an orthotropic elastic material model instead of an isotropic linear elastic material model for the structural elements. There are two components to this indirect approach. The first is to use the material parameters to reduce the shear stiffness of the assemblage of structural elements comprising a tailwall or facewall to more closely resemble the shear stiffness of an assemblage of discrete sheet piles with interlocks of limited shear strength, instead of a continuous sheet of steel. The orthotropic material stiffness matrix was set equal to the isotropic material stiffness matrix with adjustments to two terms. The isotropic material stiffness matrix for steel ( $E=29 \times 10^6$  psi,  $\nu=0.25$ ) is:

$$\begin{bmatrix} c_{11} & c_{12} & c_{13} \\ c_{12} & c_{22} & c_{23} \\ c_{13} & c_{23} & c_{33} \end{bmatrix} = \begin{bmatrix} \frac{E}{1-\nu^2} & \nu \left( \frac{E}{1-\nu^2} \right) & 0 \\ \nu \left( \frac{E}{1-\nu^2} \right) & \frac{E}{1-\nu^2} & 0 \\ 0 & 0 & \frac{E}{2(1+\nu)} \end{bmatrix} = \begin{bmatrix} 4.54 & 1.14 & 0 \\ 1.14 & 4.54 & 0 \\ 0 & 0 & 1.70 \end{bmatrix} \times 10^9 psf$$

where:

$$\{\sigma\} = [E]\{\varepsilon\} = \begin{Bmatrix} \sigma_x \\ \sigma_y \\ \tau_{xy} \end{Bmatrix} = \begin{bmatrix} c_{11} & c_{12} & c_{13} \\ c_{12} & c_{22} & c_{23} \\ c_{13} & c_{23} & c_{33} \end{bmatrix} \begin{Bmatrix} \varepsilon_x \\ \varepsilon_y \\ \gamma_{xy} \end{Bmatrix}$$

The coupling term between the vertical and horizontal normal strains and stresses and the shear stiffness constant were each reduced by a factor of 0.01. Therefore, the orthotropic material stiffness matrix used is:

$$\begin{bmatrix} 4.54 & 0.01 & 0 \\ 0.01 & 4.54 & 0 \\ 0 & 0 & 0.017 \end{bmatrix} \times 10^9 psf$$

The second component of using the material model of the tailwall and facewall is to reduce the stiffness matrix term relating lateral strain,  $\varepsilon_x$ , to lateral stress,  $\varepsilon_x$ . Previous investigators using finite element methods to model cellular cofferdam structures have determined that reducing the stiffness in the lateral direction by a factor of 1/100 to 1/30 yields results that are reasonably close to earth pressures and deformations observed when filling circular cofferdam cells. Because the goal of the local defect modeling is to understand the impact of defects, it is sufficient to examine differences in the models with and without defects. Therefore, the values from any one model are less significant than the difference in values with another model that is identical in all respects except for the presence of a defect. This means that factors such as interlock compliance, which would essentially equally affect the models, can be omitted, while recognizing that this will affect the total displacements and stresses more than the differentials between the models. Consequently, a reduction factor was not used for the defect models. This was judged to be a reasonable representation of the system after backfilling is complete when other loads such as dredging occur, because the slack would mostly be taken up during filling.

## G.2.3 Material Models

Three soil materials are used in the local defect models. These are BCF, silt sediments, and granular fill. The models for these materials correspond to those used for the as-designed evaluation of the primary model described in Section 7.2 of the report. One exception to this is that a stress-dependent bulk modulus is used for the granular backfill. The bulk modulus formulation is:

$$K = K_b \cdot p_{atm} \cdot \left( \frac{\sigma'_3}{p_{atm}} \right)^m$$

where:

- $K$  – the bulk modulus
- $K_b$  – the bulk modulus number
- $m$  – the bulk modulus exponent
- $p_{atm}$  – standard atmospheric pressure
- $\sigma'_3$  – the effective minor principal normal stress

A bulk modulus number of 75 and a bulk modulus exponent of 0.15 are used based on typical values for sands and gravels published for the Duncan and Chang hyperbolic soil model. A Poisson's ratio of 0.3 is used for the granular backfill consistent with the as-designed evaluation material parameters. The bulk modulus and shear modulus of the granular backfill is updated after each model stage, which are described below. The stress-dependent bulk modulus was used for the granular backfill because the stresses in, and hence the stiffness of, the backfill varies appreciably during backfill as the backfill depth increases.

The short-term undrained strength parameters described in Section 7.3 of the report were used for the BCF.

## G.2.4 Model Stages

The 2h and 1w+2h models are subject to a set of model stages that represent construction of the OCSP® system. The following list describes the model stages.

1. Initial Conditions – begin with silt layer and BCF in place with water level at zero. Initialize stresses in silt and BCF to  $K_0=1$  conditions and apply gravity loads, pore pressures, and a surface pressure on top of the submerged soil from weight of water above the soil surface.
2. Dredge to elevation -51 feet along the alignment of the bulkhead facewall and backfill with granular backfill.
3. Backfill the OCSP® system from elevation -30 feet to +27 feet in nine equal increments; that is, horizontally uniform lifts. Each fill increment is applied in two steps. First, a surcharge to represent the weight of the new fill lift and any water surcharge is applied to the soil surface behind the facewall. Next, the soil elements in the new fill are activated and the adjacent structural elements representing the facewall and tailwalls are created.
4. Raise the water level on the landside of the bulkhead to elevation +20 feet from zero feet in five equal increments. This raised water level acts on the retained fill in the OCSP® structure in the model from elevation -51 to +20.
5. Backfill the OCSP® structure from +27 to +30 feet in one increment in the same fashion as described in item 3.
6. Excavate soil in front of bulkhead from elevation -30 feet to -51 feet in seven equal increments.

It is noted that the incremental construction of the model OCSP® structure during backfilling described in item 3 above means that the model's OCSP® structure stiffness increases during backfilling. Although this stiffness increase is not precisely the same as what happens in the real system, it is qualitatively similar to the stiffening that occurs when the interlocks tighten during backfilling. In addition, this incremental construction approach requires a correction to the raw wall displacements obtained from this FLAC<sup>3D</sup> model. Specifically, the

displacement of any inactive gridpoint or structural node is zero until a connected zone or structural element is active. Therefore, when gridpoints and nodes are activated during the model construction, their displacements are zero at that time and do not reflect the movements that have already taken place. For example, when the last few elements at the top of the OCSP® walls are activated in the model, their displacement is zero while the elements below have non-zero displacement.

## G.2.5 Summary of Models Analyzed

Two series of models of the defect were analyzed. The first is referred to as the 2h model. The 2h models were developed for two purposes. The primary purpose of the 2h models was to obtain a reference model containing no wall defect to compare the defect model results against. The second purpose was to perform some parametric studies of the model with the goal of obtaining insight into the behaviors of the model and actual OCSP® structure. The second models were referred to as the 1w+2h model. The 1w+2h geometry models were used to investigate the effect of sheet pile defects on the system.

### G.2.5.1 2h Models

The 2h models can be categorized as a base case model, structural parameter models, and backfill parameter models. There is one base case model, which was created before any of the other models. This model represented an initial best estimate set of parameters for the reference model. The local defect models were developed directly from the 2h model base case and differ from it only by the specific wall defect included in the model.

The structural parameter models are used to examine the influence of several structural parameters. The parameters examined include:

- The c11 term of the material stiffness matrix was reduced to 1/10 of its value in the base case. The material coordinate system for the structural element was set in the FLAC3D models to be horizontal, and therefore c11 and the element thickness determine the hoop stiffness in the walls. Reducing c11 was an approximate means to investigate the influence of sheet pile interlock compliance. It was noted earlier that previous investigators of cellular cofferdam structures have found that reducing the hoop stiffness of shell elements by 1/30 to 1/100 resulted in better agreement between finite element analysis and structure measurements.
- The c33 term of the material stiffness matrix, which relates in-plane shear stress to shear strain, was increased by a factor of 10 from its value in the base case. As noted earlier, the base case used a c33 value equal to 1/100 of the value for an isotropic steel plate of the same thickness as a P32 sheet pile's web. This was an approximation made to reduce the tailwall assembly's capacity for in-plane shear to approximate the effect of interlocks, which can slip, in an actual sheet pile tailwall.
- Another parameter examined was the boundary conditions at the wye connection, that is, the connection of the facewall to tailwall. In the base case model the structural node from a facewall assembly is constrained to match the lateral movement of a corresponding structural node from the tailwall, while remaining independent in the global vertical direction. This is representative of a perfectly fit interlock with no slack and no friction that can freely rotate about the interlock axis and slide along it as well. Coupling the two nodes in the vertical direction provided an opportunity to compare with another bounding case, that is, a frictionless hinge.
- The influence of the tailwall length was examined by creating a model with a tailwall 6 feet longer than the base case.
- The influence of the shear coupling spring stiffness,  $k_s$ , of the geogrid elements used to model the tailwall was investigated by varying this parameter by factors of 0.1 and 10.
- The influence of the BCF shear strength was examined by creating a couple of parametric cases which used the long-term BCF undrained shear strength parameters during dredging.

The backfill parameter models are used to examine the influence of several backfill parameters. The parameters examined include:

- Backfill angle of internal friction,  $\phi$ , and interface friction angle,  $\delta$ , between backfill and structural elements representing sheet pile walls. The base case used  $\phi=36$  degrees and  $\delta=30$  degrees, which was found to be somewhat conservative in light of additional soils investigation and the interlock pullout model. Therefore, a model was developed with  $\phi= \delta=40$  degrees.
- The method of modeling the backfilling process implemented in the local models involves initializing the vertical and horizontal stresses in each new backfill layer based on the backfill density and a user-defined  $K_0$  parameter, which gives the initial horizontal stress in a new fill layer as a fraction of the vertical stress. The base case used a  $K_0$  value of 0.5, and  $K_0$  was varied to 0.35 in a parameter model in order to be more consistent with a backfill internal friction angle of 40 degrees and assess the parameter's effect on the model.
- The influence of the backfill stiffness was examined by increasing the bulk modulus number,  $K_b$ , of the backfill from 75 to 125.

In addition, another variation of the base case model was created to approximate the effects of an earthquake. Because of the mesh refinement of the 2h and 1w+2h models, the model run times for dynamic simulation of earthquakes with these models would be many times the already long run times of the primary mode. Therefore, a simplified static load case was created to approximate an earthquake's effect on the wall. It was assumed that the effects of an earthquake could be represented as a horizontal body force acting on the active earth pressure zone behind the facewall. This force was applied as a unique load case after dredging was completed to elevation -42.2 in the model. The undrained strength parameters for the BCF were changed to the long-term condition parameters prior to applying the horizontal body force.

### G.2.5.2 1w+2h Models

Models with defects in the facewall and tailwall were analyzed. The basic defect considered was the loss of interlock between two adjacent sheets during installation. The most likely interlock defect in an OCSP® structure is the loss of interlock during installation. The interlock between piles can be lost when a pile strays from alignment during installation and pulls away from the interlock. This construction defect occurs at the bottom of a wall.

There are two practical means to model an interlock defect in the FLAC<sup>3D</sup> models. The first is to delete a column of elements at the bottom of a wall up to the origin of the defect. This method is called the "notch" method in this report. The second way to model an interlock defect is to break the element connectivity between the structural shell elements in a wall assembly along a vertical line of nodes. This is achieved by creating a line of duplicate structural nodes at the defect location and then connecting the elements on each side of the defect to the nodes on that side of the defect. This second method of defect modeling is called the "tear" method in this report. The following paragraphs describe specific facewall and tailwall defect models.

Two facewall defect models were analyzed. The first represented a defect at the centerline of a cell from the wall tip up to the final dredge level of -51 feet by deleting a notch of elements at the centerline of one of the half cells in the 1w+2h model. The second defect model was of a defect extending from the wall tip up to elevation -30, that is, about the original seafloor in the model. This defect was modeled using the "tear" method at the centerline of the whole cell in the 1w+2h model.

Five tailwall defect models were analyzed. Defects at two different locations with respect to distance from the wye connector were modeled. Four defects were modeled at a distance of 9 feet from the wye. Two of these defects were modeled as "notch" defects with one extending up to elevation -47 feet and the second extending up to elevation -30 feet. The remaining two defects at this location were modeled using the "tear" method. One of these defects extended up to elevation -30 feet, and the other extended up to elevation -40 feet. The fifth defect model used the "notch" method to model a defect extending up to elevation -30 feet at a location about 40 feet from the wye.

The vertical sides of the FLAC<sup>3D</sup> models are planes of symmetry and have boundary conditions consistent with imposing symmetry on the model, for example, gridpoints and nodes on these planes can only move in-plane. Therefore, one would obtain the same results if a plane of symmetry was removed and a mirror image of the model was placed on the adjoining side. Consequently, the 2h model behaves as a slice of an infinitely long OCSP<sup>®</sup> structure for which every cell has identical geometry and materials. Something similar occurs with the 1w+2h models. Each of these defect models behaves as a slice from an infinitely long OCSP<sup>®</sup> structure that has regularly repeating defects. The tailwall defect model behaves as a slice from an infinitely long OCSP<sup>®</sup> structure in which the defect is present once every third tailwall. The model with the facewall defect in the whole cell represents an infinitely long OCSP<sup>®</sup> structure with a facewall defect in every other cell. The model with the facewall defect at the centerline of one of the half-cells represents a structure with a defect once every fourth cell. This means that the models will yield a larger response than a single defect in a long OCSP<sup>®</sup> structure. One could create additional models, say 2w+2h and 3w+2h, and compare results with the 1w+2h model to establish how increasing the defect spacing affects the results. However, this was not practical because of the long model run times and memory requirements.

A variation of the tailwall tear defect model was also created to approximate the effects of an earthquake with a pseudo-static load approximation in the same fashion as was done for the 2h model.

## G.2.6 Differences between Primary and Local FLAC<sup>3D</sup> Models

There are a number of differences between the primary and local FLAC<sup>3D</sup> models. These differences are described and discussed here in order to aid the reader in any comparisons of results from the local and primary models. The major differences between the two models include:

1. **Model Extents.** The local model's extents are smaller than the primary model's. The dimensions of the mesh for the primary model of a slice of the wall system encompassing one tailwall and two half-cells are 689 feet long, 27.5 feet wide, and 180 feet tall. The dimensions of the mesh for the local two half-cell model are 162.5 feet long, 27.5 feet wide, and 131 feet tall. The primary model spans elevations +35 to -150 feet, while the local model spans elevations +30 feet to -101 feet. The landside length of the primary model is 492 feet, while the landside length of the local model is 103 feet.
2. **Mesh Refinement.** The local model uses smaller elements than the primary model and consists of a fine mesh near the OCSP<sup>®</sup> facewall surrounded by a coarser mesh region that extends to the model's landside, seaside, and base boundaries. The two half-cell local model contains 65,400 hexahedron soil zones, which range in volume from about 4 ft<sup>3</sup> for the fine mesh portion to 40 ft<sup>3</sup> for the coarse mesh portion. All of the zones in the local model have aspect ratios between 0.8 and 1.0. Aspect ratio is the ratio of the shortest side of a hexahedron element to its longest side. The primary model contains 8,850 hexahedron soil zones, which range in volume from about 12 ft<sup>3</sup> to 521 ft<sup>3</sup> with volumes generally greater than 200 ft<sup>3</sup> with aspect ratios varying from 0.2 to 1.0 and typically about 0.5. The local model utilizes 5,656 structural shell-type elements to model the facewall and tailwall, while the primary model utilizes 516 elements.
3. **Tailwall Geometry.** The primary models closely follow the actual tailwall design and as-built layouts and profiles. The local model uses a simplified tailwall geometry in which the tailwall extends 80 feet back from the wye connector and spans from the top to bottom of the facewall (elevations +30 to -61 in the local model) within the first 10 feet and then elevations +24 to -45 feet thereafter.
4. **Modeling of OCSP<sup>®</sup> Construction.** There are two main differences in the staged modeling of the construction of the OCSP<sup>®</sup> system between the local and primary models. One difference is that the staged construction of the construction dike and backlands fill is modeled in the primary model. In contrast, the landside fill behind the OCSP<sup>®</sup> face is built in 10 uniform horizontal layers. The second difference is that the structural elements representing the portion of the OCSP<sup>®</sup> structure above the seafloor are all activated prior to the modeling of the construction dike and backlands fill in the primary model. In the local model, the OCSP<sup>®</sup> structure is built in 10 increments with the backfill above the seafloor. Consequently, unlike the primary model, the top

“layers” of structural elements are not subject to the loads and deformations that occur from filling below each layer.

5. **Structural Element Types.** Both models use FLAC<sup>3D</sup> structural elements called geogrid elements for the tailwall and liner elements for the facewall. Each element type comprises a shell-type finite element and default attachments between the shell-type element and adjacent 3D zones. The shell-type finite element in a geogrid or liner element may be selected from one of five available shell-type elements, but the attachment conditions are determined by the selection of a geogrid or liner. In the primary model, shell-type elements combining three-dimensional bending and plane stress using a Discrete Kirchoff Triangle, and Hybrid Constant Stress Triangle formulation are used for the geogrid and liner elements. In the local model, shell-type elements using only the Hybrid Constant Stress Triangle plane stress formulation are used for the geogrid and liner elements. Therefore, the geogrid and liner elements in the local model are only capable of membrane action, while the elements in the primary model also include 3D bending action.
6. **Material Models.** The main material model difference between the local and primary models is the stiffness of the OCSP<sup>®</sup> backfill material. In the primary model, the shear and bulk moduli of all fill materials are set to constant values once they are activated. In the local model, the stress-dependent formulation described previously in this subsection is used.
7. **BCF Strength.** The 2h base case and all the 1w+2h defect models use the short-term undrained BCF strength parameters throughout the model stages, unless otherwise noted. The primary model uses the short-term and the long-term undrained strength parameters for the BCF after the wall is backfilled, depending on the load case being evaluated.

## G.2.7 Results

Results obtained from the 2h model and 1w+2h models are summarized in the following two subsections. These results include wall displacements and stresses as a function of elevation, as well as cross-sections showing stresses for the facewall and tailwall. Figures G-1.1 through G-1.28 in Attachment G-1 to this Appendix include wall displacements and OCSP<sup>®</sup> wall stresses for the 2h models; Figures G-2.1 through G-2.23 in Attachment 2 to this appendix include wall displacements and OCSP<sup>®</sup> wall stresses for the 1w+2h models. A subset of these figures, as well as a few additional figures, are discussed in each of the following two subsections. The results from the 1w+2h defect models and design implications are also discussed in Section 6 of this suitability study report.

### G.2.7.1 2h Models

Figure G-17 illustrates lateral displacement and hoop stresses at the center of a facewall at various stages of the analysis for the reference model base case. Several things are evident from the displacements.

- Relatively modest movements occur during backfilling of the wall until the water level in the backfill rises to elevation 20 feet, which is 20 feet greater than the waterside. In the model, this differential water pressure acts from elevation -51 to +20 on the face sheets.
- Larger movements subsequently take place when the mudline is lowered, especially below elevation -42. In fact, the base of the wall begins to move when the mudline is dredged below -42 feet, which suggests the structure is subject to movements consistent with a global instability. This was investigated by creating another version of the model and using long-term undrained strength parameters for the BCF during dredging. Examining Figure G-18, which shows wall displacements from the base case model and the model using long term  $S_u$  BCF strength, confirms that increasing the strength of the BCF material reduces the movement at the tip of the OCSP<sup>®</sup> face sheets.
- Increasing the tailwall length decreases the movement of the facewall relative to its base but does not affect the basal movement, as can be seen by examining Figure G-19.

Given that the 1w+2h models are based on the 2h base case model, it is important to establish the relevance of model results for dredging below -42. It is obvious that increasing the strength of the foundation material for the OCSP® structure, that is, the BCF, will produce smaller total wall movements at the deeper dredge levels by reducing or eliminating the plastic strains in the foundation material. If the shape of the deflected facewall remained the same, the stresses in it would be unchanged. It can be seen by examining Figure G-19 that above the mudline the shape of the wall between the two cases is essentially the same but there is a small inflection introduced in the case of the higher BCF (long-term) strengths. Figure G-20 shows the facewall stresses from the two cases and reveals that although there is a slight increase in the facewall tensile stresses near the mudline above the base case values, the differences are only on the order of 1 to 2 psi. On the other hand, there is a substantial increase in the compressive stresses below the mudline. However, as discussed below, the accuracy of the compressive stresses from the model below the mudline is questionable as this aspect of behavior is strongly influenced by the assumption of no flexibility at the interlock locations.

Although the modeling approach for the local defect modeling is to focus on the relative impact of defects on the system and not the values of displacements and stresses, it is still worthwhile to look at the model behavior versus the actual system. The displacements from the base case are similar in pattern to, but larger in magnitude than, the inclinometer data from the 1-year monitoring report published by Terracon in February 2011 (Terracon, 2011b). Examining the results in Appendix G from models shows that increasing the backfill and backfill-to-sheet-pile interface friction angles and the backfill stiffness parameters can significantly decrease the facewall movements without significantly altering the hoop stresses in the facewall or tailwall.

Several other results are also apparent from the facewall hoop stresses shown in Figures G-17 and G-20:

- The stresses in the wall increase to about 10 ksi during the backfilling process, which includes the development of the differential water head of 20 feet between the land and water sides. Also, the stresses above the construction mudline do not change much when the mudline is lowered.
- Below the original mudline there are significant hoop stress increases, and the hoop stresses below the initial mudline but above the final mudline ultimately increase to a maximum that is slightly larger than those above the initial mudline. It is also apparent that there are some compression stresses in the facewall below the mudline. The magnitude of these compression stresses is likely over-predicted by a significant amount for two reasons. First, in the real system unlike the model there is compliance at the interlock locations. Second, in the real OCSP® system the tailwall and facewall have lower stiffness in compression than the model because rotation can occur at the interlocks.
- The real walls would exhibit lower initial stiffness when subjected to hoop compression and then be prone to local buckling by rotation at the interlocks. Similarly, the over-prediction of compression stresses below the mudline also indicates that the model slightly under-predicts the maximum tensile hoop stress as well as the deflection of the wall above the mudline. This effect can be seen by examining Figure G-21, which illustrates facewall displacements and hoop stresses from the model with the lateral stiffness reduced by 1/10th. The tensile stresses above the mudline are essentially the same as for the base case, but with the reduced lateral (hoop) stiffness, the compressive stresses below the mudline are significantly diminished.

Figure G-22 illustrates contours of the horizontal membrane stress resultant in the tailwall and facewall structural elements for the reference model base case. The horizontal membrane stress resultant is equal to the integral of the horizontal stress in a structural element over the thickness of the element, and therefore has the units of force/length. Stress resultants for structural elements are reported in terms of the element material coordinate system, which in this case is defined so that the material x-axis lies in a horizontal plane, the z-axis is normal to the element face, and the y-axis is up (+z in global coordinate system). The previously discussed compressive stresses below the mudline in the tailwall and facewall can clearly be seen.

Figure G-23 illustrates the tailwall anchor loads, that is, the mobilized horizontal pullout resistance, computed by integrating the horizontal membrane stress resultant along vertical profiles from the front of the tailwall to its

end. The tailwall anchor load is plotted along the length of the tailwall and diminishes from a peak near the wye to zero at the end of the wall. The increase in tailwall anchor load as the mudline is dredged to elevation -51 from -42 is much less than the increase during dredging from elevation -30 to -42. This is consistent with the observation that the model becomes marginally stable during the dredging from -42 to -51. The instability is evident in the significant movement of the tip of the face when dredging past elevation -42 seen in Figure G-17 and the mesh displacement vectors shown in Figure G-24. Figure G-25 shows facewall displacements from the base case and a model with the tailwall lengthened by about 6 feet. Comparing the plots shows that lengthening the tailwall appreciably decreases the wall movements above the mudline, but does not affect the movement at the base of the wall, and hence it is concluded the tailwall lengthening does not improve the global stability of the OCSP® structure in this case. Figure G-26 shows that facewall hoop stresses from the base case and the model with the tailwall extended 6 feet are very similar and hence lengthening the tailwall has no significant effect on the facewall hoop stresses.

Figure G-27 illustrates contours of the stress level and shear stress vectors in the tailwall geogrid coupling elements from two stages in the base case model. The shear stress vectors show the direction of the stress that the coupling springs are applying on the adjacent soil. One stage is during the backfill modeling just prior to raising the water level on the landside from elevation 0 to +20, and the second is the last dredge step in the model, that is, mudline at -51. Comparing the two stages shows several things:

- During filling, the shear stress acting on the wall is primarily vertical, which is consistent with settlement of the backfill and foundation soil during filling.
- During the last dredging step, the interface shear strength is mobilized over nearly the whole wall.
- During the last dredging step, the shear stress acting on the wall has become more horizontal, especially below the active earth pressure zone and below the original sea floor, which is consistent with pulling out of the wall.

Because the base case model exhibits a global instability due to plastic shear strains in the BCF, it is useful to examine results from the model stage with the mudline at -42, for which the model OCSP® structure is still globally stable. Figure G-28 shows these results, and comparing with Figure G-27 it can be seen that the level of mobilized shear strength between the tailwall and adjacent soil actually decreases in a triangular zone extending up from the tip of the facewall when the structure experiences a base instability during the final model dredging steps with the lower, short-term, undrained shear strength for the BCF. The complexity of the pattern of shear stress direction on the shear wall is interesting to note in comparison with the simplified assumptions that must be used during a geotechnical design based on limit-equilibrium methods. Figure G-29 illustrates the magnitude of relative shear displacement between the tailwall and adjacent soil at the end of dredging and when dredging is at elevation -42 in the base case model. This result corroborates the observation from Figure G-27 that a triangular block of soil is tending to move with the wall as it experiences basal movements. Examining the relative shear displacement magnitudes and the shear stresses from the previous figures also shows that a large amount of slip occurs in the backfill zone during the backfill process.

Finally, examining the wall displacements and hoop stresses from the pseudo-static representation of an earthquake load on the base case model with the final mudline at elevation -42 shown in Figure G-30 shows that relatively small increases in the wall displacement and hoop stress occurred for the applied body force of 0.05g on a wedge of soil corresponding to an active earth pressure zone behind the OCSP® face.

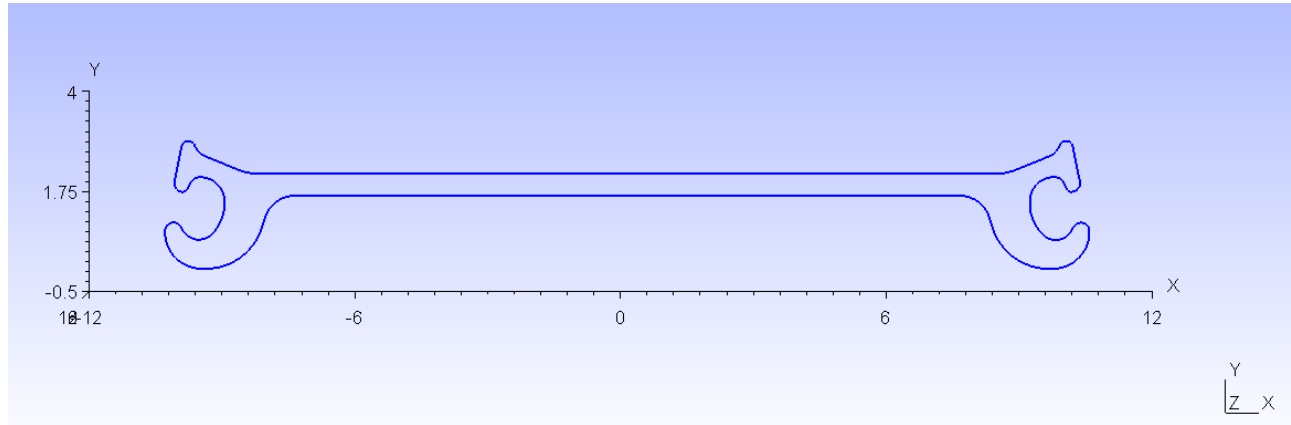
### G.2.7.2 1w+2h Models

The local defect models are based on the model sequence, material models, and boundary conditions used for the 2h reference model base case. As mentioned in the discussion of 2h model results, the base case exhibits instability as the mudline depth approaches elevation -51. Consequently, the model displacements when the dredging depth increases represent lower bound estimates because plastic flow in the model was truncated by limiting the number of solution steps. However, the model results for loads and stresses on the OCSP® walls are less affected by the force imbalance from plastic flow and reasonably accurate.

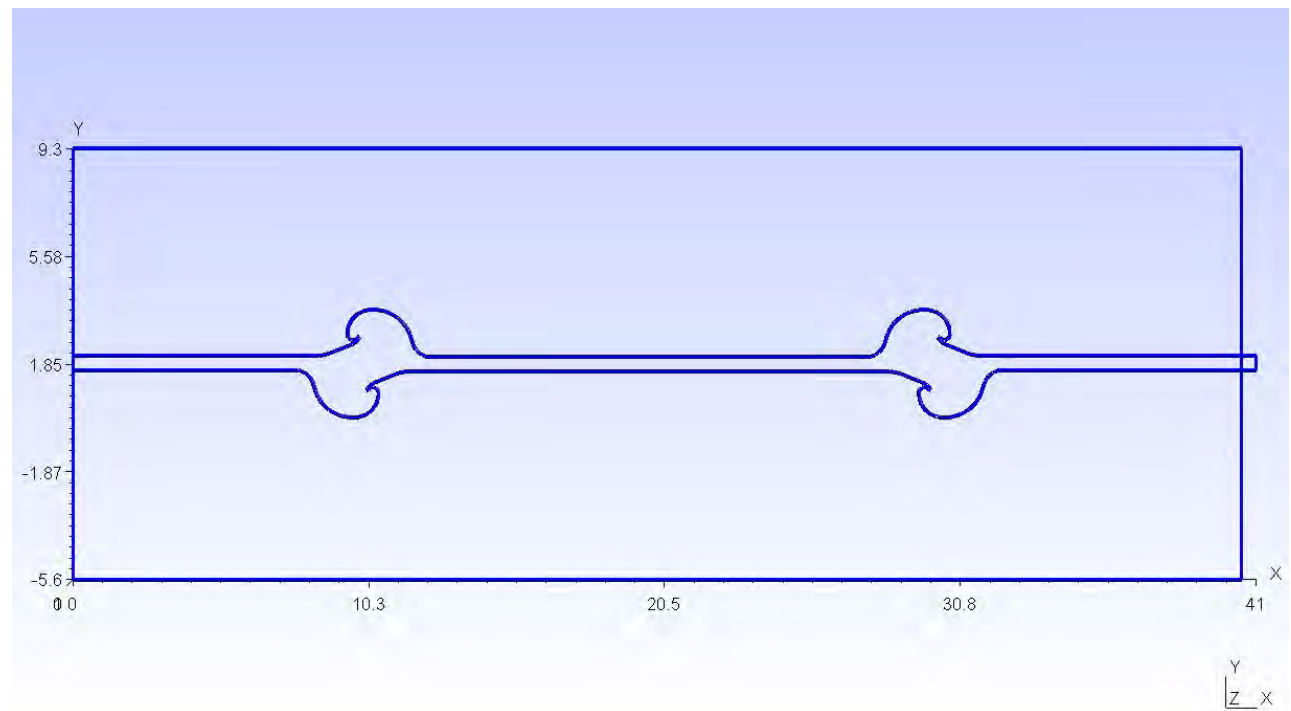
Figures G-31 and G-32 are contour plots of the horizontal stress resultant in the tailwall and facewall for the tailwall tear and notch defect models. The horizontal stress resultant is equal to the hoop stress integrated over the thickness of the shell element. The defect extends up to elevation -30 in both models, and it can be seen that the pattern of stresses and stress concentration at the top of the defect are very similar in both models. This result demonstrates that the previously described tear and notch methods of modeling defects produce similar results for tailwall defects.

Figure G-33 is a contour plot of the horizontal stress resultant in the tailwall and facewall for the facewall tear to elevation -30 defect model. This result, which may seem counter to intuition, illustrates that in contrast to a tailwall defect, a facewall defect does not tend to produce a stress concentration. There are a couple of reasons for this result. First, the defect relieves stress on the facewall by allowing the soil to spill out below the top of the defect. Therefore, in contrast to a tailwall defect, which tends to result in a redistribution of stresses to transmit loads similar to a no-defect case, a facewall defect tends to reduce loads on a system. Second, the defect models were run in small strain mode and effects from changing geometry are not included in the model.

The results for tailwall and facewall defects (see Figures G-2.3 and G-2.9) that do not extend above the final mudline show that such defects have relatively minor impacts on the wall system. Also, the displacements and stresses for the pseudo-static representation of an earthquake load on the model with a tailwall tear defect extending up to  $z=-42$  feet shows, as one would expect from intuition and the 2h model result, an increase in the displacements and stresses. In particular, the magnitude of the stresses at the stress concentration at the top of the defect increases and thus demonstrates the potential for such a defect to propagate upward during an earthquake.



**FIGURE G-1. PS31 Sheet Pile Section**



**FIGURE G-2. Section View through Conceptual Pullout Test Device with Two Interlock Joints**

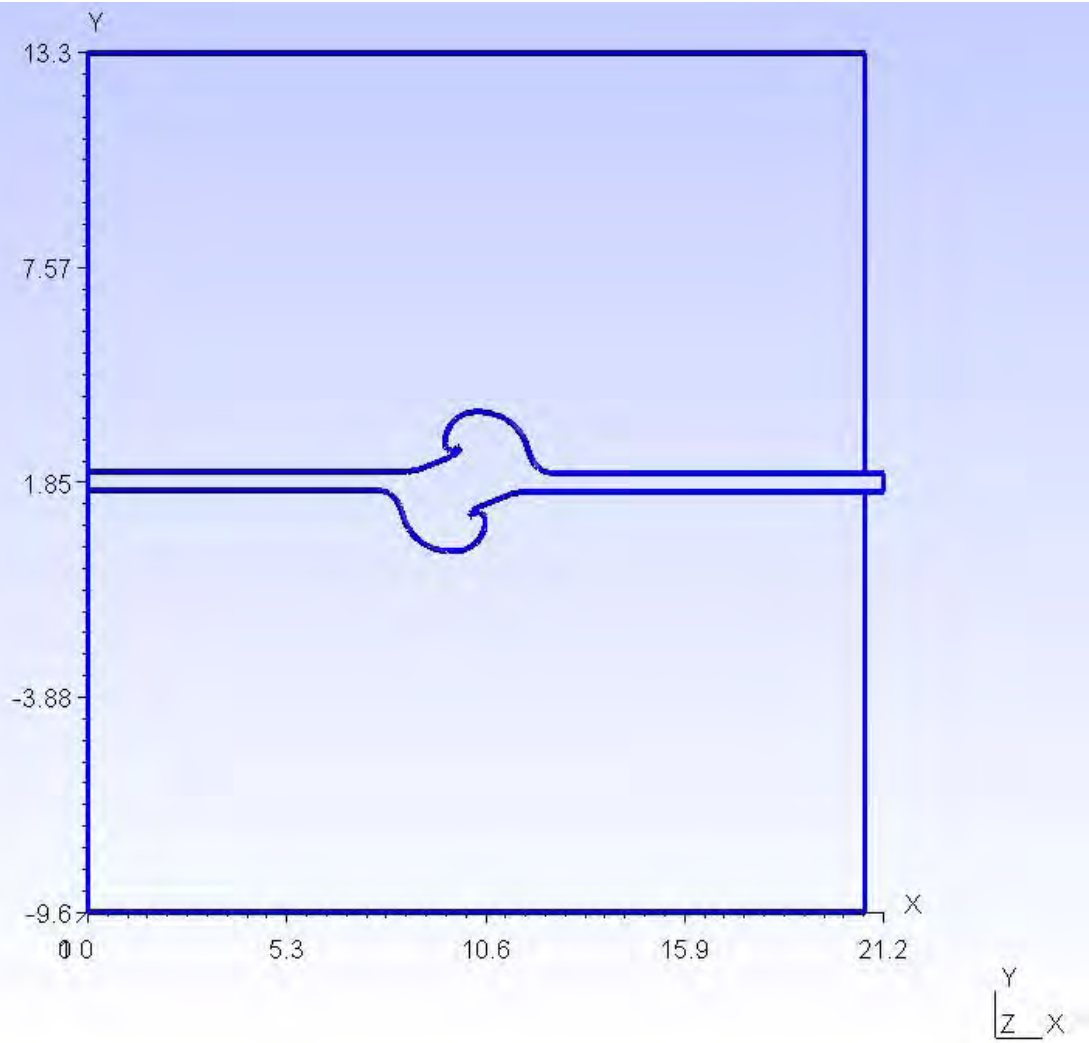


**FIGURE G-3. Section View through Pullout Test Model with One Interlock Joint**

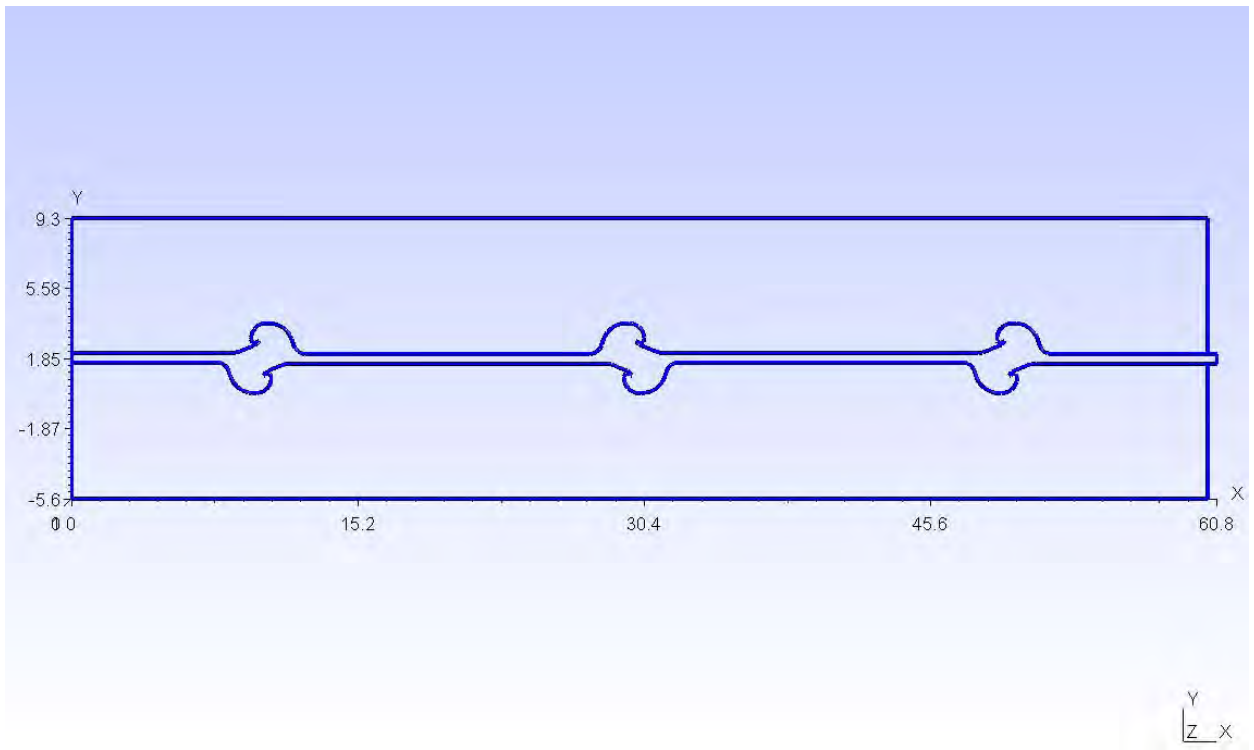


**FIGURE G-4. Section View through Pullout Test Model with Three Interlock Joints**

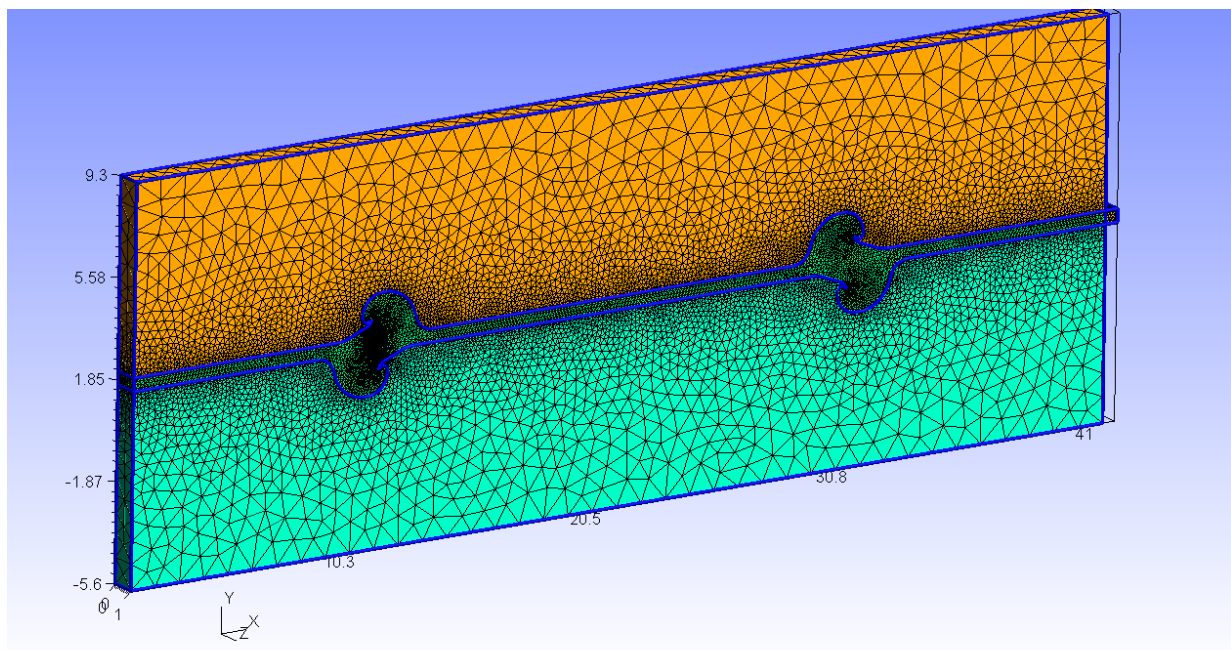


**FIGURE G-5. Finite Element Mesh for Two Interlock Shallow Soil Box Model**

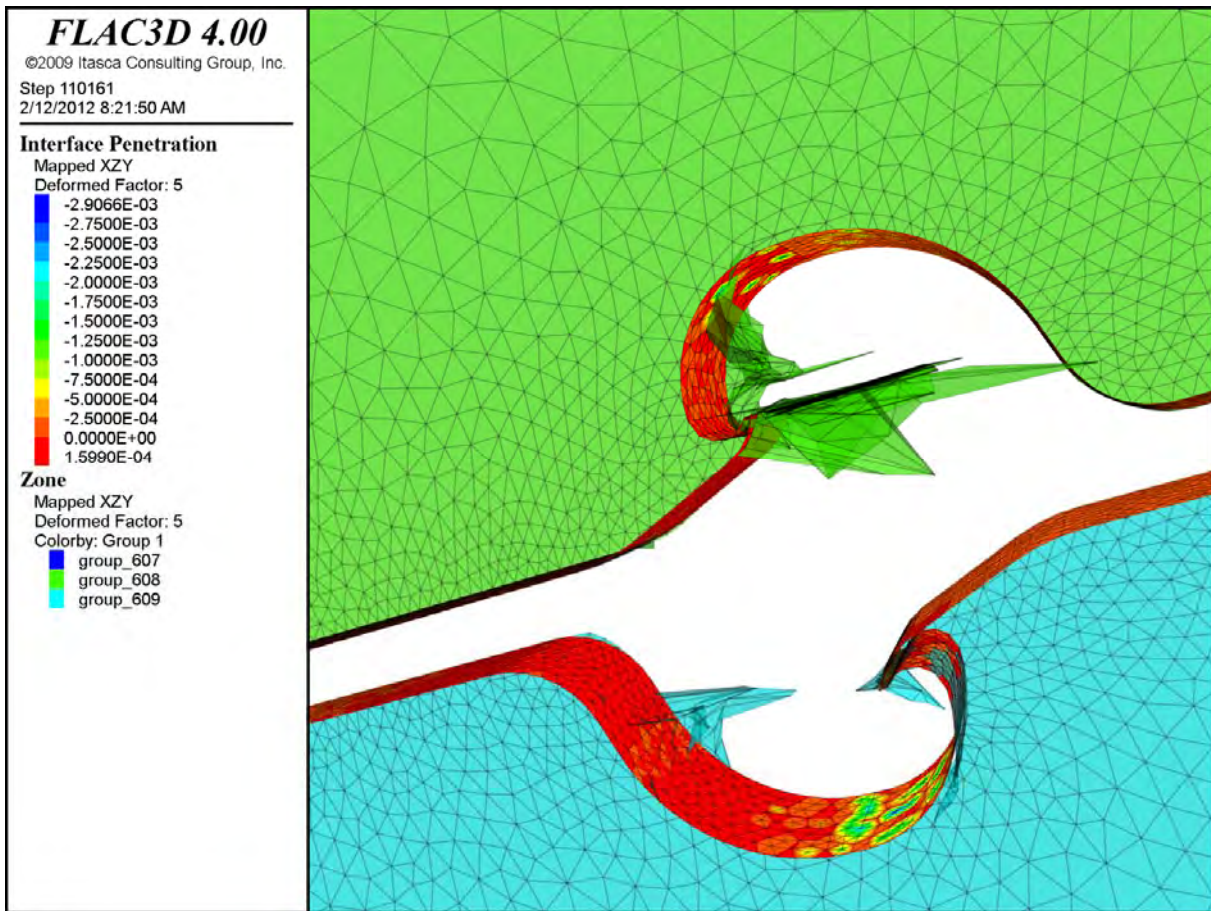


**FIGURE G-6. Penetration of Soil Elements into Steel Interlock with Interface Attached to Steel (Steel Elements Omitted for Clarity)**

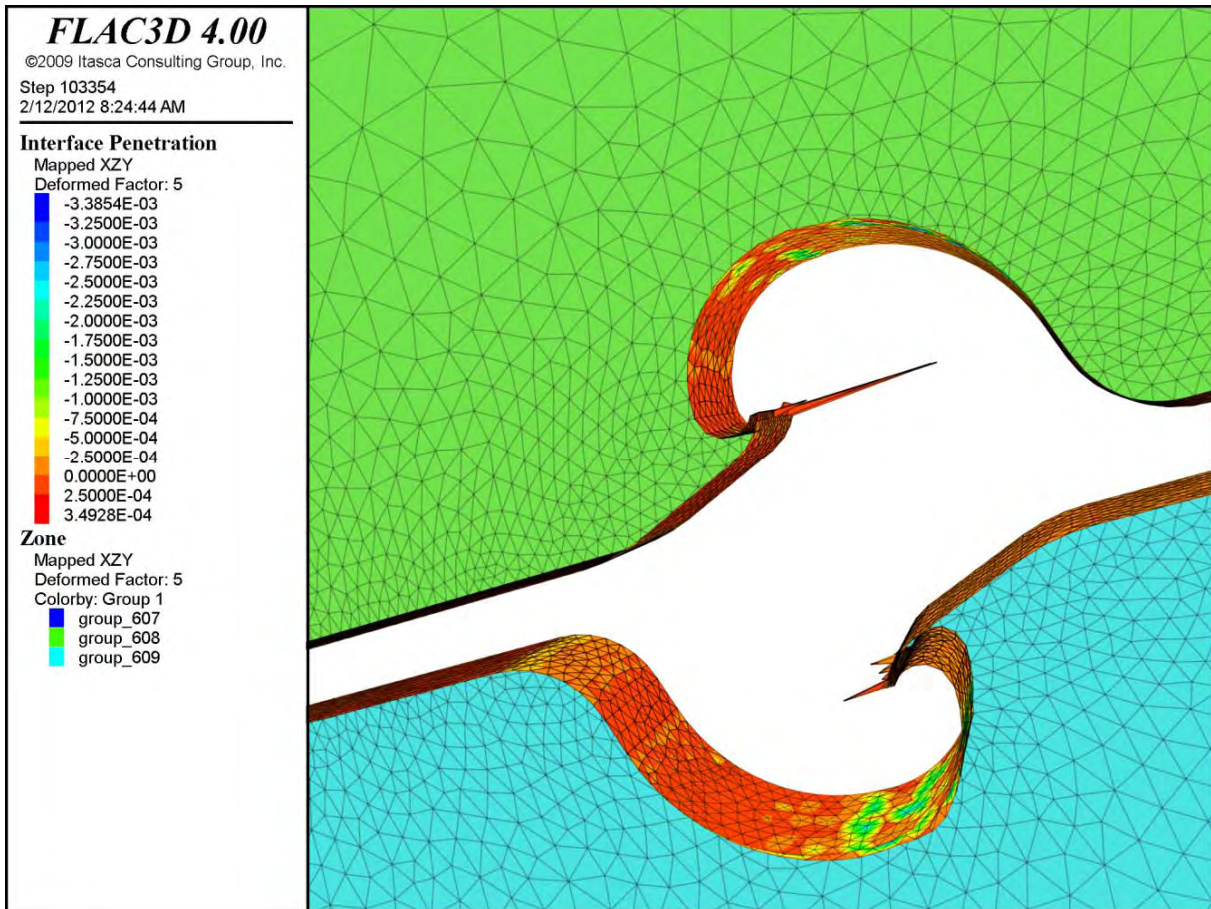


**FIGURE G-7. Penetration of Soil Elements into Steel Interlock with Interfaces Attached to Soil and Steel (Steel Elements Omitted for Clarity)**

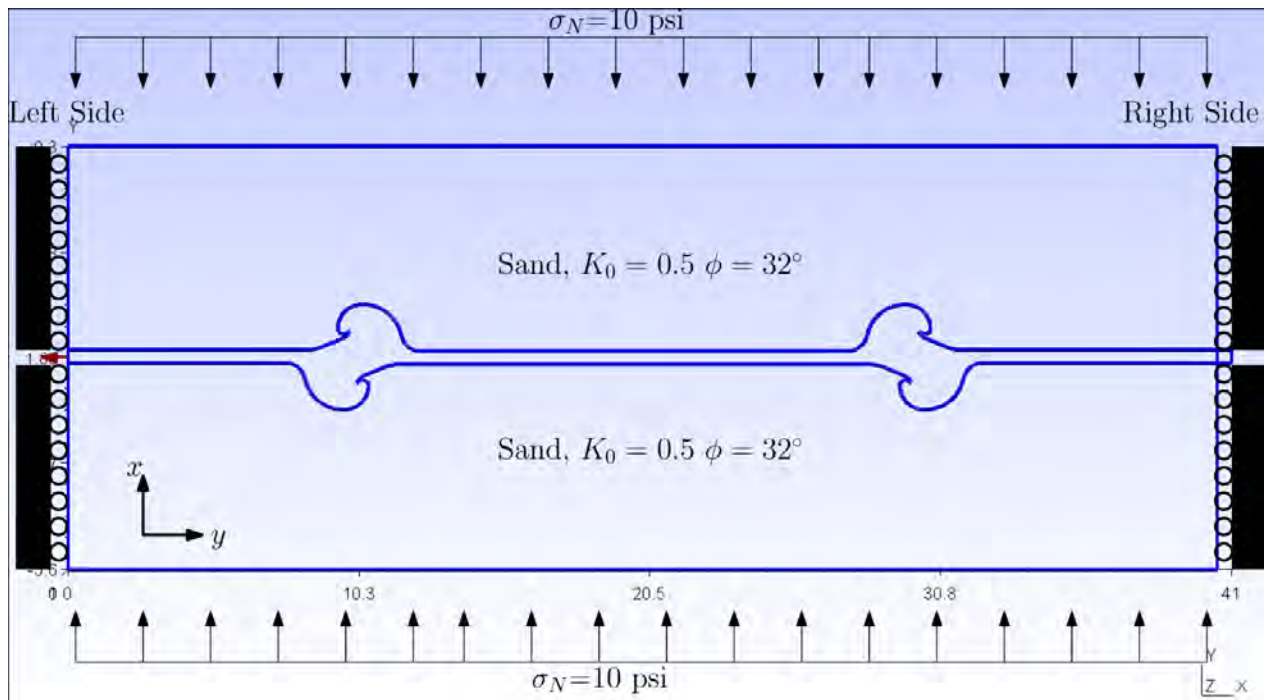


FIGURE G-8. Boundary Conditions for Pullout Test Model

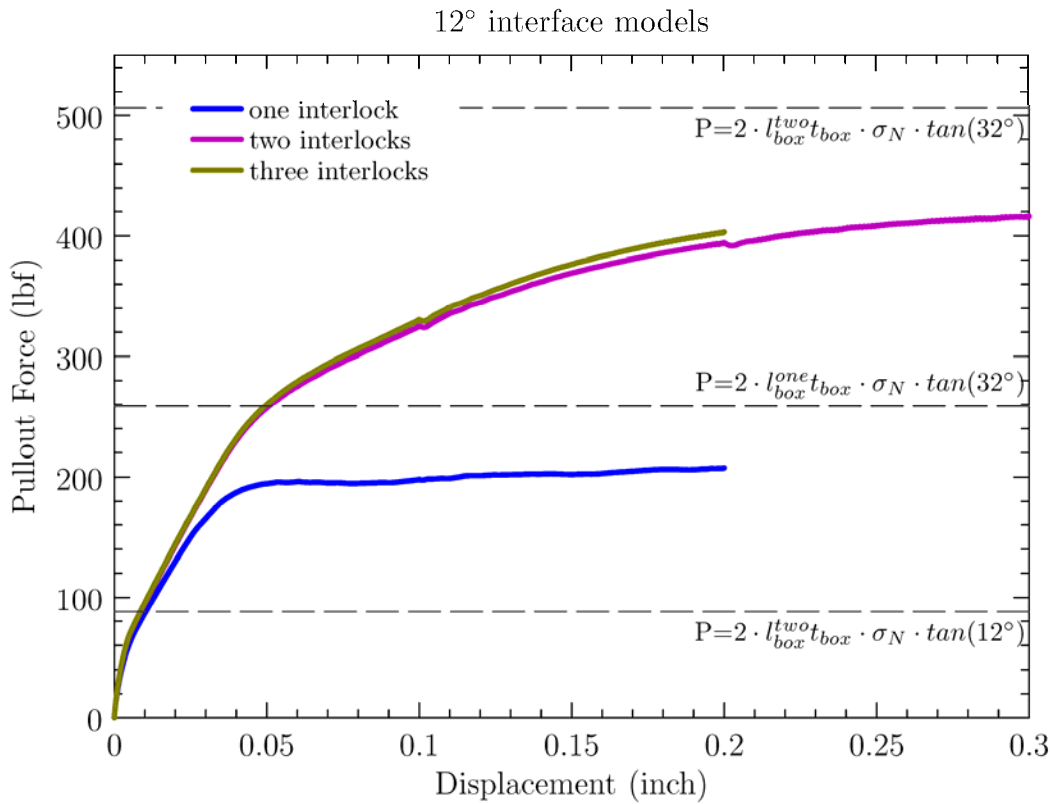


FIGURE G-9. FLAC<sup>3D</sup> Pullout Test Results for One, Two, and Three Interlock Models

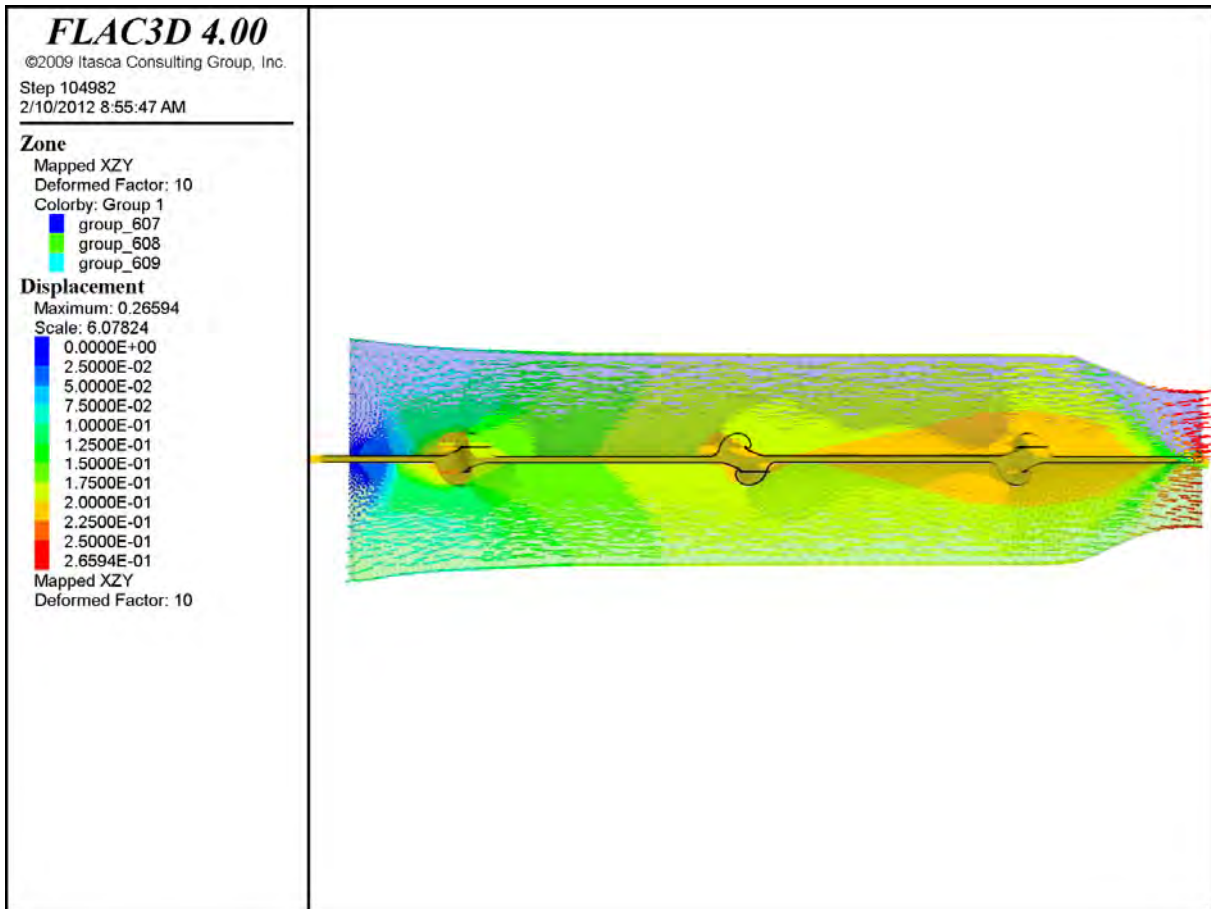


FIGURE G-10. Displacement Vectors at 0.2016 Inches Displacement

Single Interlock Models

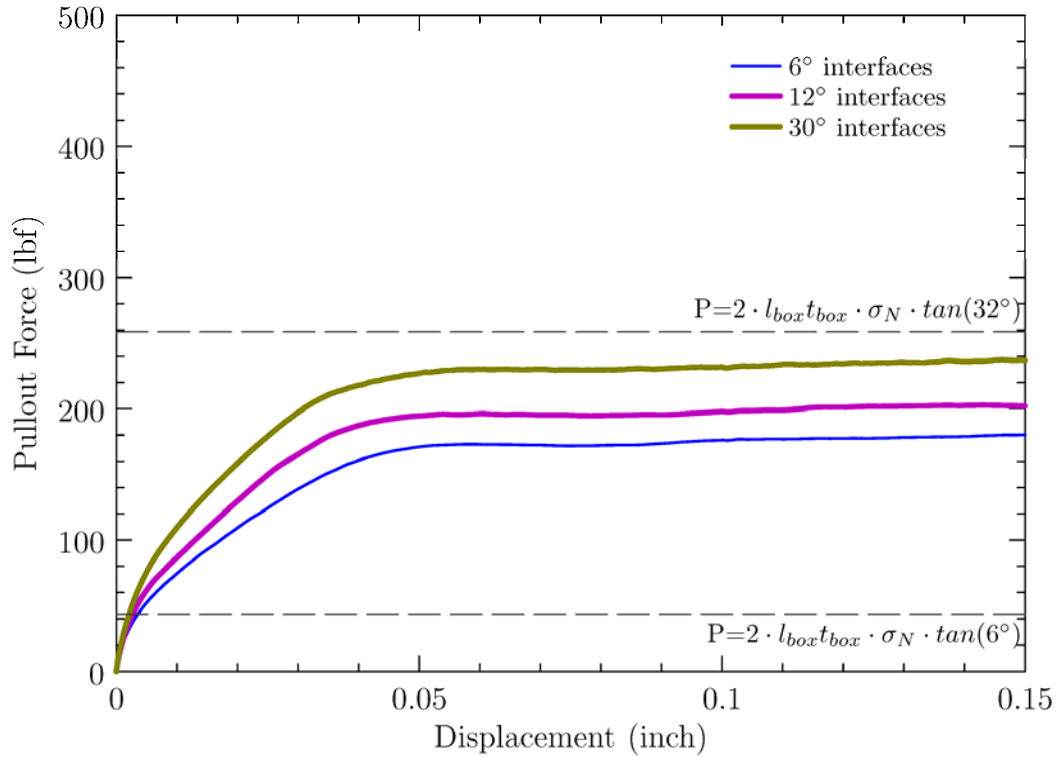


FIGURE G-11. FLAC<sup>3D</sup> Pullout Test Results for Single Interlock Model at Various Interface Friction Values

Two interlock 12° interface models

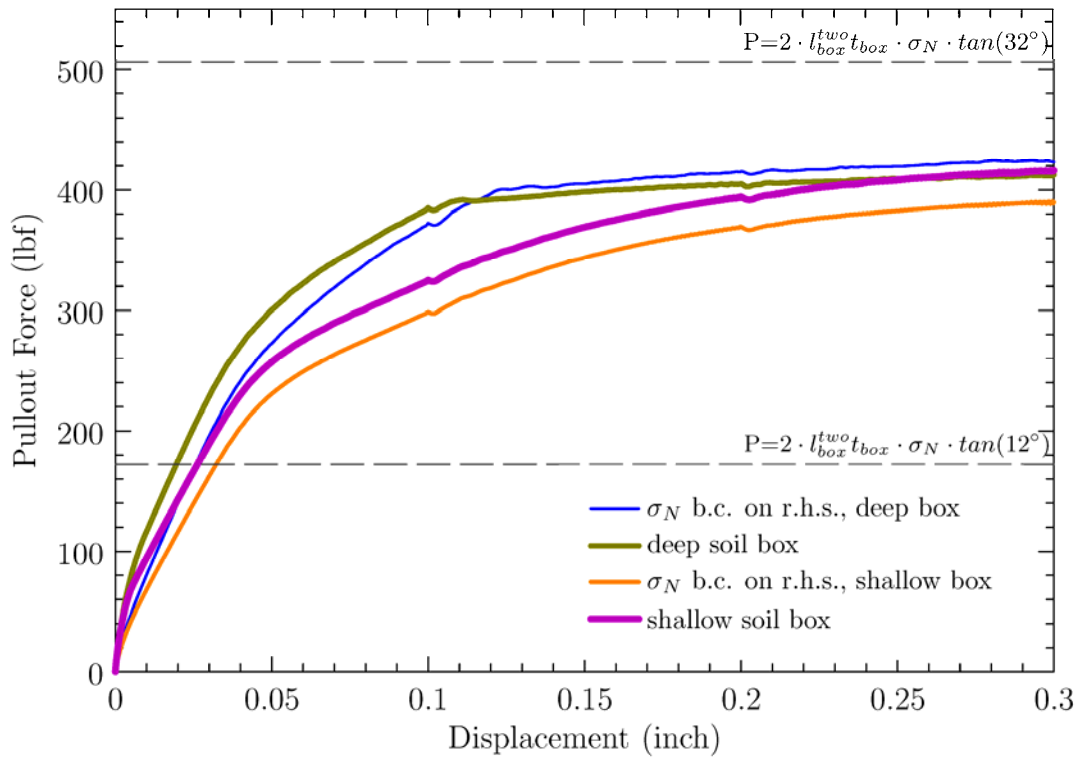
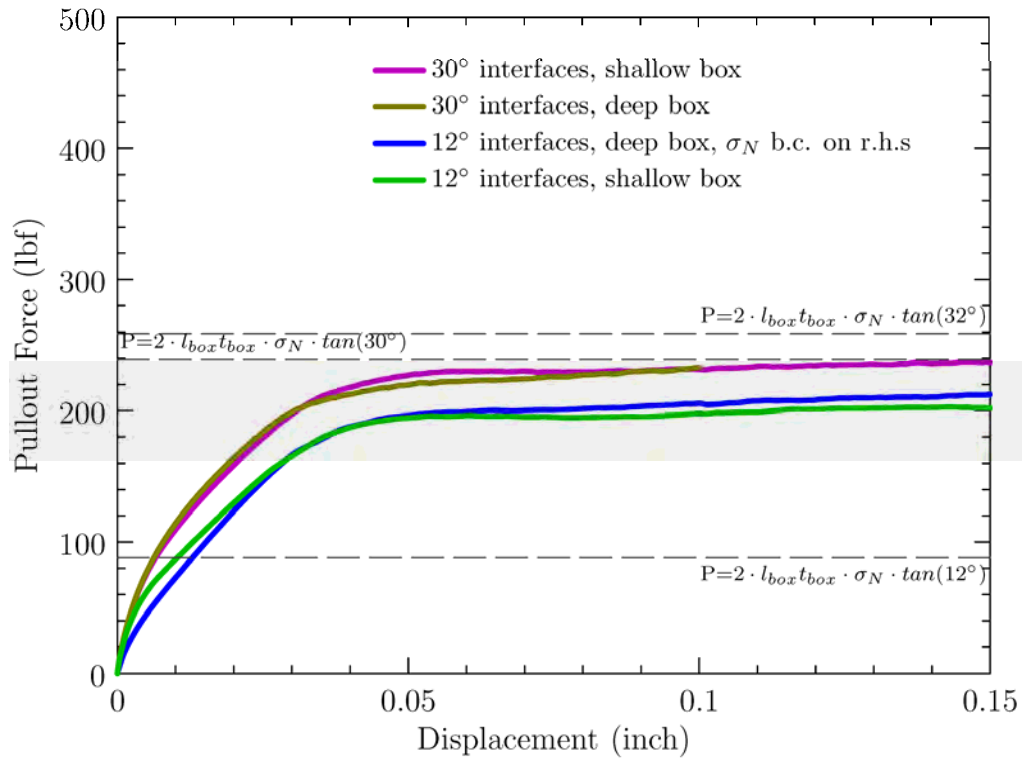
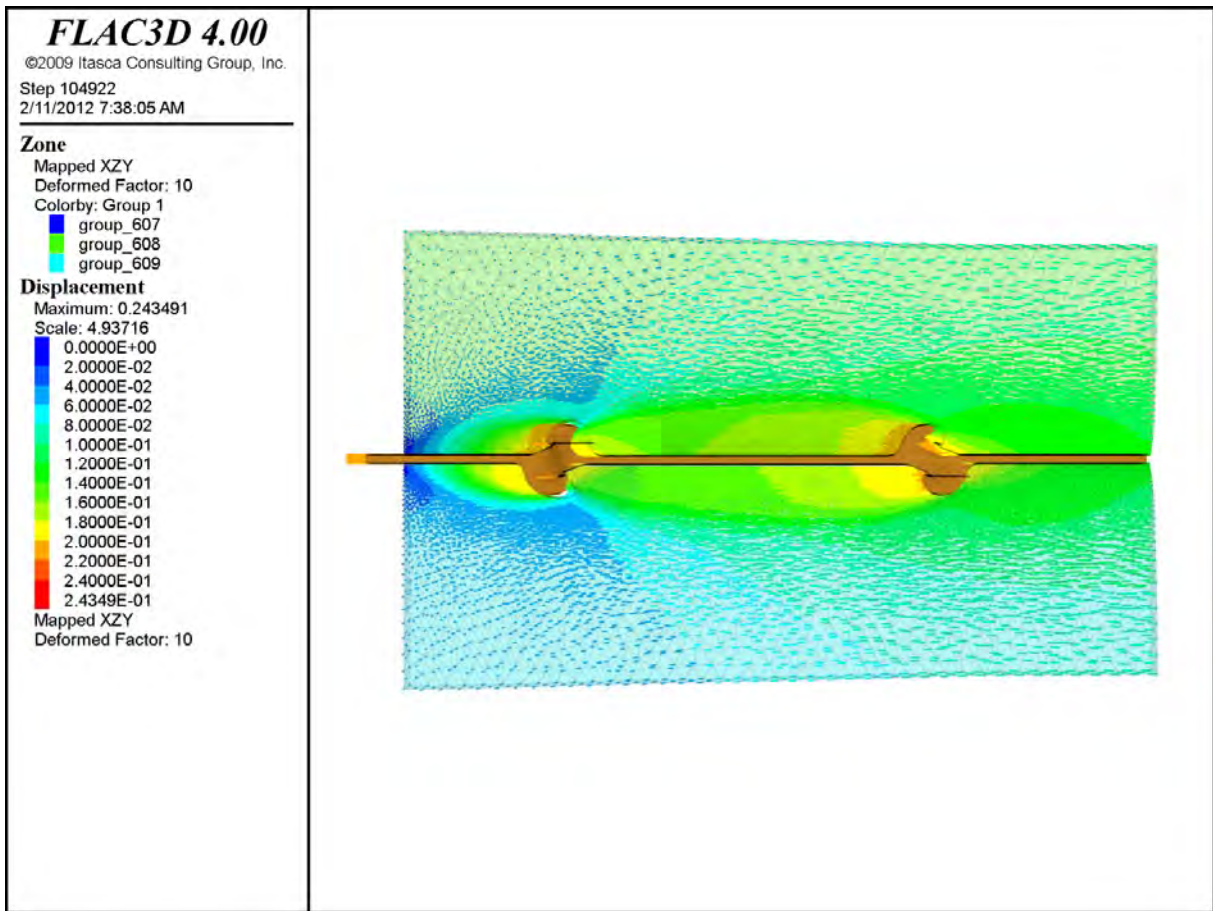


FIGURE G-12. FLAC<sup>3D</sup> Pullout Test Results for Two Interlock Models

## Single Interlock Models

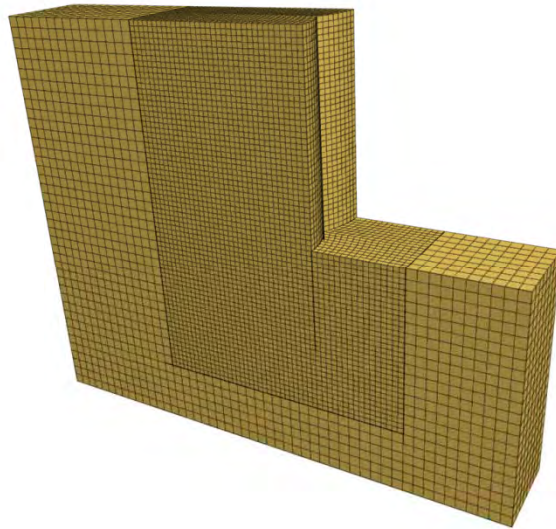
FIGURE G-13. FLAC<sup>3D</sup> Pullout Test Results for One Interlock Model



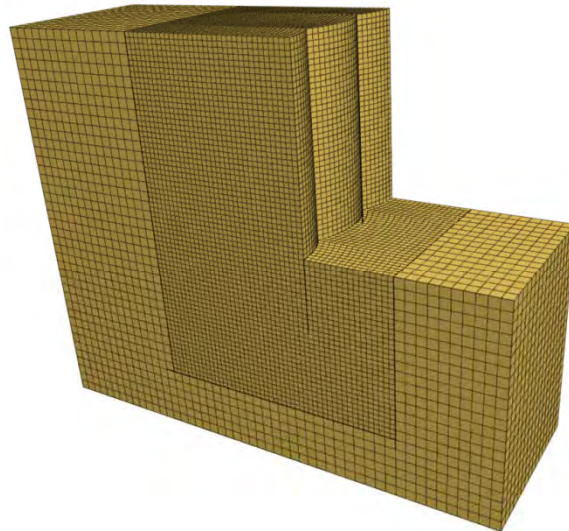
**FIGURE G-14. Contoured Displacement Vectors for the Two Interlock Model with a Stress Boundary on Right Side of Deep Soil Box**

**FLAC3D 4.00**

©2009 Itasca Consulting Group, Inc.

**FIGURE G-15. FLAC<sup>3D</sup> Mesh for 2h (Two Half-Cell) Local Defect Model****FLAC3D 4.00**

©2009 Itasca Consulting Group, Inc.

**FIGURE G-16. FLAC<sup>3D</sup> Mesh for 1w+2h (One Whole Cell, Two Half-Cell) Local Defect Model**

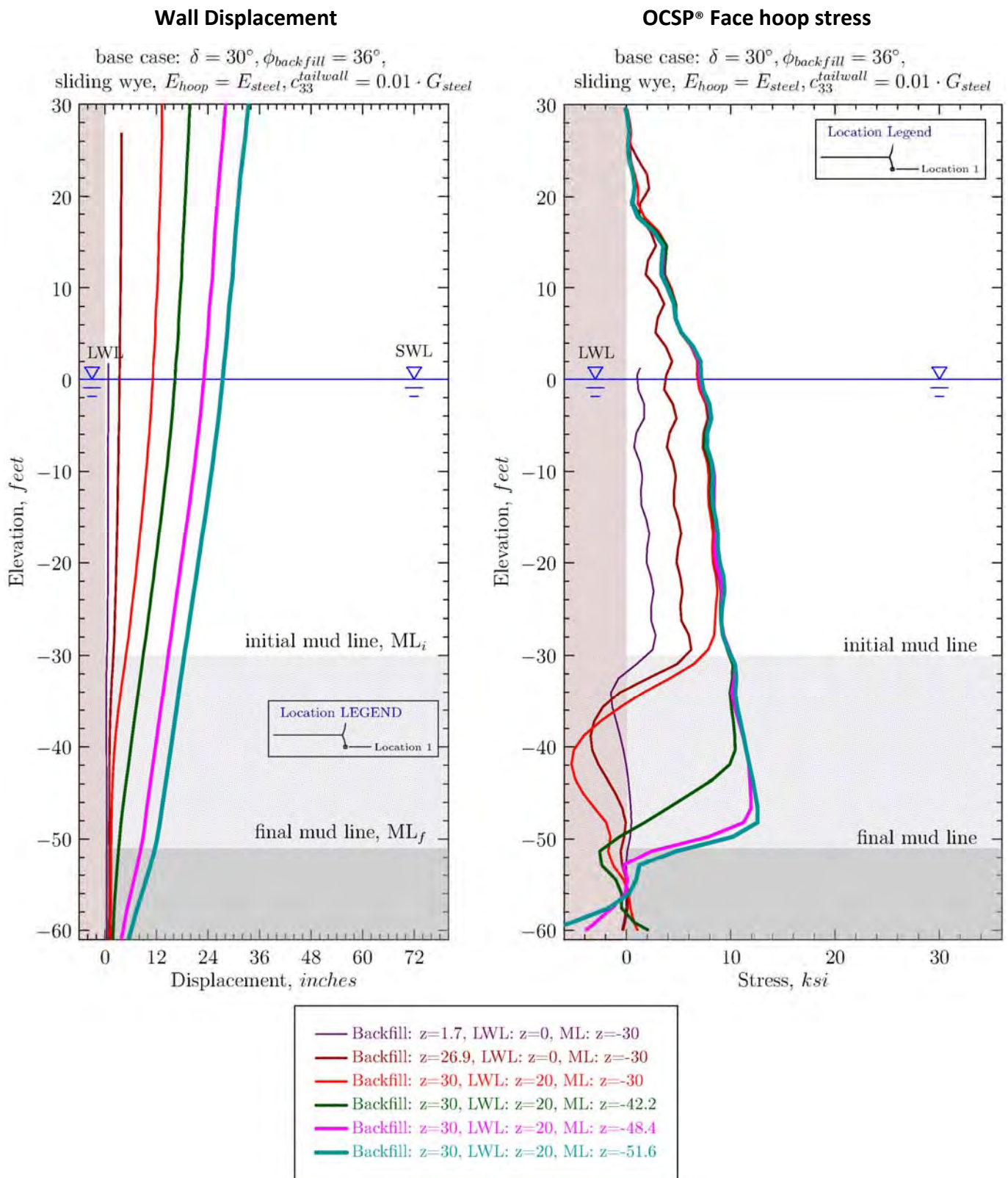
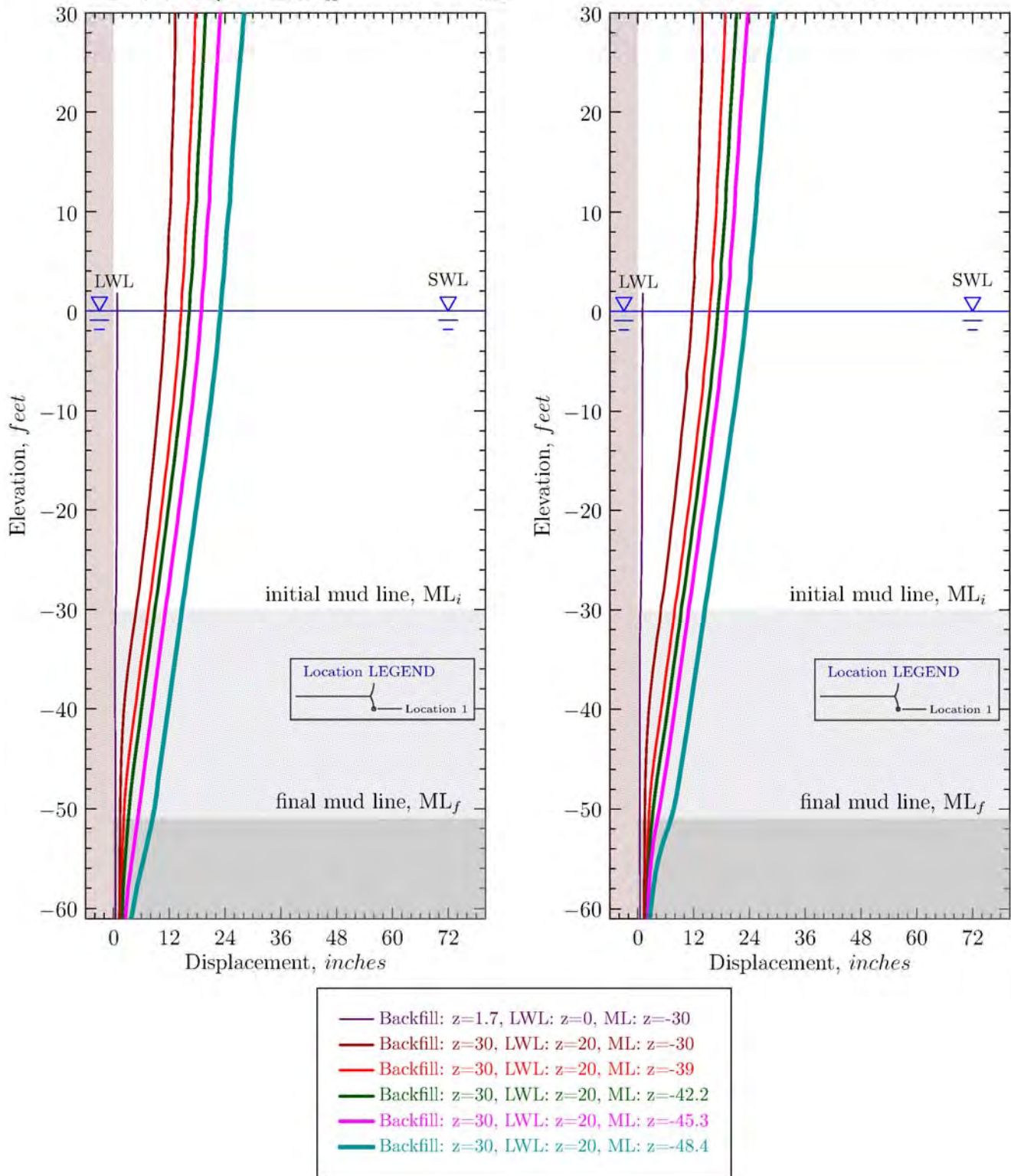


FIGURE G-17. Profiles of Facewall Lateral Displacements and Hoop Stresses from 2h Reference Model, Base Case

## Facewall Lateral Displacement 2h Reference Models

base case:  $\delta = 30^\circ$ ,  $\phi_{backfill} = 36^\circ$ ,  
sliding wye,  $E_{hoop} = E_{steel}$ ,  $c_{33}^{tailwall} = 0.01 \cdot G_{steel}$

Long Term BCF  $S_u$  profile

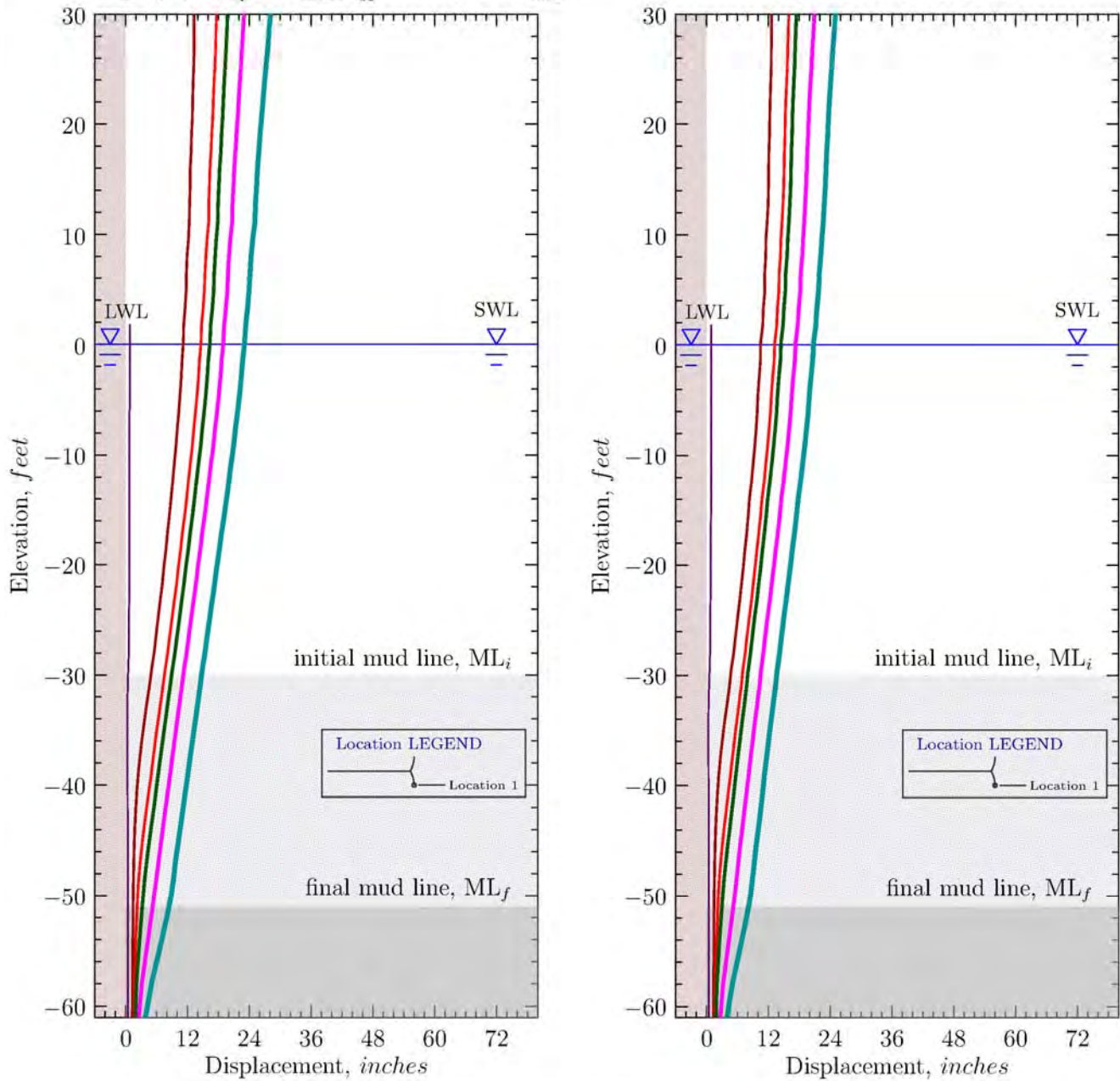


**FIGURE G-18. Profiles of Facewall Lateral Displacements from 2h Base Case and Case with Long-Term BCF Undrained Strength**

## Facewall Lateral Displacement 2h Reference Models

base case:  $\delta = 30^\circ$ ,  $\phi_{backfill} = 36^\circ$ ,  
sliding wye,  $E_{hoop} = E_{steel}$ ,  $c_{33}^{tailwall} = 0.01 \cdot G_{steel}$

tailwall extended 6 feet



- |   |  |
|---|--|
| — | Backfill: $z=1.7$ , LWL: $z=0$ , ML: $z=-30$   |
| — | Backfill: $z=30$ , LWL: $z=20$ , ML: $z=-30$   |
| — | Backfill: $z=30$ , LWL: $z=20$ , ML: $z=-39$   |
| — | Backfill: $z=30$ , LWL: $z=20$ , ML: $z=-42.2$ |
| — | Backfill: $z=30$ , LWL: $z=20$ , ML: $z=-45.3$ |
| — | Backfill: $z=30$ , LWL: $z=20$ , ML: $z=-48.4$ |

**FIGURE G-19. Profiles of Facewall Lateral Displacements from 2h Base Case and Tailwall Extended 6 Feet Case**

## Face Wall Horizontal Membrane Stress 2h Reference Models

base case:  $\delta = 30^\circ$ ,  $\phi_{backfill} = 36^\circ$ ,  
sliding wye,  $E_{hoop} = E_{steel}$ ,  $c_{33}^{tailwall} = 0.01 \cdot G_{steel}$

Long Term BCF  $S_u$  profile

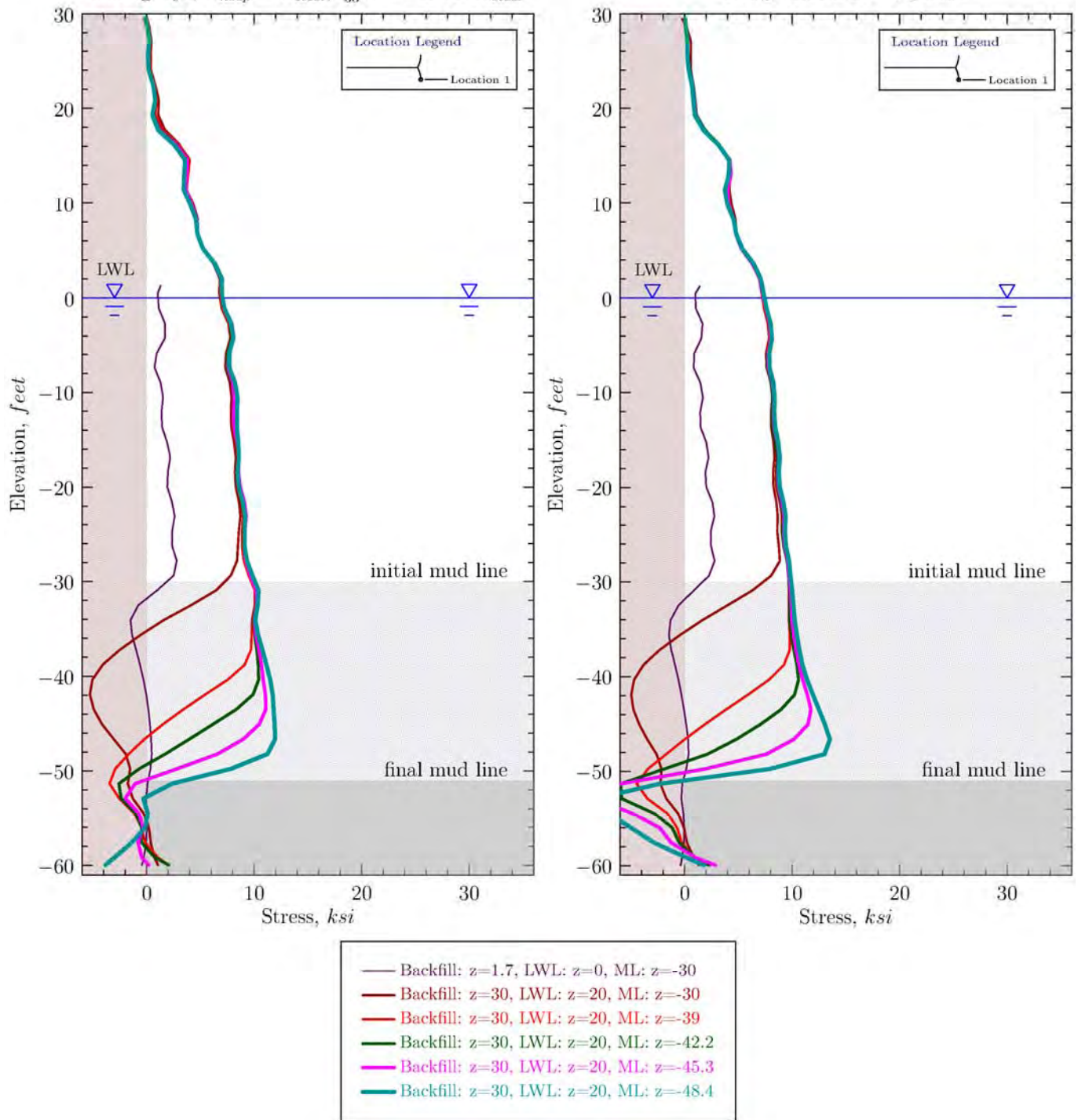


**FIGURE G-20. Profiles of Facewall Hoop Stresses from 2h Base Case and Long-Term BCF Undrained Strength Case**

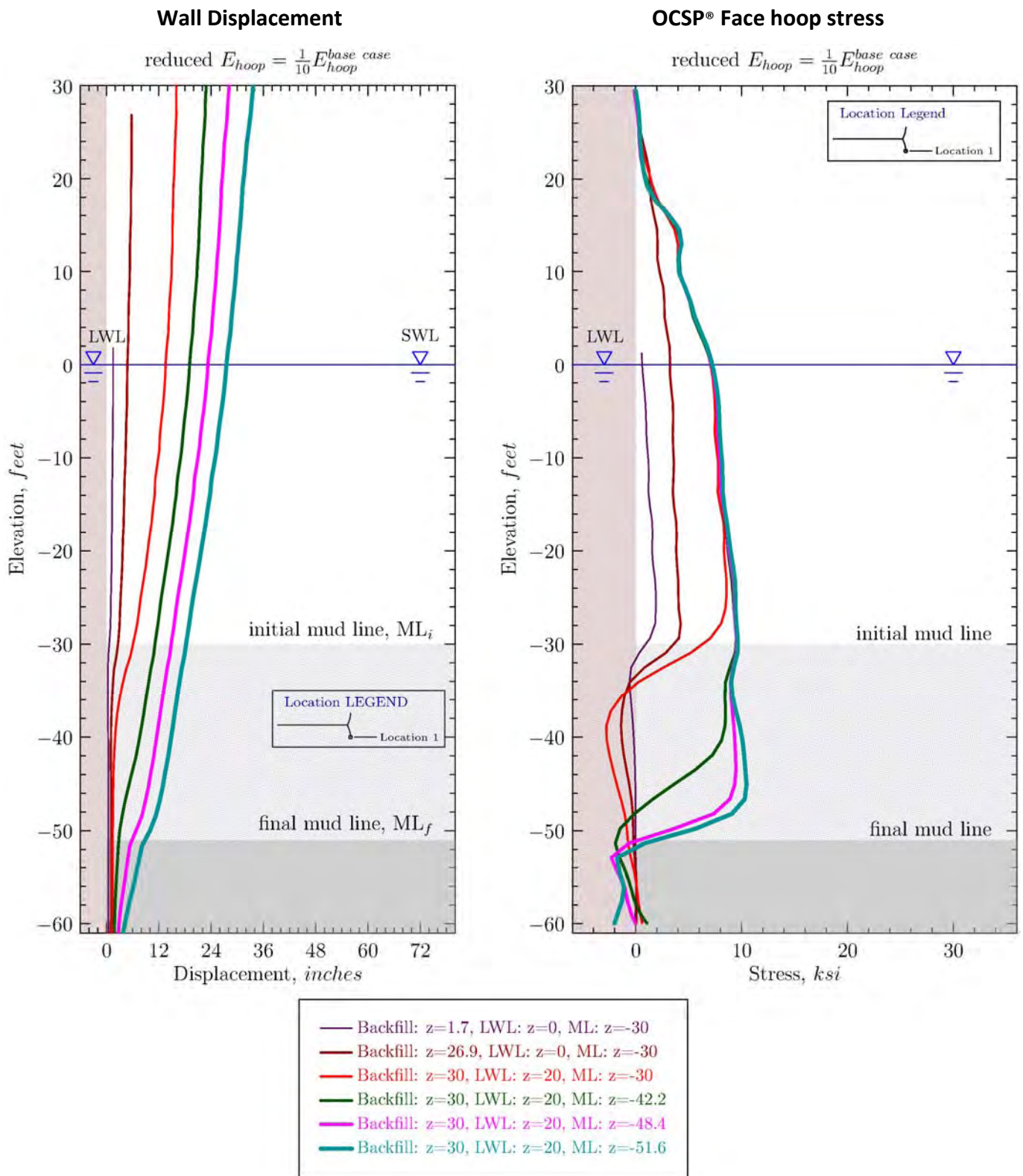


**FIGURE G-21. Profiles of Facewall Lateral Displacements And Hoop Stresses from 2h Reference Model,  $E_{hoop}$  Reduced**

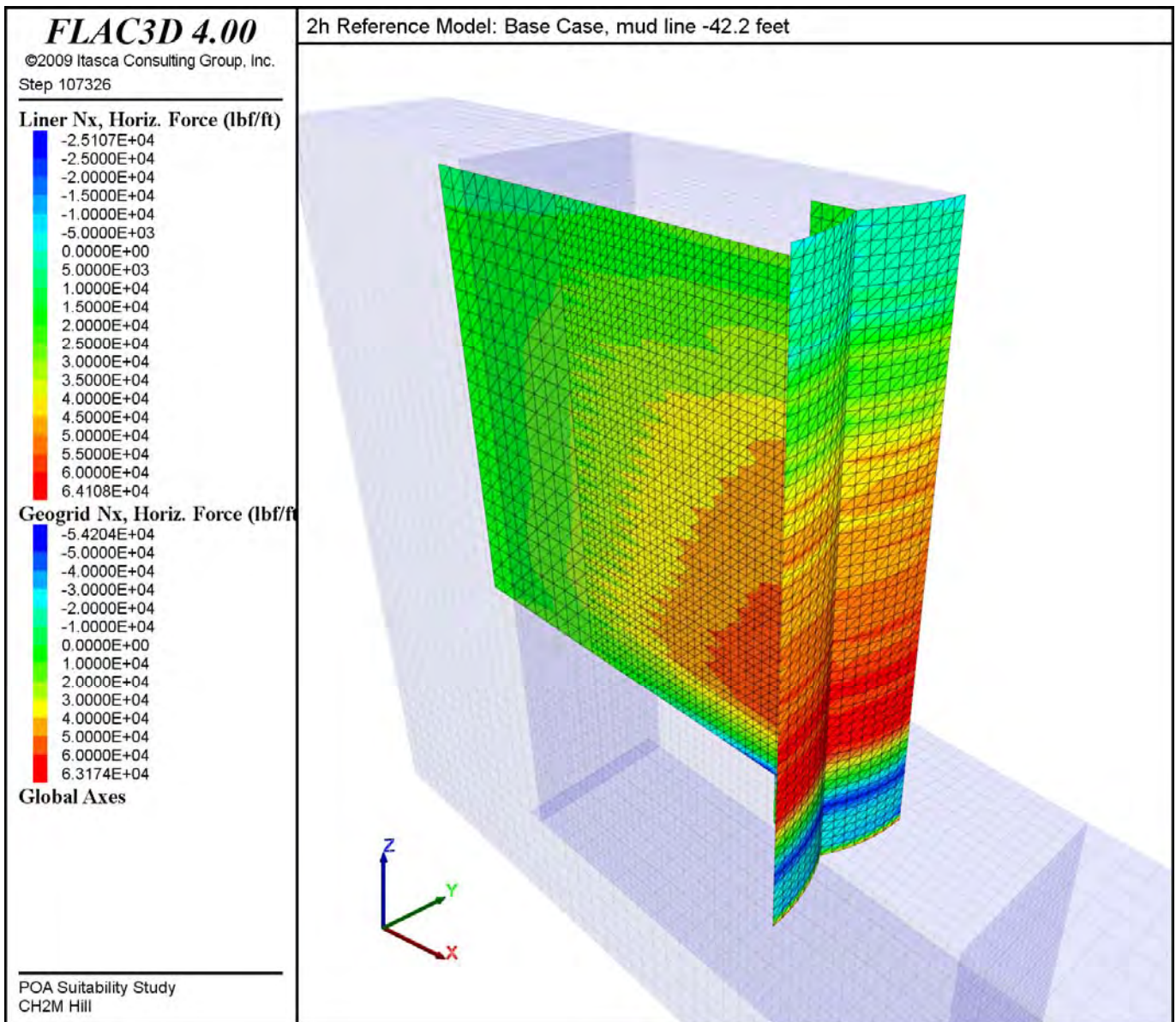


**FIGURE G-22. Horizontal Membrane Stress Resultants in Tailwall and Facewall for 2h Reference Model with Seaside Mudline at -42**

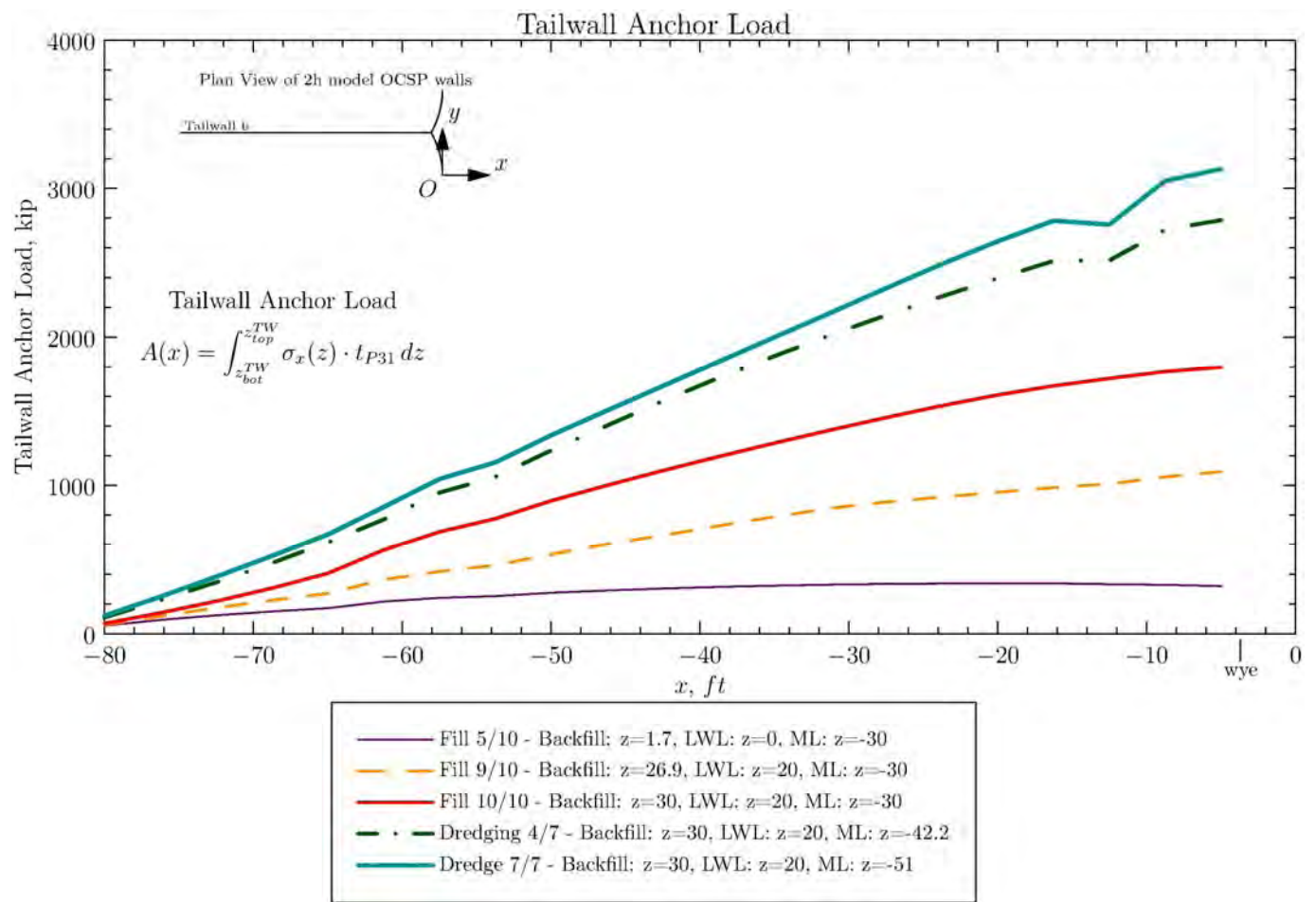
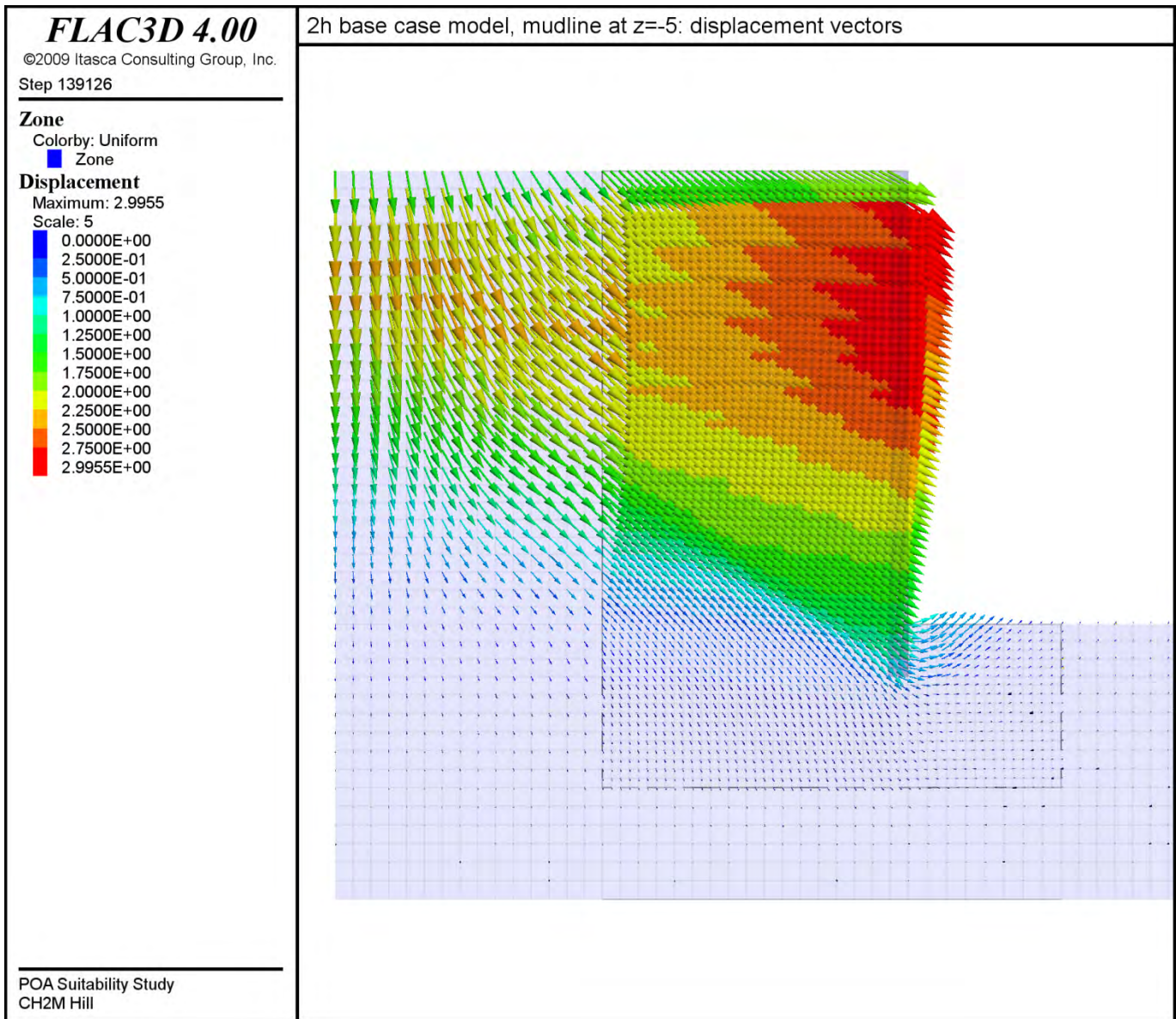


**FIGURE G-23. Tailwall Anchor Loads at Various Model Stages for 2h Reference Model, Base Case**



*NOTE: horizontal bands are an artifact of the incremental construction of the backfill and OCSP® system above the initial seafloor bed of z=-30.*  
**FIGURE G-24. Mesh Displacement Vectors for 2h Base Case Model at Completion of Dredging to z=-51**

## Facewall Lateral Displacement 2h Reference Models

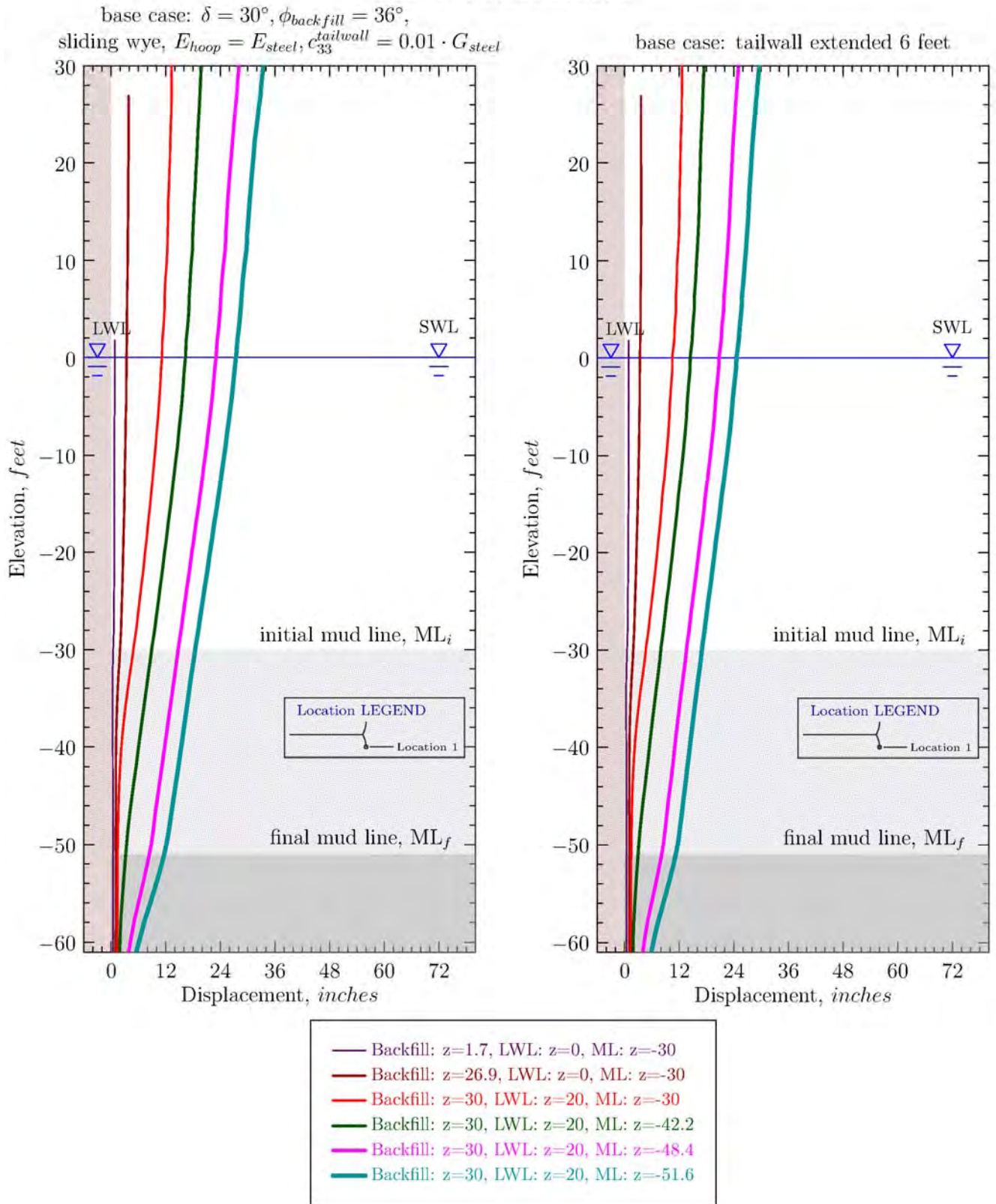


**FIGURE G-25. Facewall Lateral Displacements for 2h Reference Model Base Case and Extended Tailwall Case**

## Face Wall Horizontal Membrane Stress 2h Reference Models

base case:  $\delta = 30^\circ, \phi_{backfill} = 36^\circ,$   
 sliding wye,  $E_{hoop} = E_{steel}, c_{33}^{tailwall} = 0.01 \cdot G_{steel}$

base case: tailwall extended 6 feet

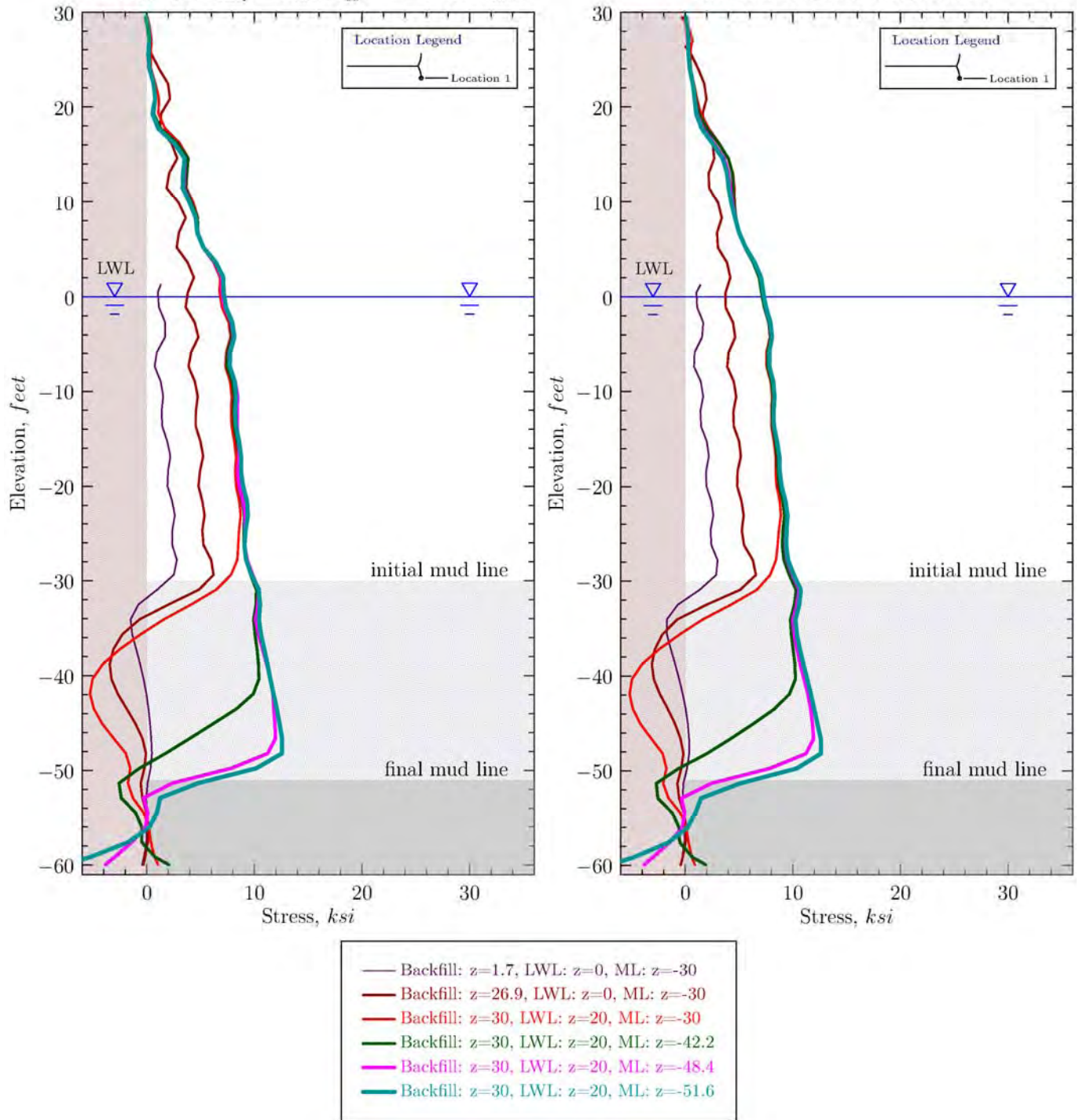


**FIGURE G-26. Profiles of Facewall Hoop Stresses from 2h Reference Model Base Case and Parametric Case with Tailwall Extended 6 Feet**

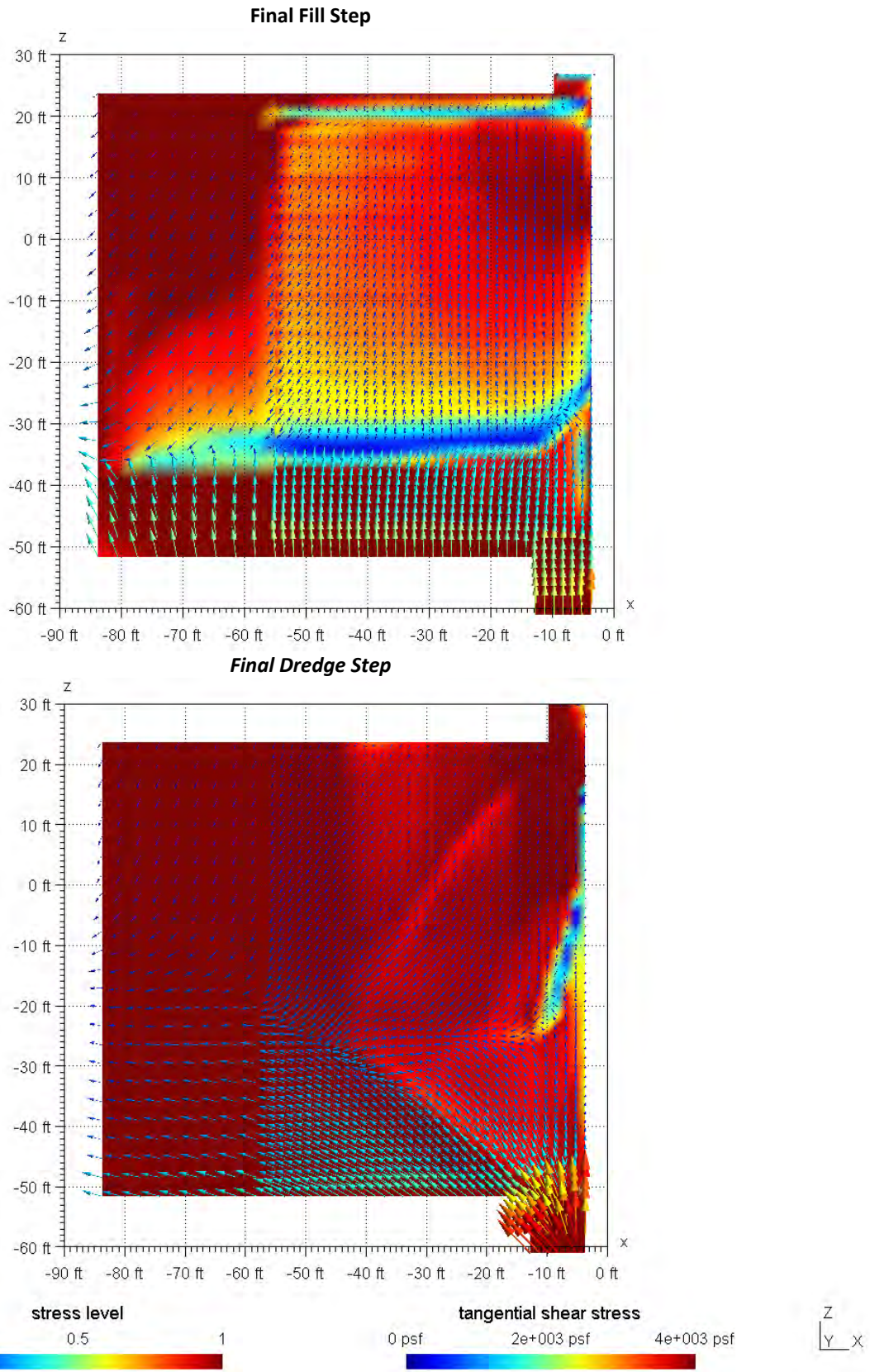


**FIGURE G-27. Contours of Shear Stress Level (Stress/Strength Ratio) and Geogrid Shear Coupling Stress Vectors at End of Filling and Final Dredge Step**

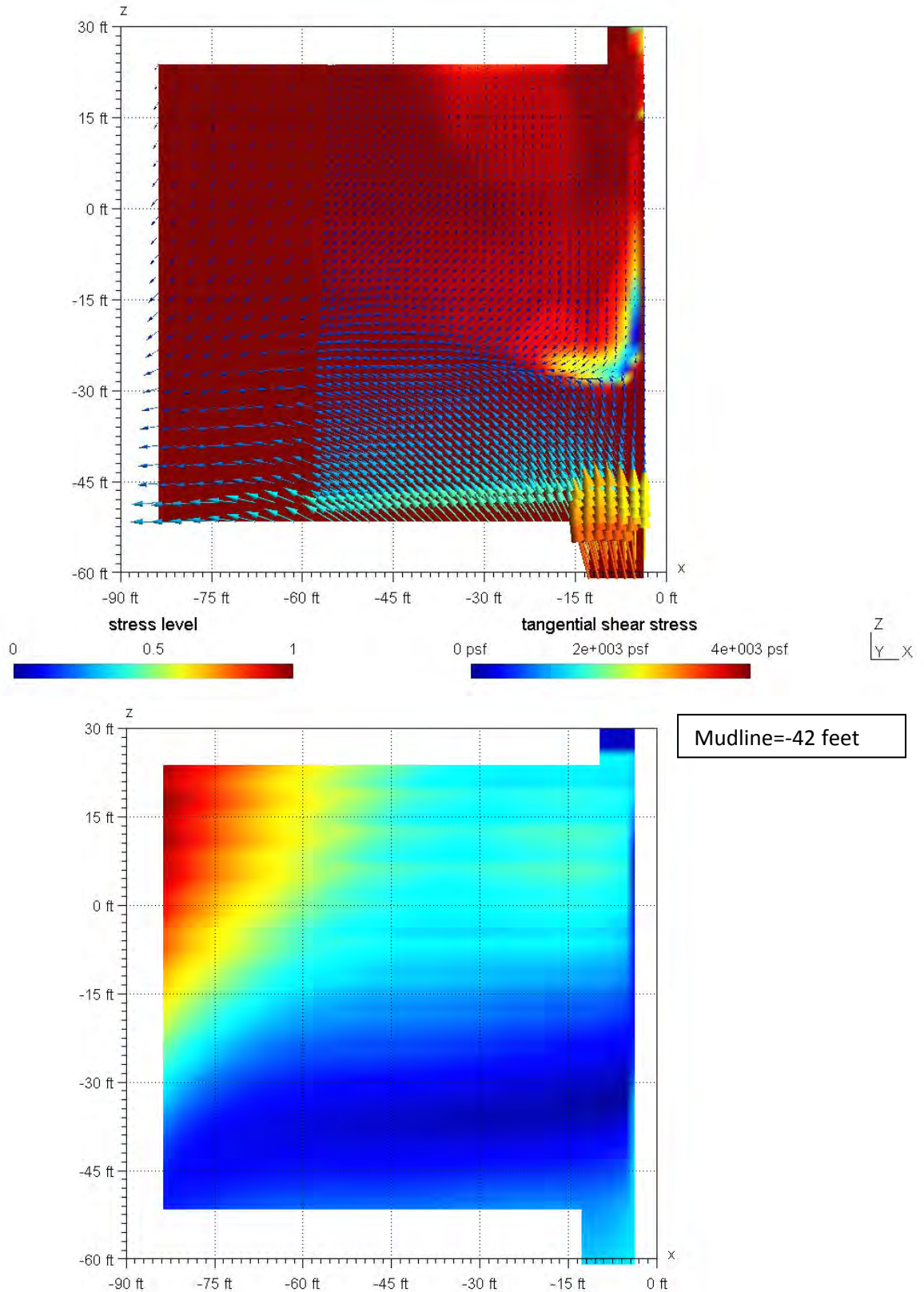
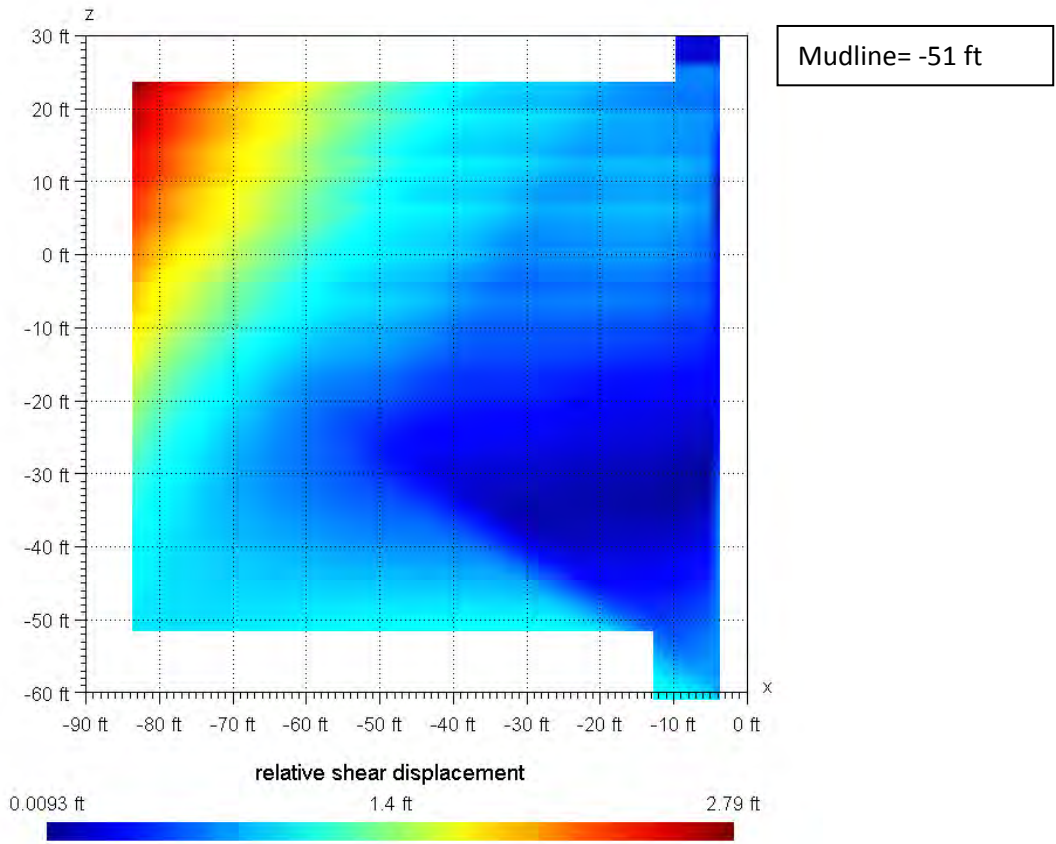


**FIGURE G-28. Contours of Shear Stress Level (Stress/Strength Ratio) and Geogrid Shear Coupling Stress Vectors during Dredging when Mudline is -42**



NOTE: horizontal bands are an artifact of the representation of the OCSP® construction in the model with incremental building of soil backfill and OCSP® wall in horizontal layers above z=-30.

**FIGURE G-29. Contour of Relative Shear Displacement between Geogrid and Adjacent Soil at the End of Dredging in The Base Case Reference Model (mudline at z=-51)**

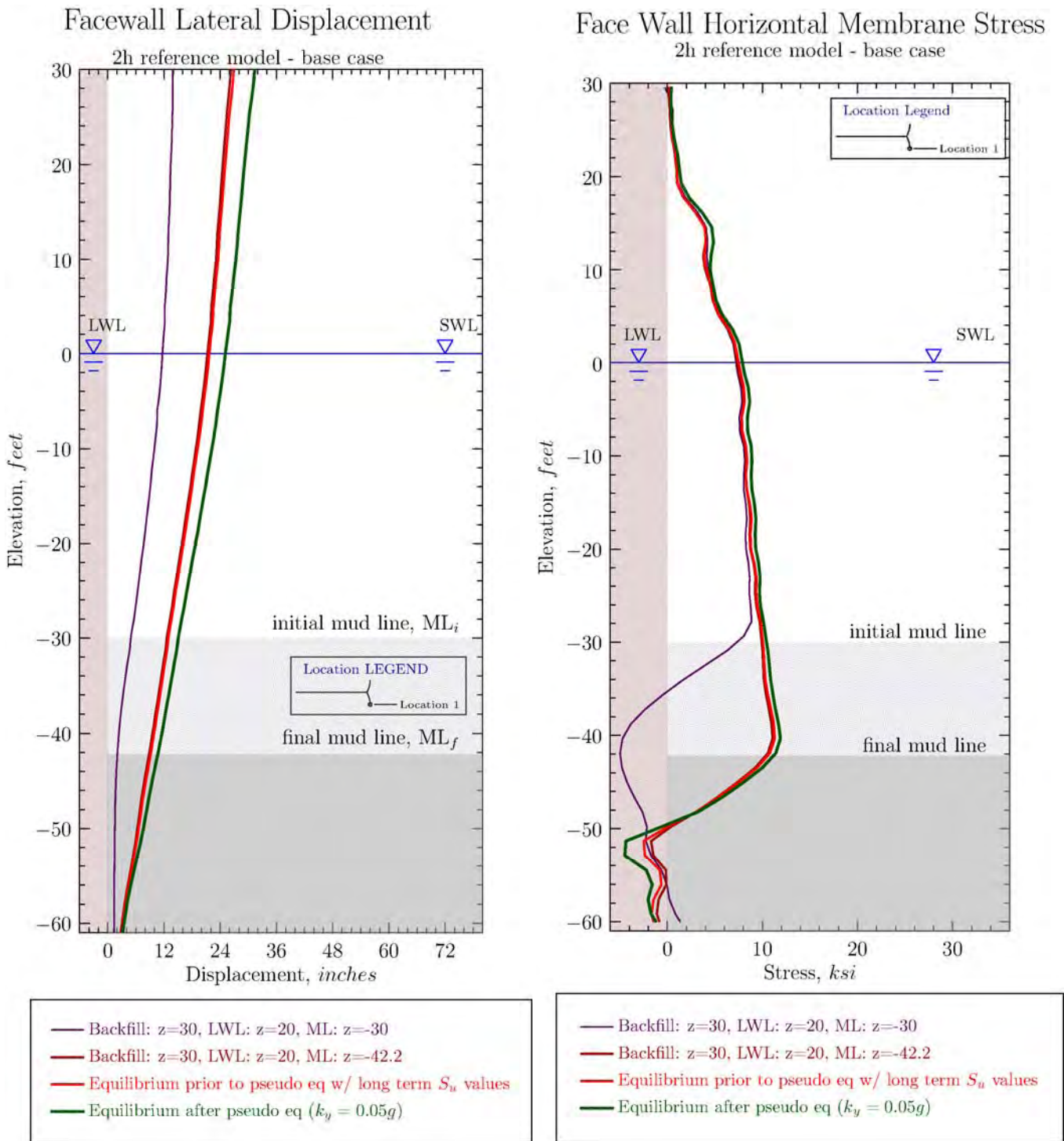


**FIGURE G-30. Facewall Lateral Displacements and Hoop Stresses for Pseudo-Static Earthquake Load on Base Case Model with Mudline at -42**

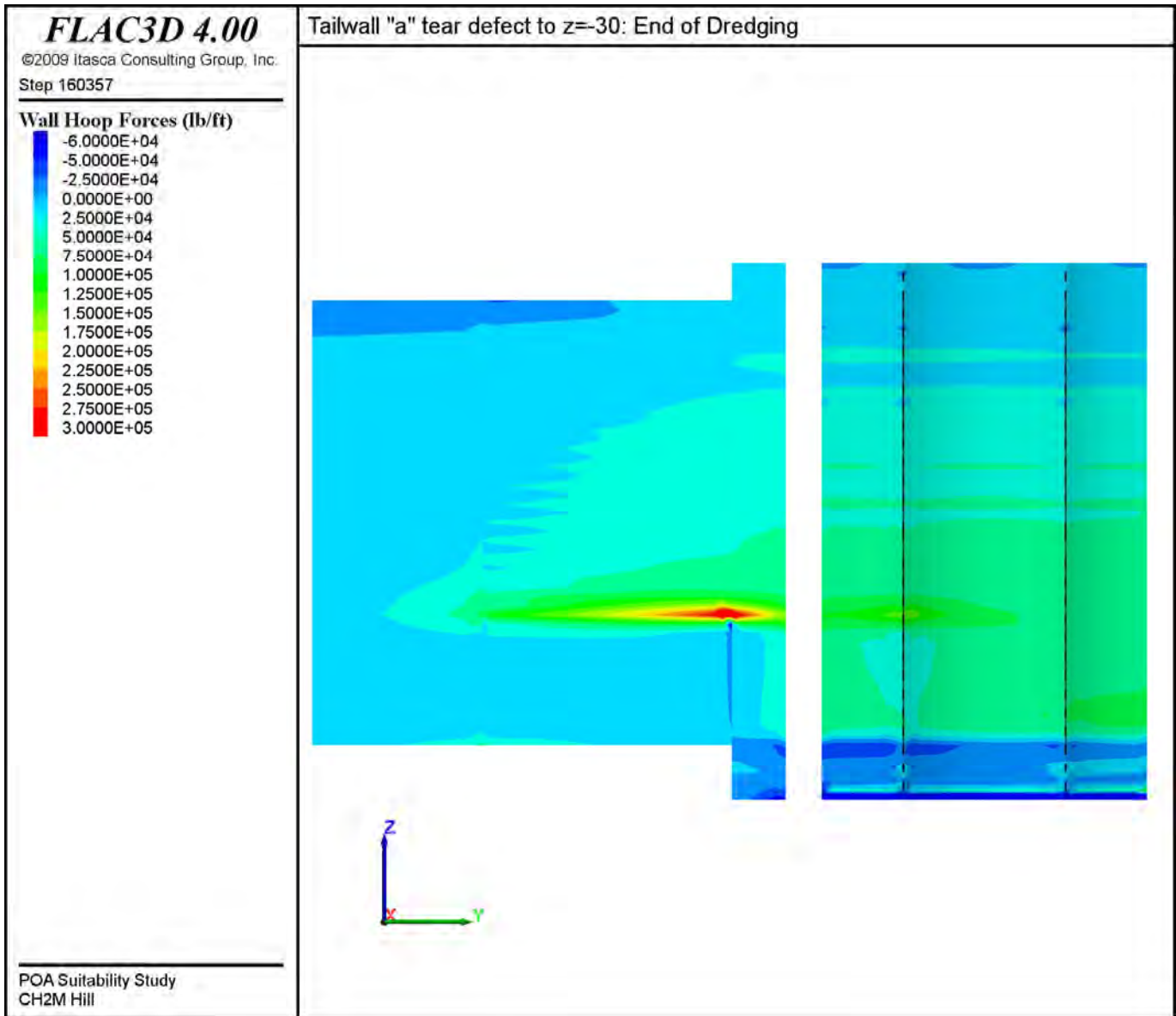
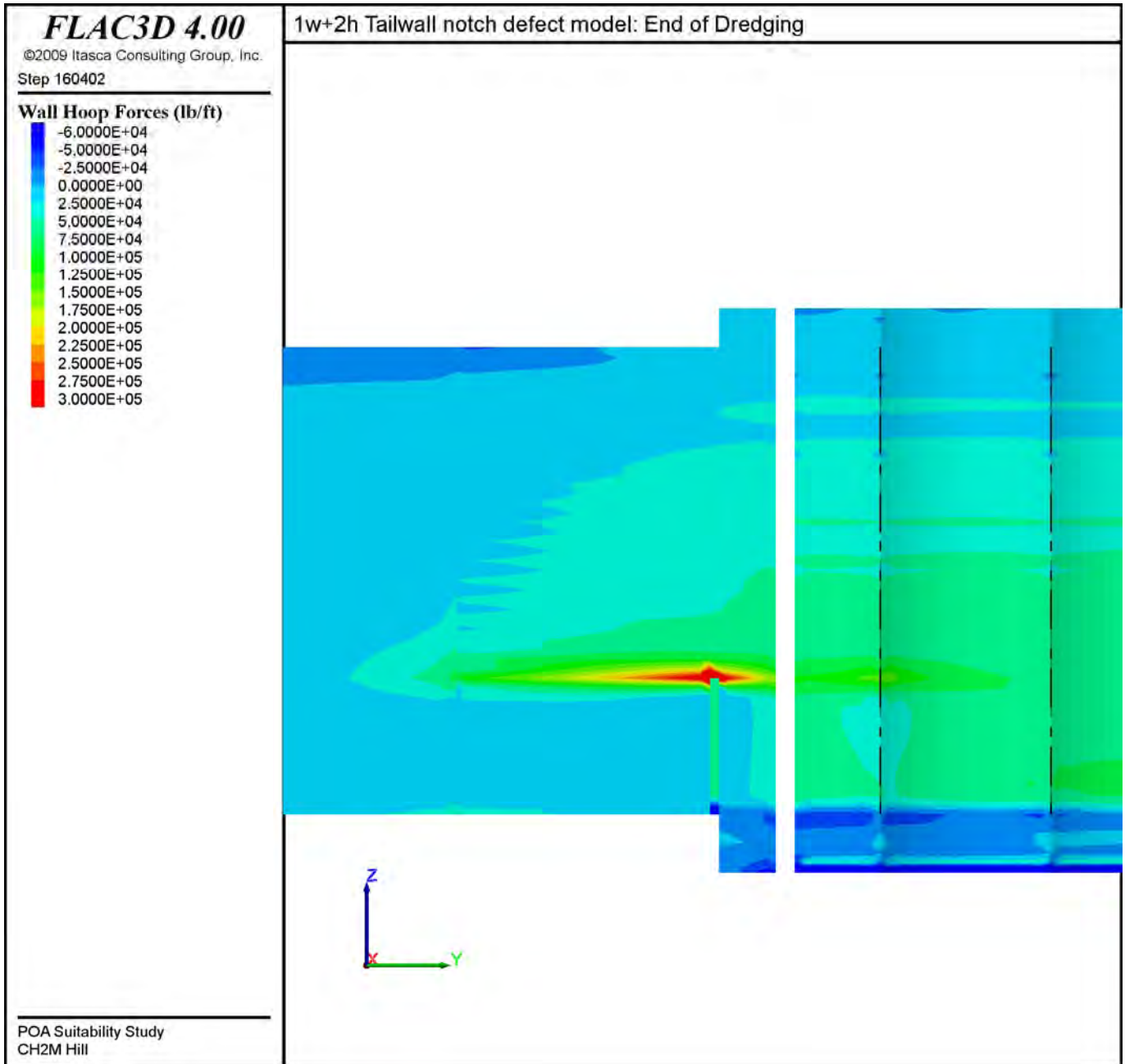


FIGURE G-31. Contours of Tailwall and Facewall Horizontal Stress Resultant for Tailwall Tear Defect to z=-30 in 1w+2h Defect Model



**FIGURE G-32. Contours of Tailwall and Facewall Horizontal Stress Resultant for Tailwall Notch Defect to z=-30 in 1w+2h Defect Model**

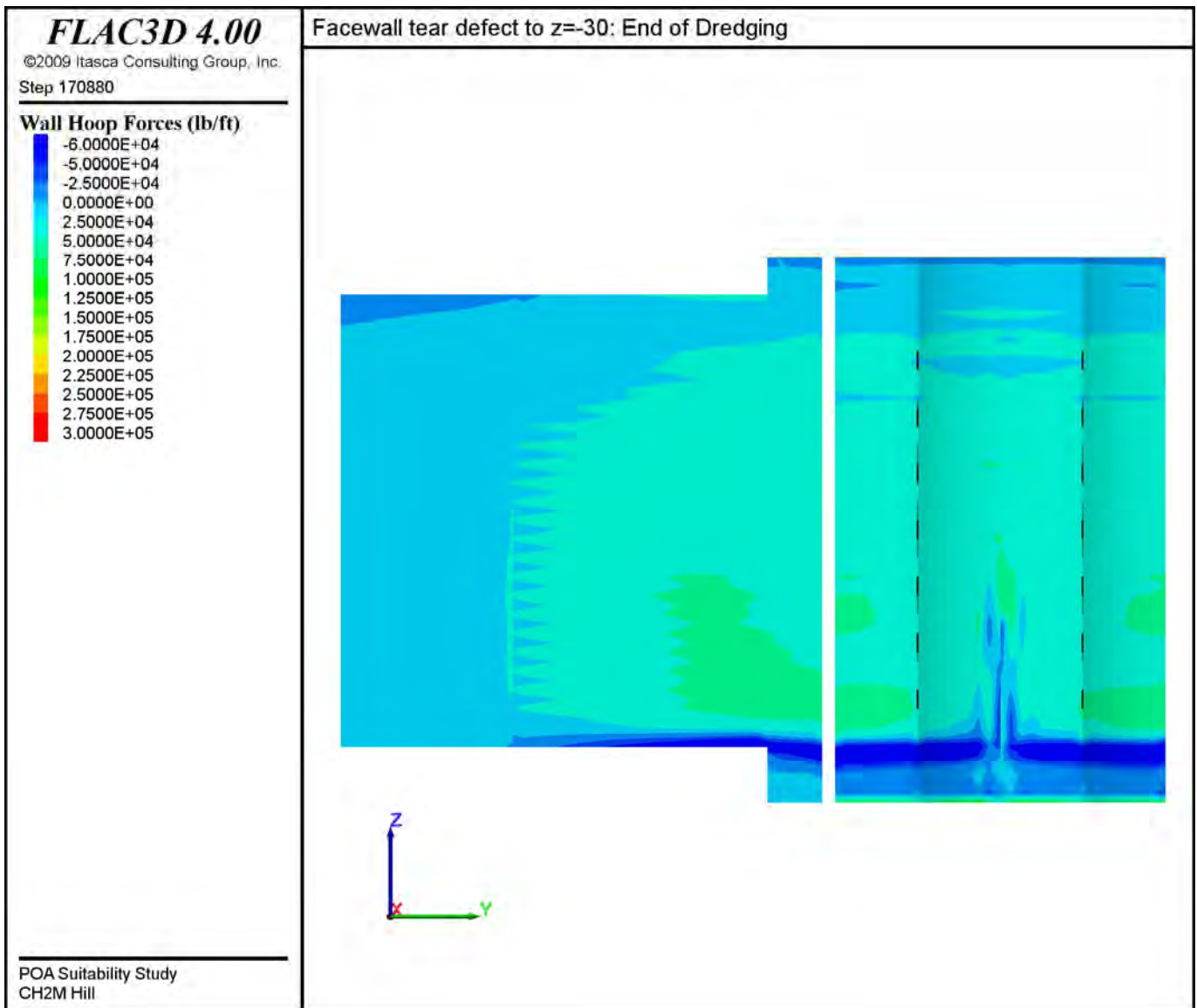


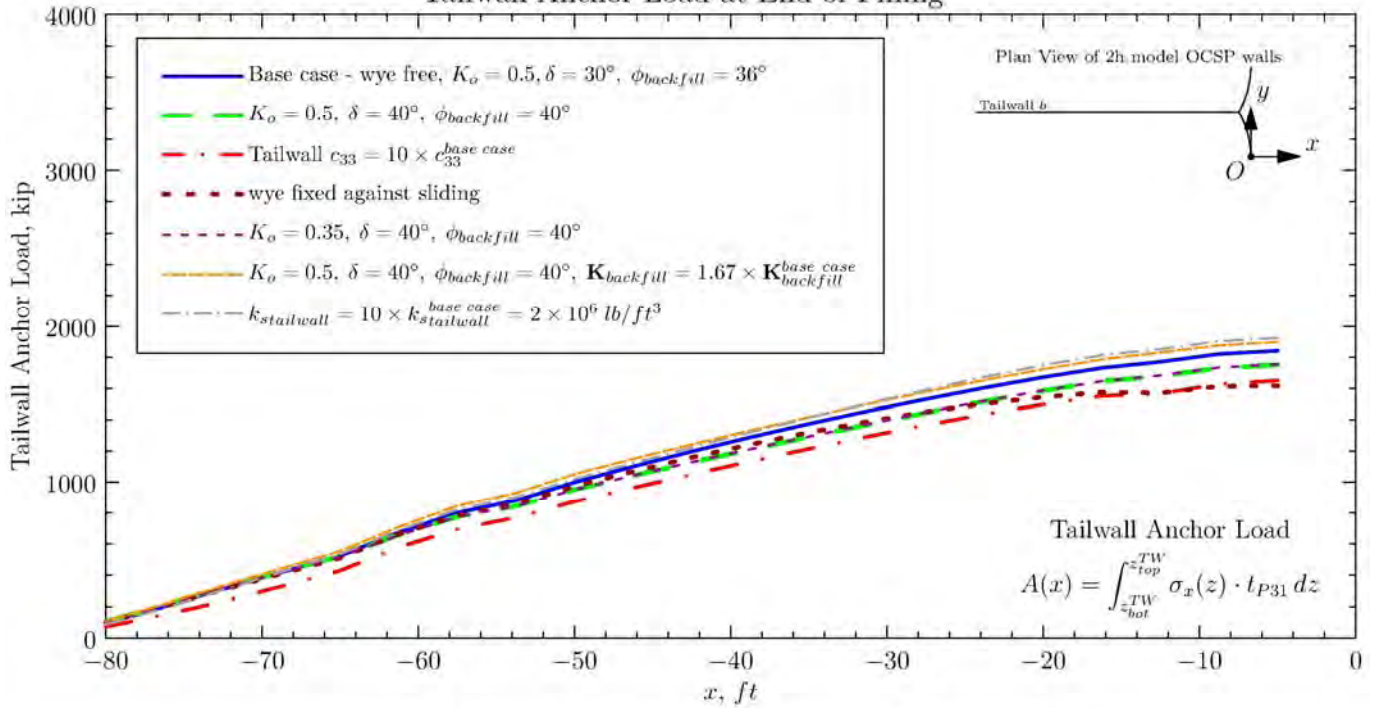
FIGURE G-33. Contours of Tailwall and Facewall Horizontal Stress Resultant for Facewall Tear Defect to z=-30 in 1w+2h Defect Model

**Attachment G-1**  
**Summary Figures for 2h Models**



### 2h models - no defects

#### Tailwall Anchor Load at End of Filling



#### Tailwall Anchor Load during Dredging, mudline z=-42

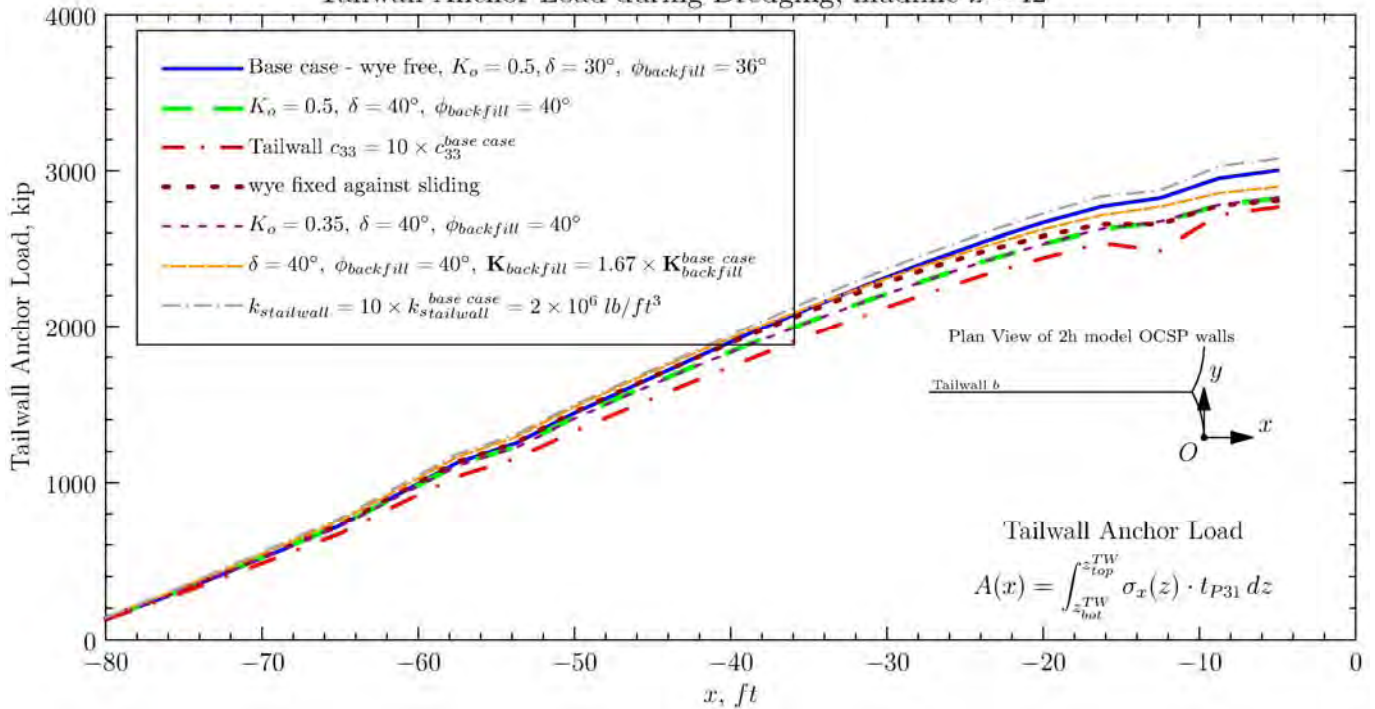


Figure G-1.1. Tailwall Anchor Loads from 2h Base Case and Parametric Models

## Facewall Lateral Displacement 2h Reference Models

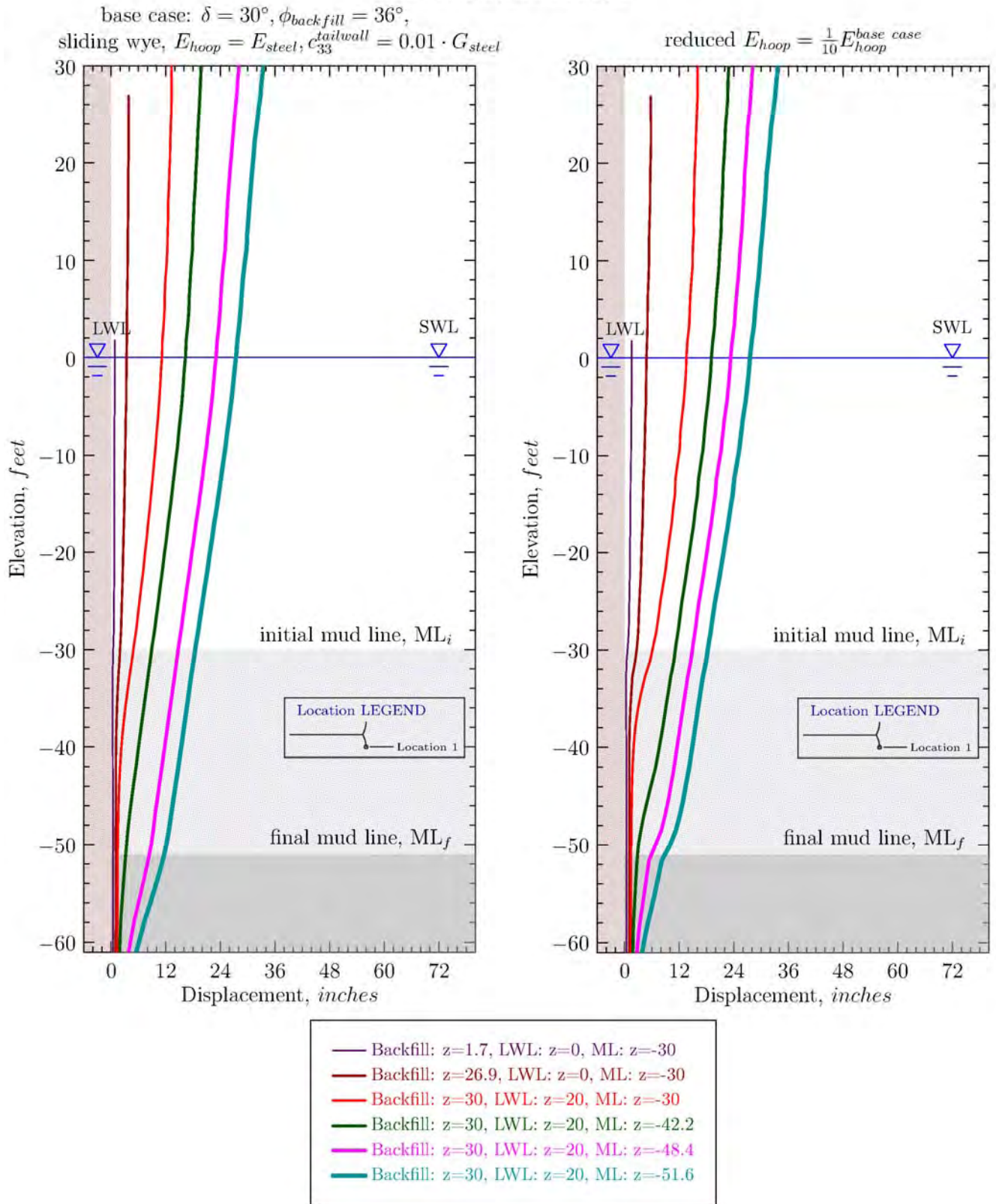


Figure G-1.2. Facewall Lateral Displacement from 2h Base Case and Reduced  $E_{hoop}$  Parametric Case

## Facewall Lateral Displacement 2h Reference Models

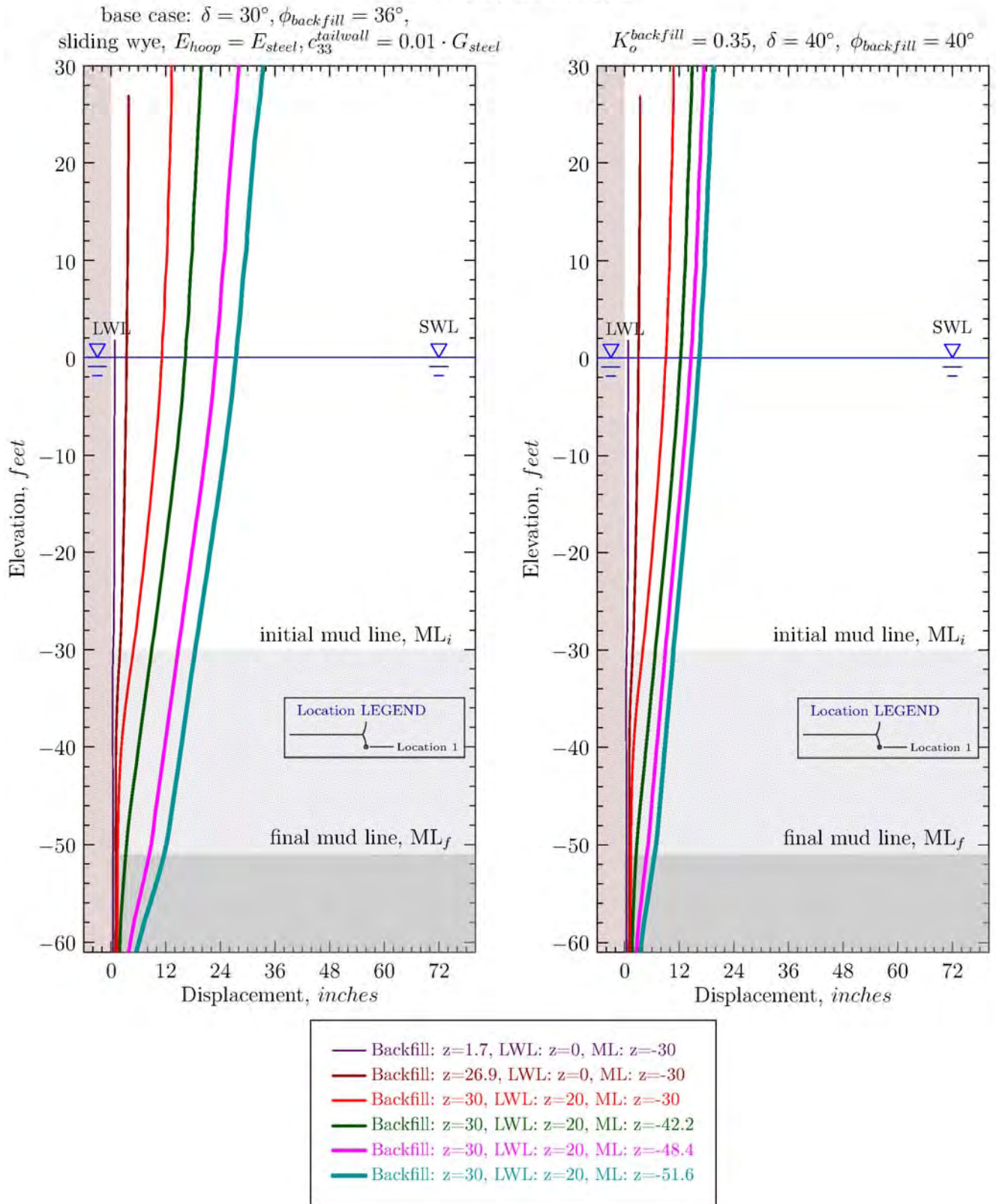


Figure G-1.3. Facewall Lateral Displacement from 2h Base Case and  $\delta=\phi=40^\circ$  with  $K_o=0.35$  for Fill Layer Parametric Case

## Facewall Lateral Displacement 2h Reference Models

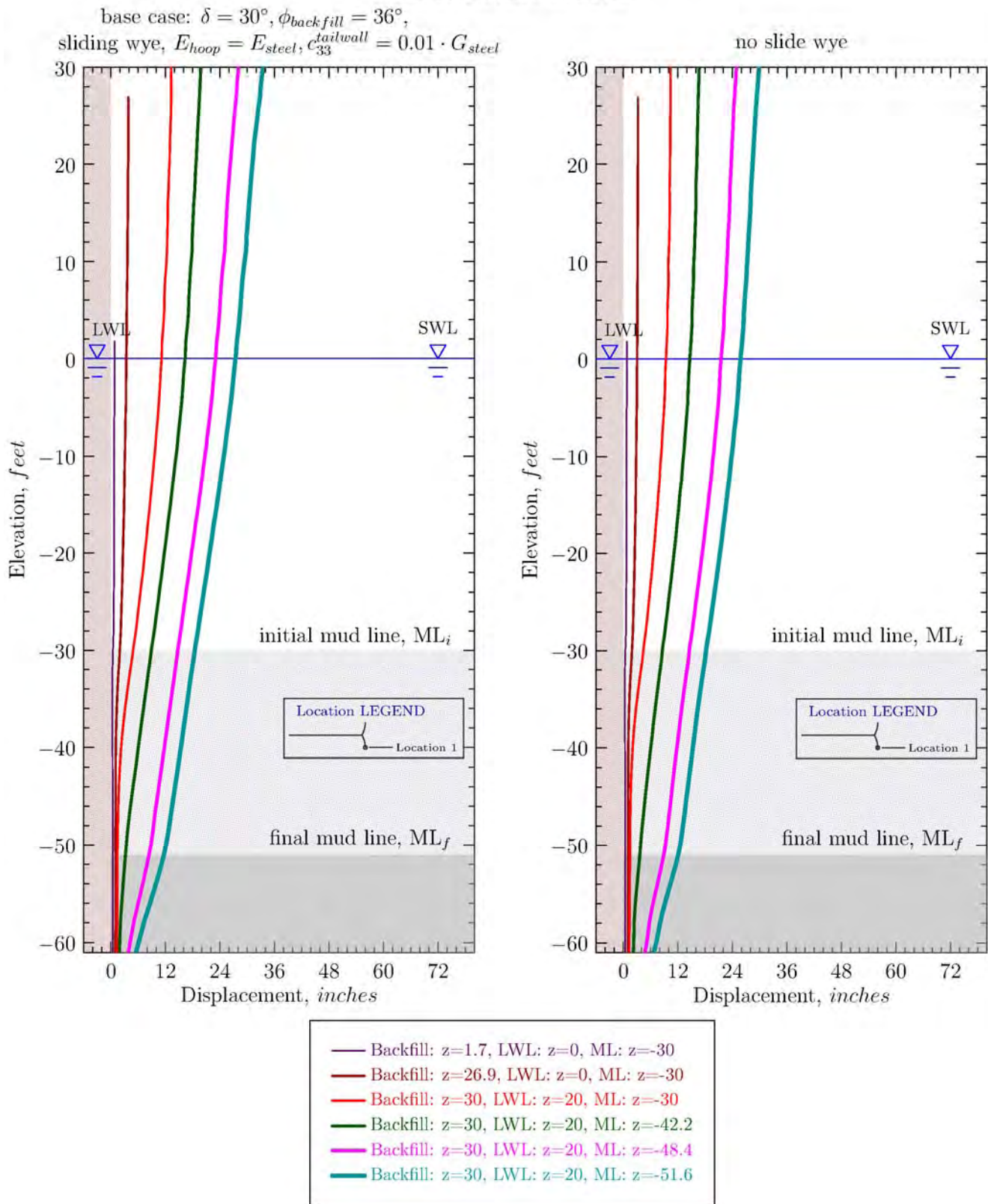


Figure G-1.4. Facewall Lateral Displacement from 2h Base Case and Fixed Wye Connector Parametric Case

## Facewall Lateral Displacement 2h Reference Models

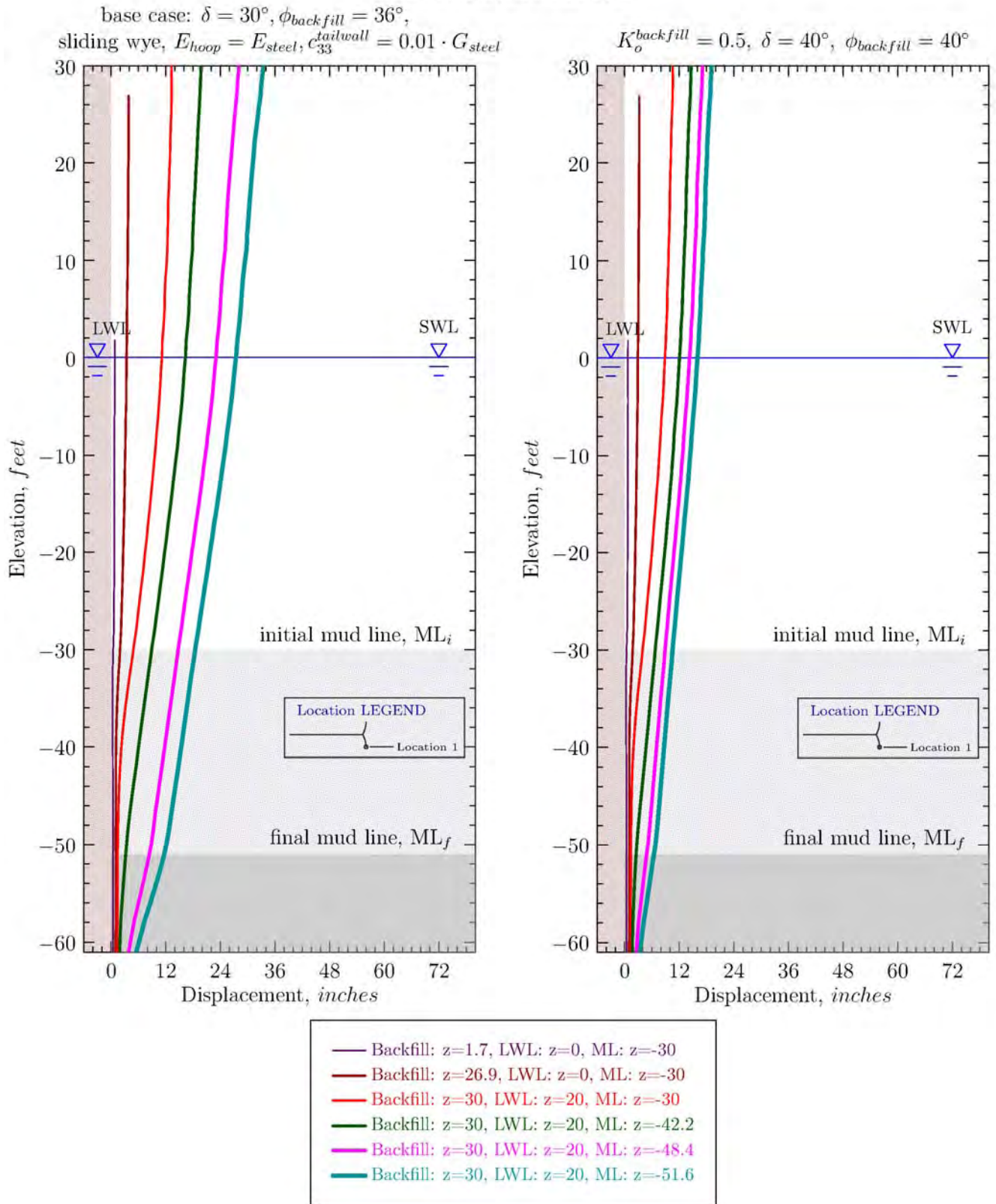


Figure G-1.5. Facewall Lateral Displacement from 2h Base Case and  $\delta=\phi=40^\circ$  Parametric Case

## Facewall Lateral Displacement 2h Reference Models

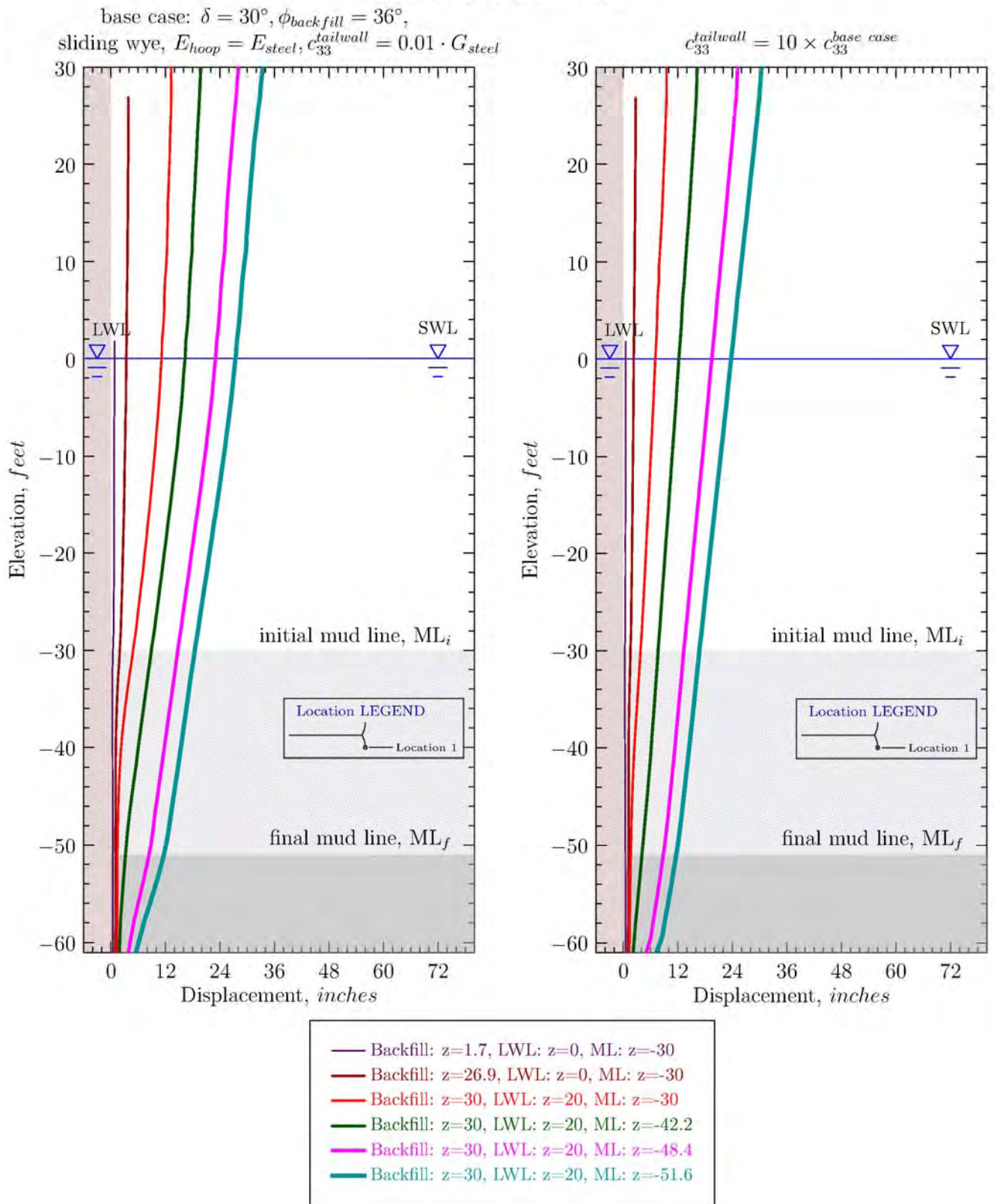


Figure G-1.6. Facewall Lateral Displacement from 2h Base Case and Increased Tailwall Shear Stiffness Parametric Case

## Facewall Lateral Displacement 2h Reference Models

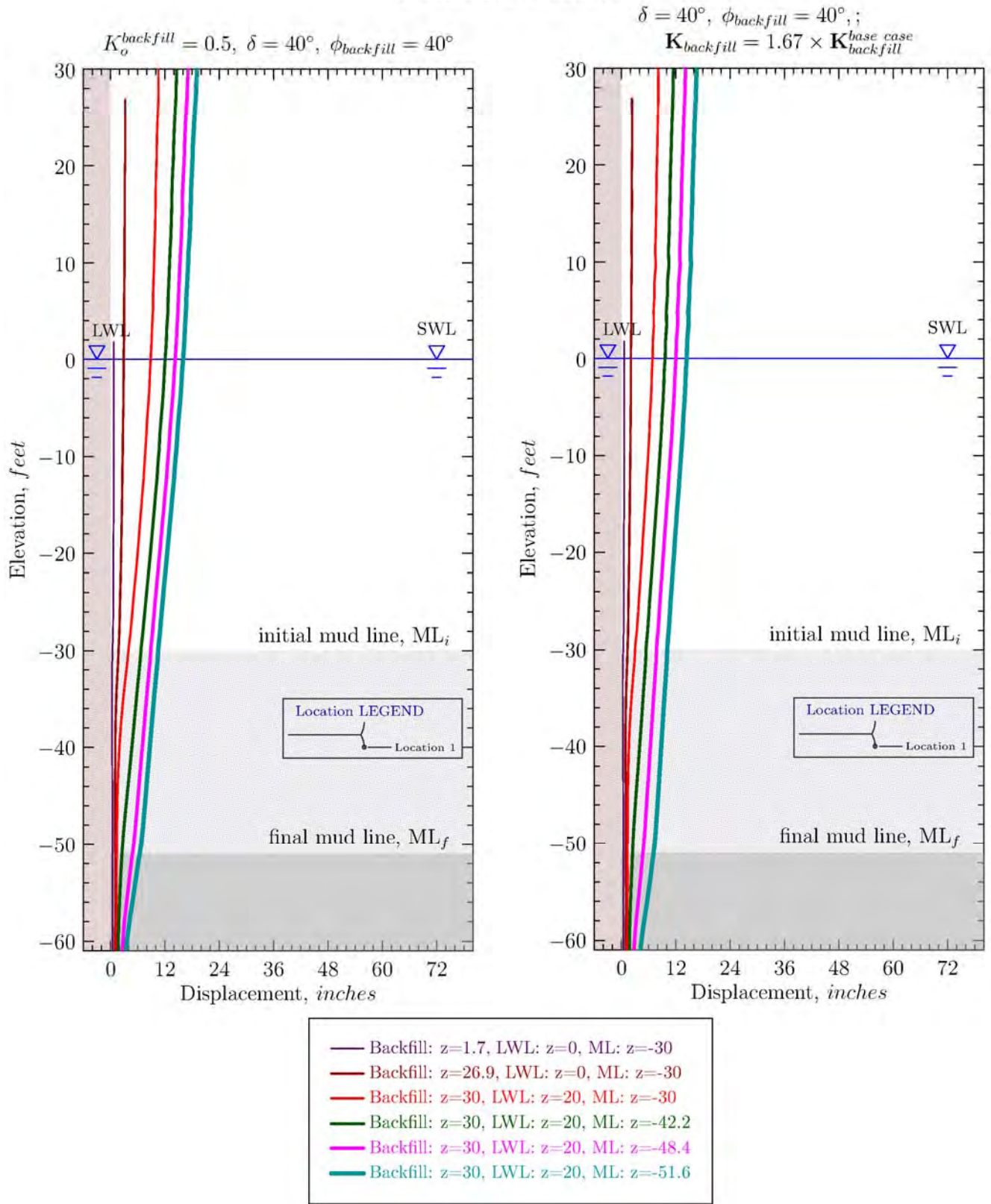


Figure G-1.7. Facewall Lateral Displacement from  $\delta=\phi=40^\circ$  Parametric Case and Increased Backfill Stiffness Number and  $\delta=\phi=40^\circ$  Parametric Case

## Facewall Lateral Displacement 2h Reference Models

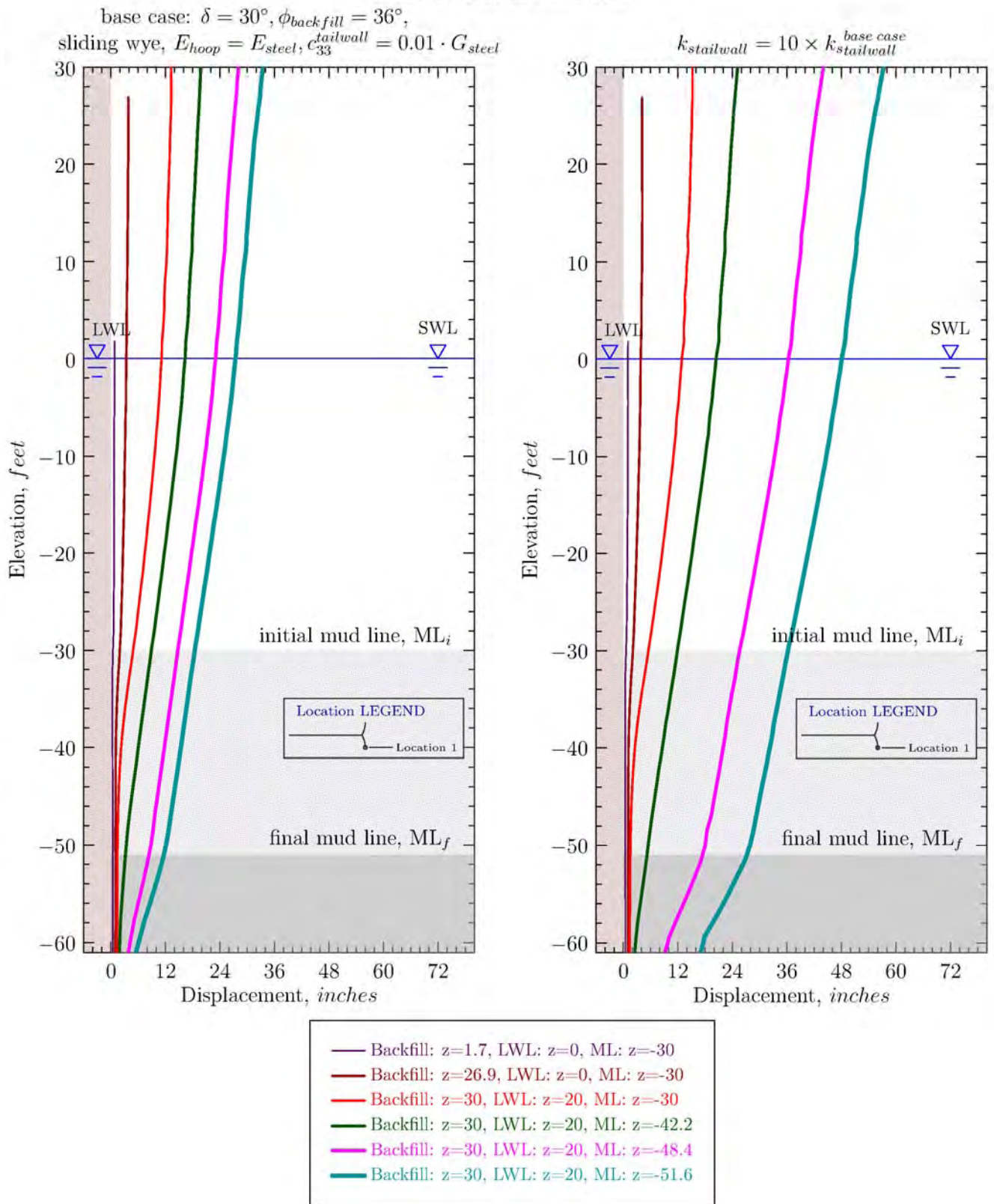


Figure G-1.8. Facewall Lateral Displacement from 2h Base Case and Increased Tailwall Shear Coupling Spring Stiffness Parametric Case

## Facewall Lateral Displacement 2h Reference Models

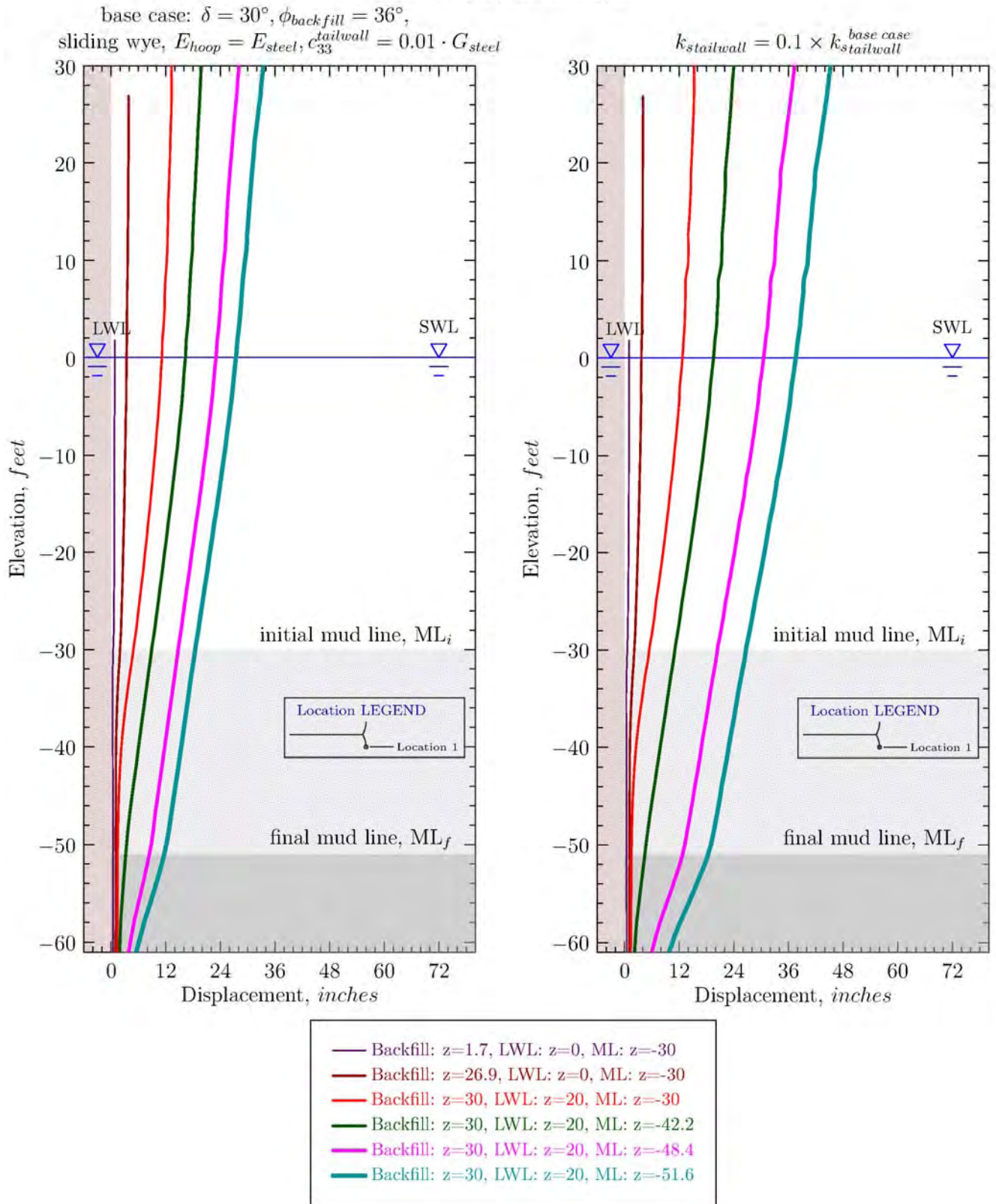


Figure G-1.9. Facewall Lateral Displacement from 2h Base Case and Reduced Tailwall Shear Coupling Spring Stiffness Parametric Case

## Face Wall Horizontal Membrane Stress 2h Reference Models

base case:  $\delta = 30^\circ, \phi_{backfill} = 36^\circ,$   
 sliding wye,  $E_{hoop} = E_{steel}, c_{33}^{tailwall} = 0.01 \cdot G_{steel}$

reduced  $E_{hoop} = \frac{1}{10} E_{hoop}^{base\ case}$

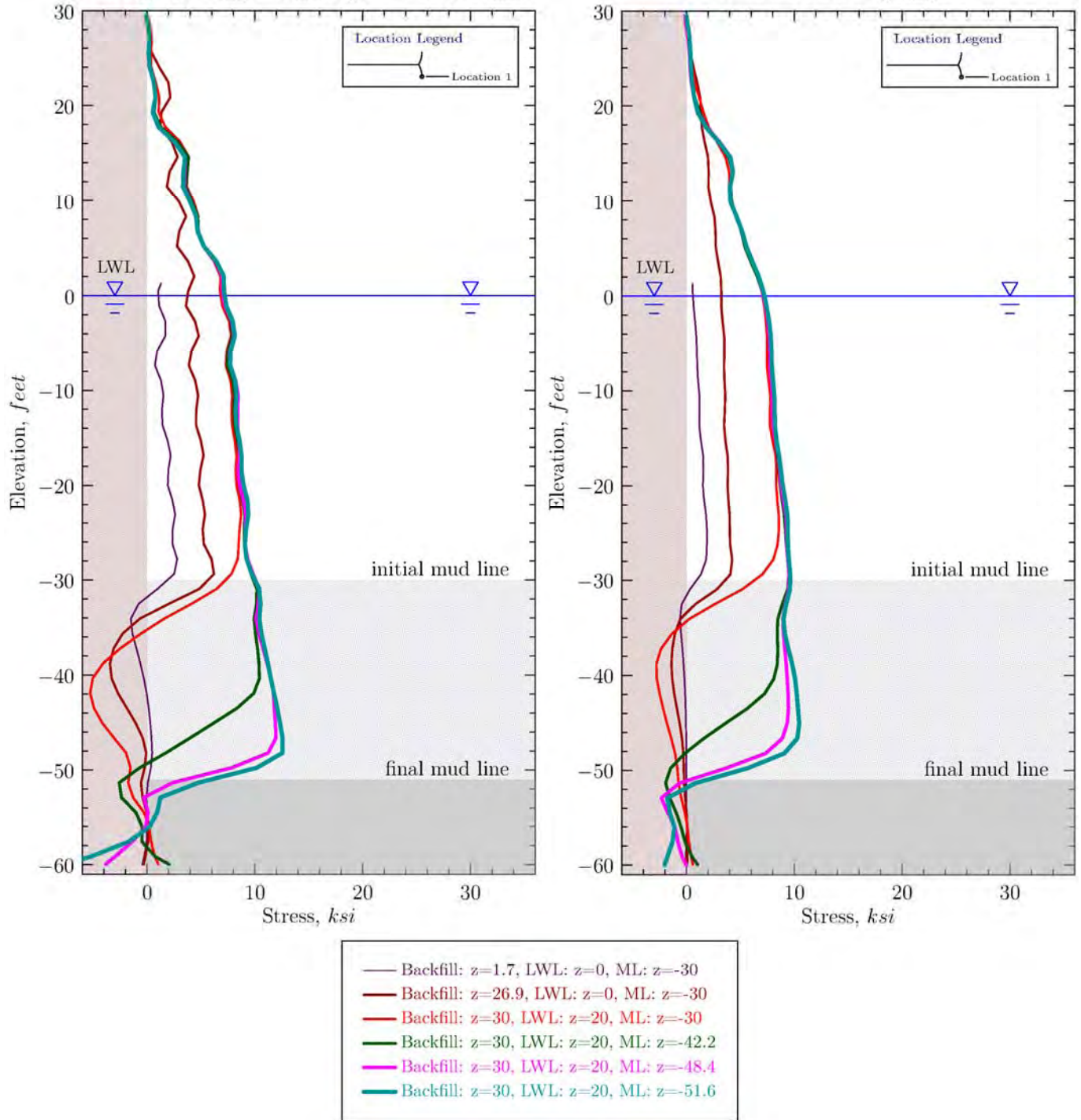


Figure G-1.10. Facewall Hoop Stresses from 2h Base Case and Reduced  $E_{hoop}$  Parametric Case

### Face Wall Horizontal Membrane Stress 2h Reference Models

base case:  $\delta = 30^\circ, \phi_{backfill} = 36^\circ,$   
sliding wye,  $E_{hoop} = E_{steel}, c_{33}^{tailwall} = 0.01 \cdot G_{steel}$

$K_o^{backfill} = 0.35, \delta = 40^\circ, \phi_{backfill} = 40^\circ$

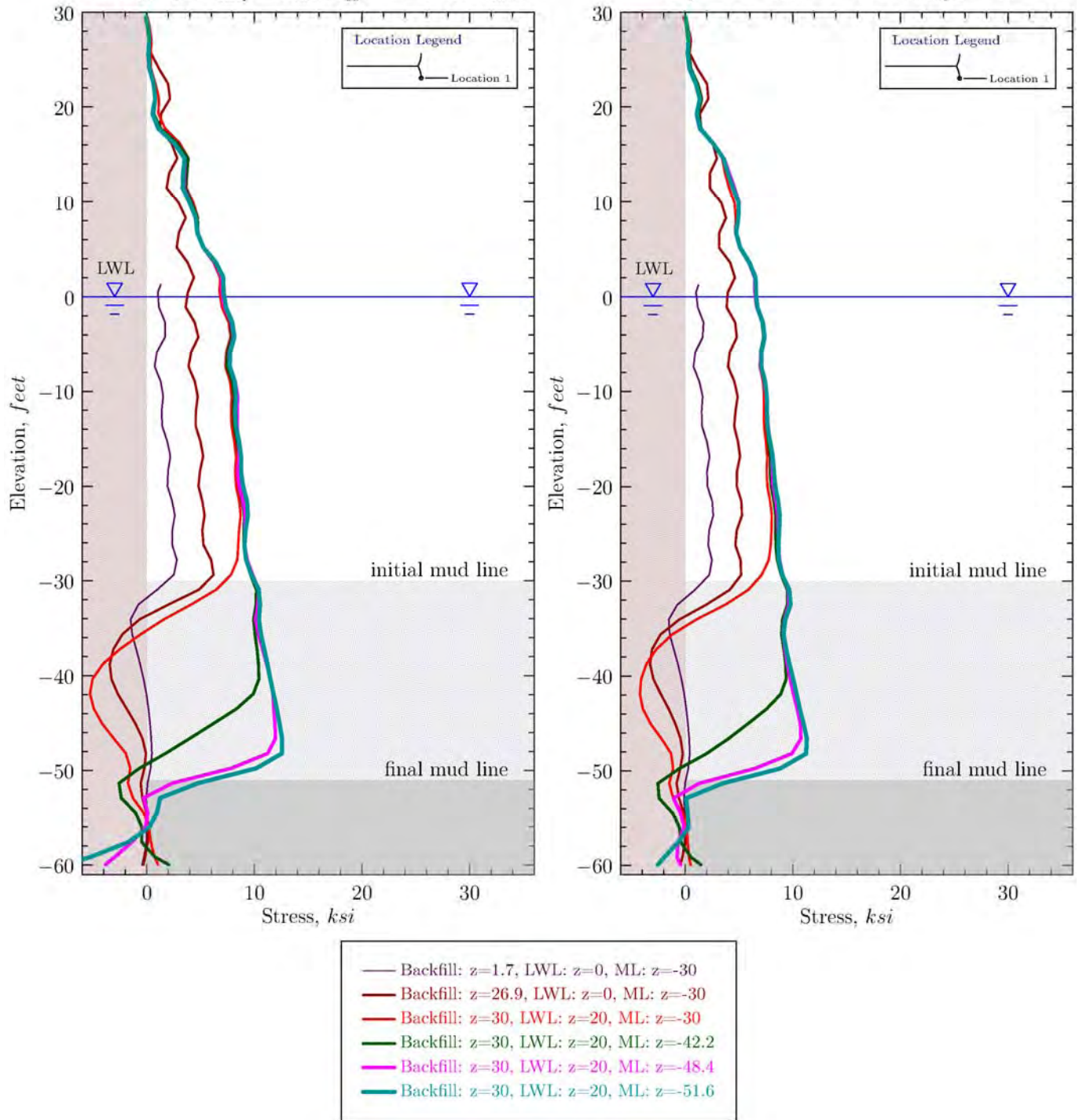


Figure G-1.11. Facewall Hoop Stresses from 2h Base Case and  $\delta=\phi=40^\circ$  with  $K_o=0.35$  for Fill Layer Parametric Case

## Face Wall Horizontal Membrane Stress 2h Reference Models

base case:  $\delta = 30^\circ, \phi_{backfill} = 36^\circ,$   
 sliding wye,  $E_{hoop} = E_{steel}, c_{33}^{tailwall} = 0.01 \cdot G_{steel}$

no slide wye

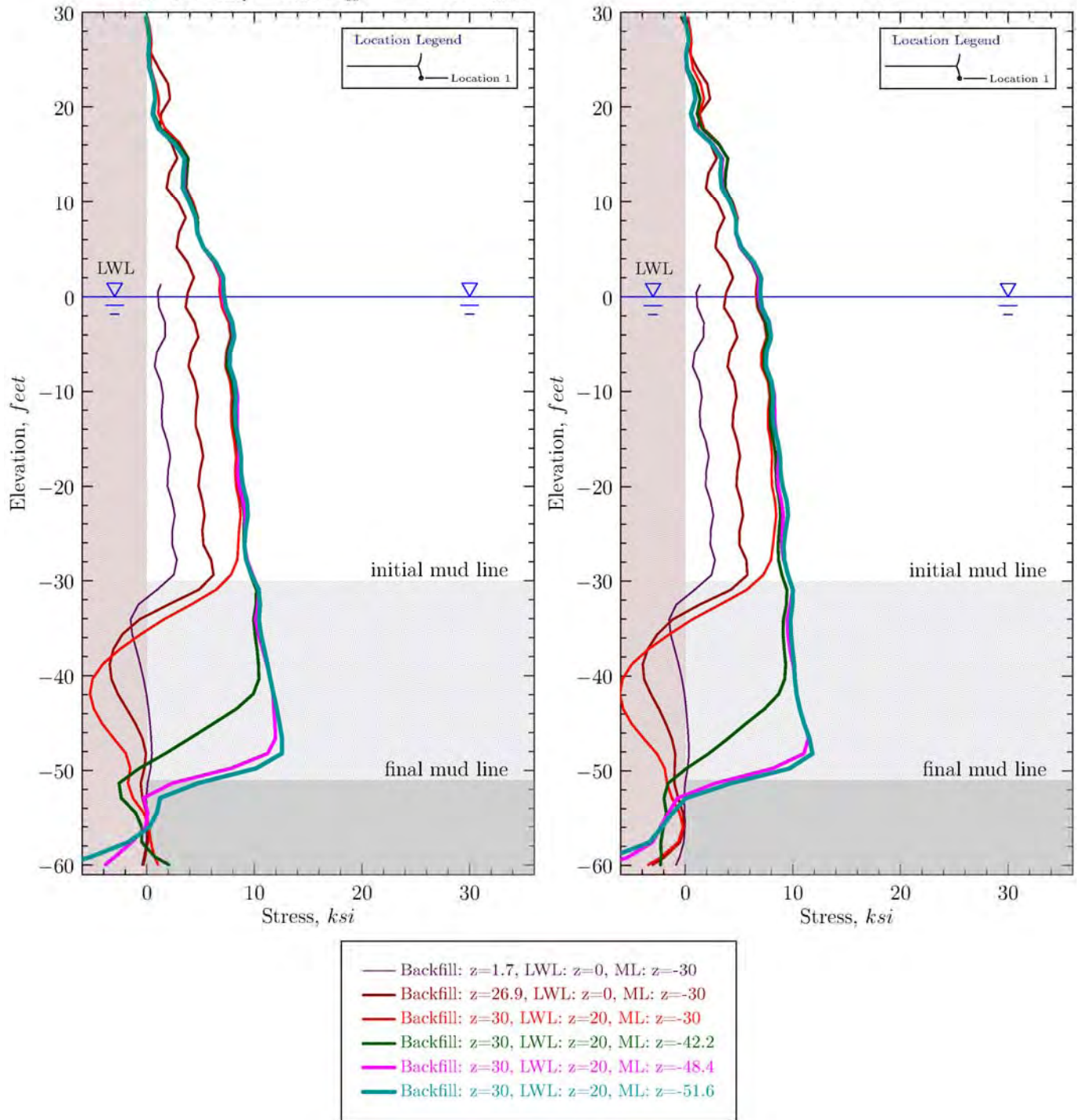


Figure G-1.12. Facewall Hoop Stresses from 2h Base Case and Fixed Wye Connector Parametric Case

### Face Wall Horizontal Membrane Stress 2h Reference Models

base case:  $\delta = 30^\circ, \phi_{backfill} = 36^\circ,$   
sliding wye,  $E_{hoop} = E_{steel}, c_{33}^{tailwall} = 0.01 \cdot G_{steel}$

$K_o^{backfill} = 0.5, \delta = 40^\circ, \phi_{backfill} = 40^\circ$

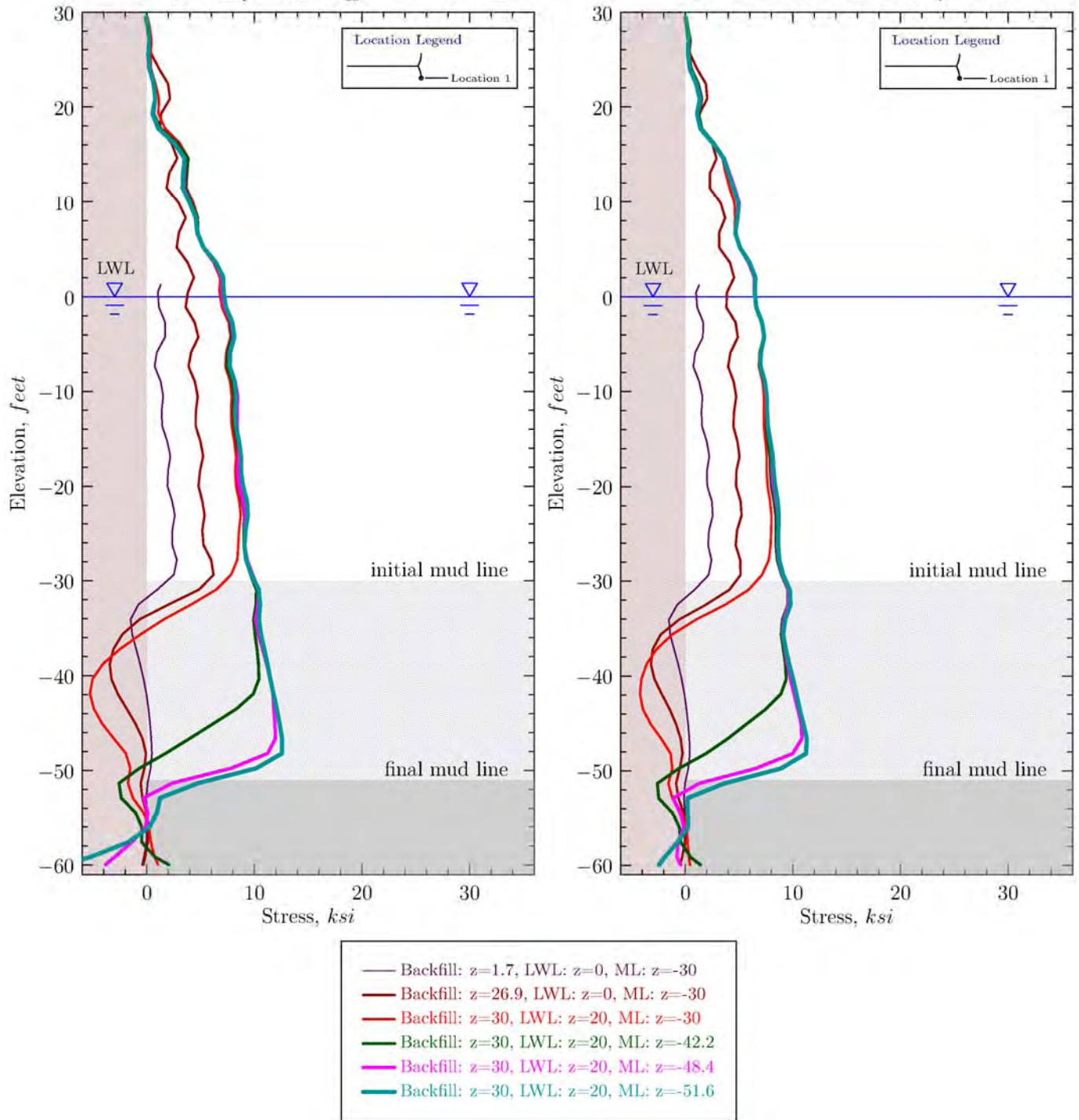


Figure G-1.13. Facewall Hoop Stresses from 2h Base Case and  $\delta=\phi=40^\circ$  Parametric Case

## Face Wall Horizontal Membrane Stress 2h Reference Models

base case:  $\delta = 30^\circ, \phi_{backfill} = 36^\circ,$   
 sliding wye,  $E_{hoop} = E_{steel}, c_{33}^{tailwall} = 0.01 \cdot G_{steel}$

$c_{33}^{tailwall} = 10 \times c_{33}^{base\ case}$

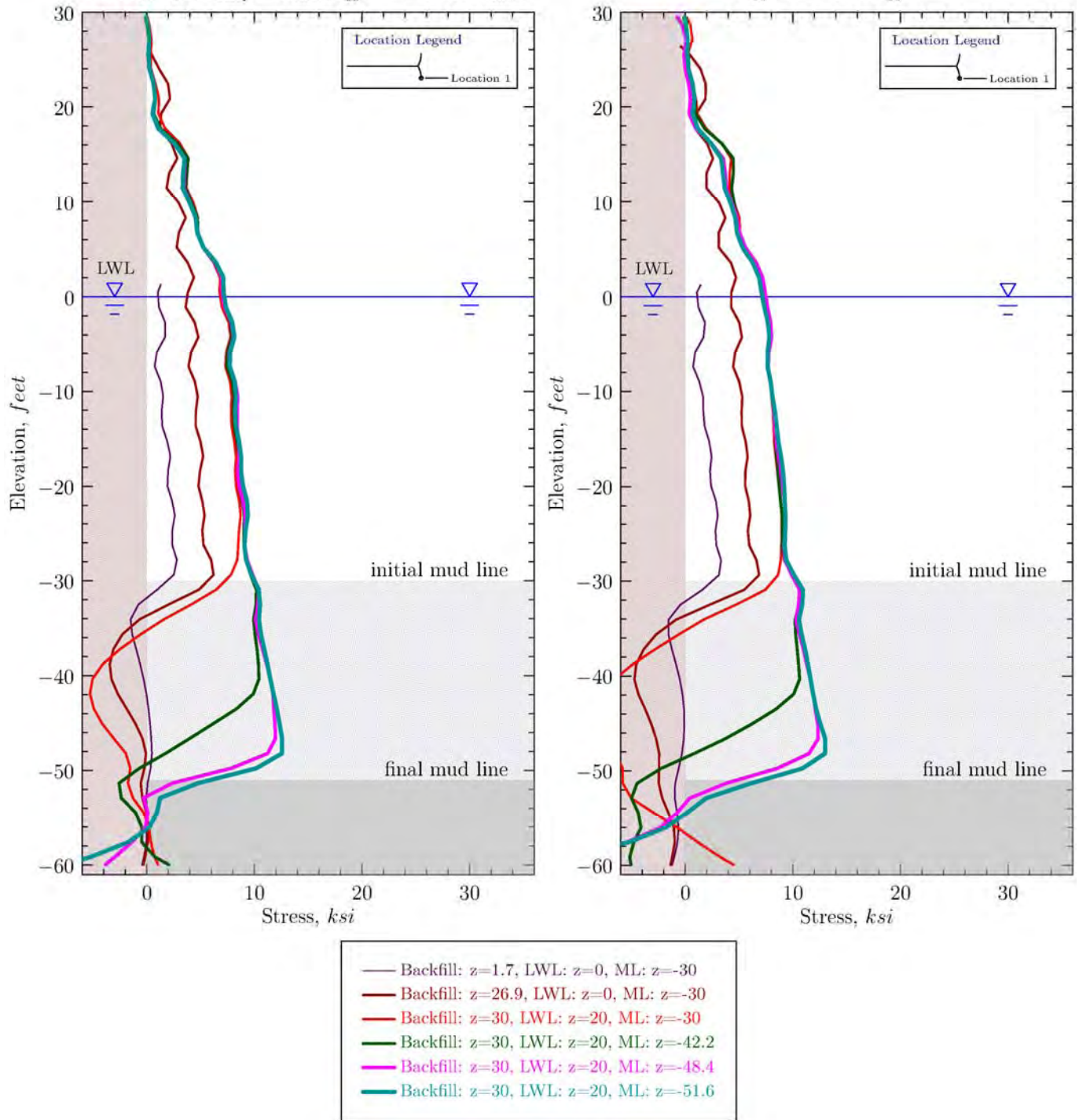


Figure G-1.14. Facewall Lateral Displacement from 2h Base Case and Increased Tailwall Shear Stiffness Parametric Case

### Face Wall Horizontal Membrane Stress 2h Reference Models

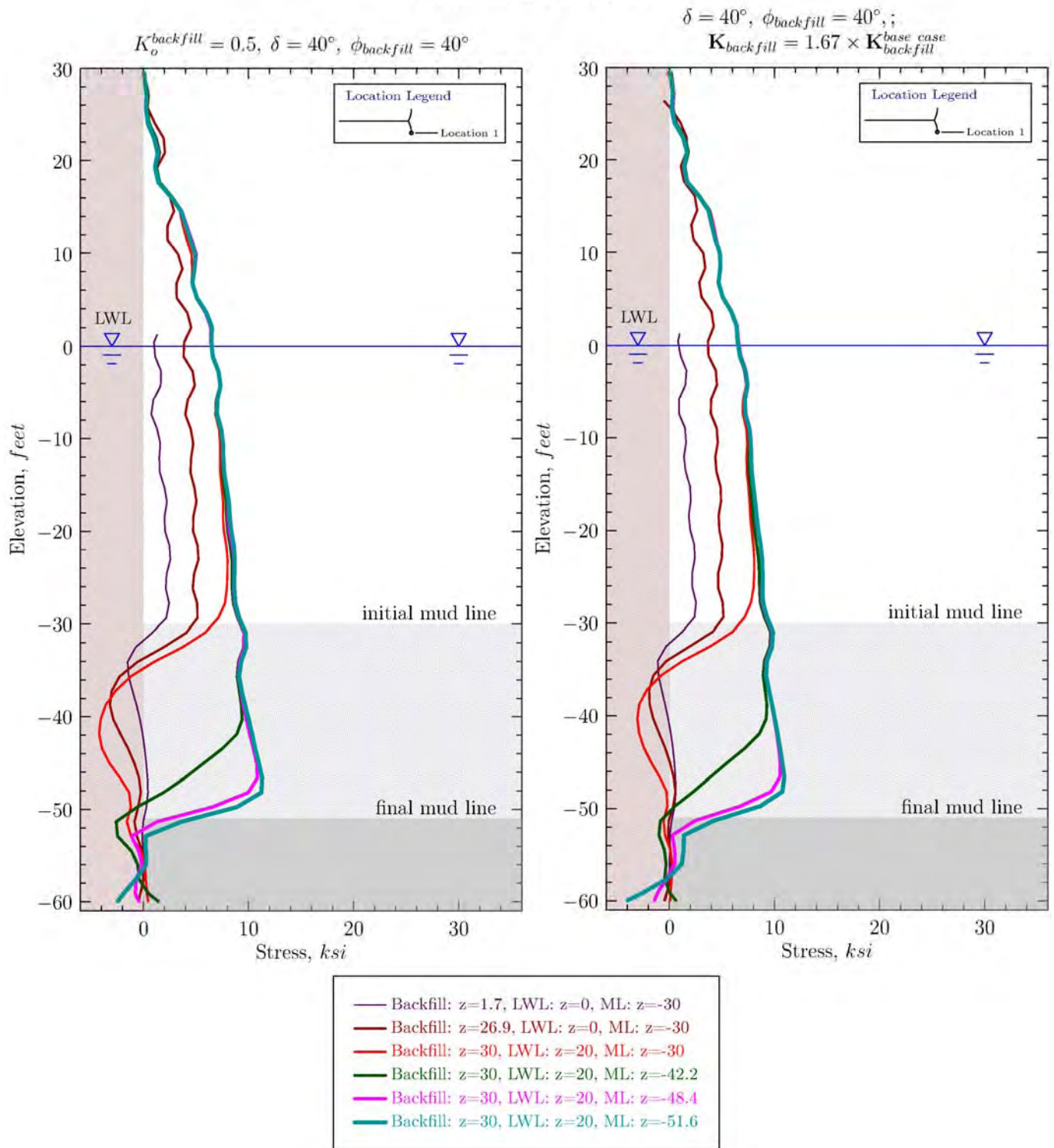


Figure G-1.15. Facewall Hoop Stresses from  $\delta=\phi=40^\circ$  Parametric Case and Increased Backfill Stiffness Number and  $\delta=\phi=40^\circ$  Parametric Case

## Face Wall Horizontal Membrane Stress 2h Reference Models

base case:  $\delta = 30^\circ, \phi_{backfill} = 36^\circ,$   
 sliding wye,  $E_{hoop} = E_{steel}, c_{33}^{tailwall} = 0.01 \cdot G_{steel}$

$k_{stailwall} = 10 \times k_{stailwall}^{base\ case}$

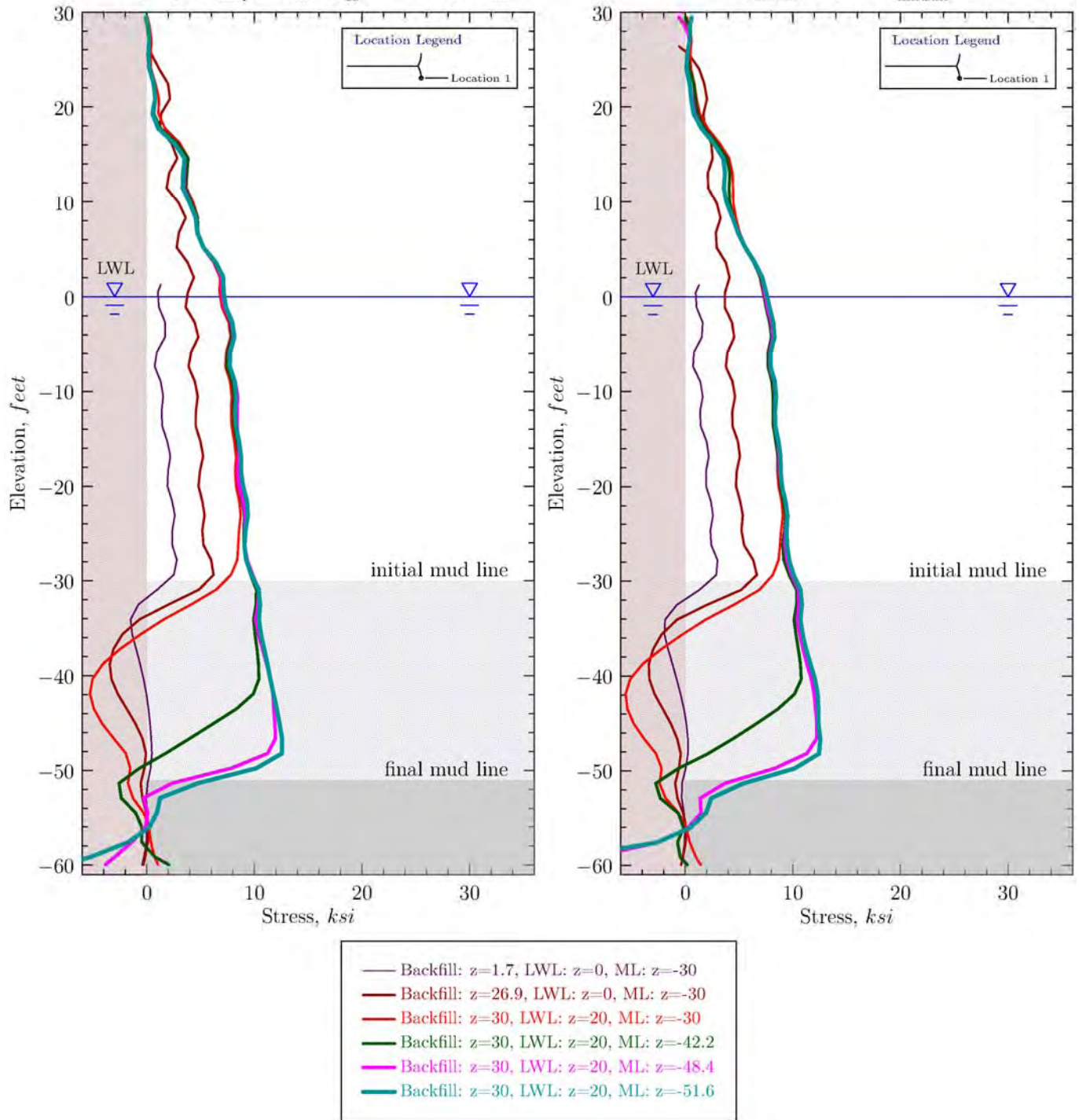


Figure G-1.16. Facewall Lateral Displacement from Base Case and Increased Tailwall Shear Coupling Spring Stiffness Parametric Case

### Face Wall Horizontal Membrane Stress 2h Reference Models

base case:  $\delta = 30^\circ, \phi_{backfill} = 36^\circ,$   
sliding wye,  $E_{hoop} = E_{steel}, c_{33}^{tailwall} = 0.01 \cdot G_{steel}$

$k_{tailwall} = 0.1 \times k_{tailwall}^{base\ case}$

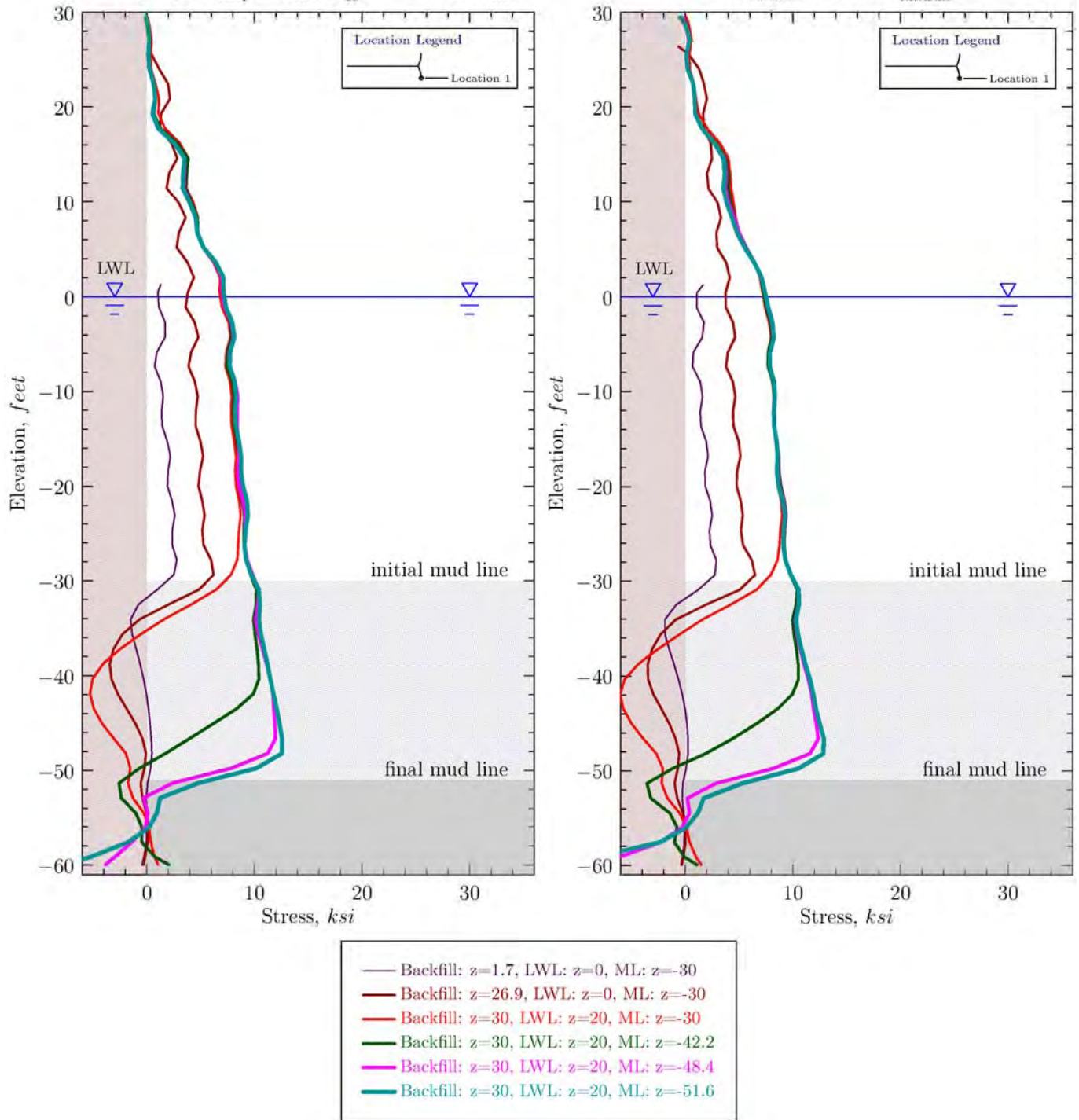


Figure G-1.17. Facewall Lateral Displacement from Base Case and Reduced Tailwall Shear Coupling Spring Stiffness Parametric Case

Tail Wall Horizontal Membrane Stress Profiles from *FLAC*<sup>3D</sup> local model

base case:  $\delta = 30^\circ$ ,  $\phi_{backfill} = 36^\circ$ ,  
 sliding wye,  $E_{hoop} = E_{steel}$ ,  $c_{tailwall}^{int} = 0.01 \cdot G_{steel}$

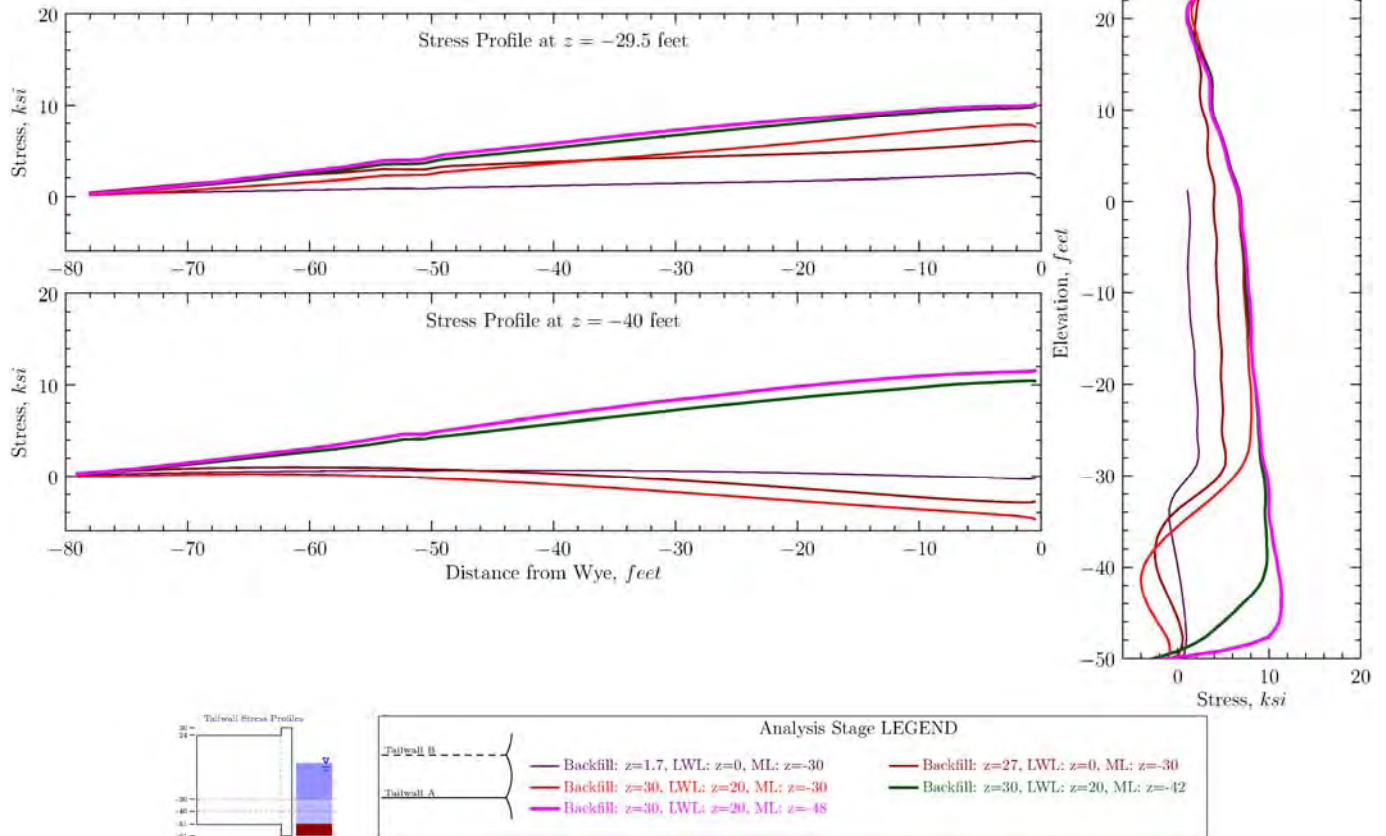


Figure G-1.18. Profiles of Tailwall Hoop Stresses for Base Case

Tail Wall Horizontal Membrane Stress Profiles from *FLAC<sup>3D</sup>* local model

$$\text{reduced } E_{hoop} = \frac{1}{10} E_{hoop}^{base\ case}$$

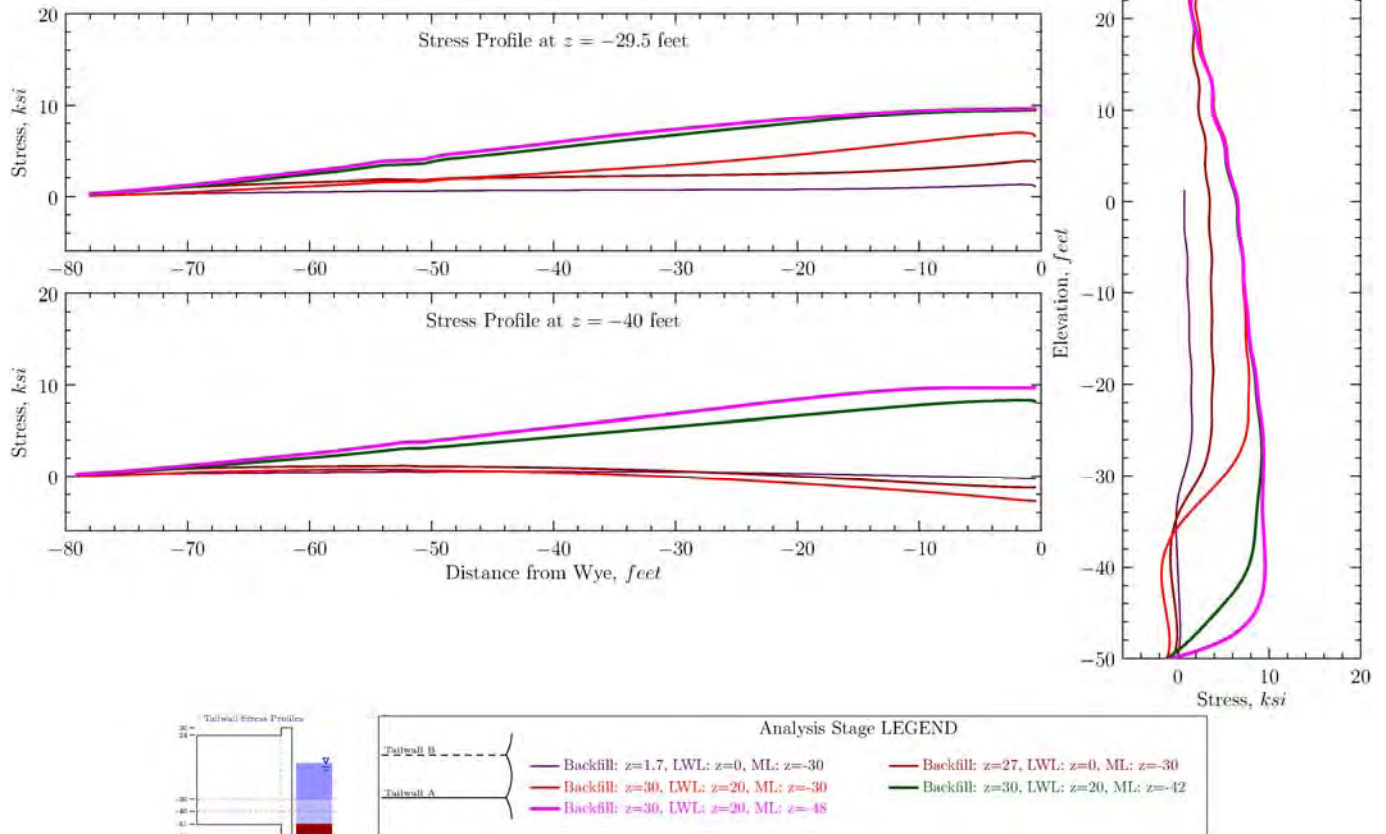


Figure G-1.19. Profiles of Tailwall Hoop Stresses for Reduced  $E_{hoop}$  Parametric Case

Tail Wall Horizontal Membrane Stress Profiles from *FLAC*<sup>3D</sup> local model

$$K_q^{backfill} = 0.35, \delta = 40^\circ, \phi_{backfill} = 40^\circ$$

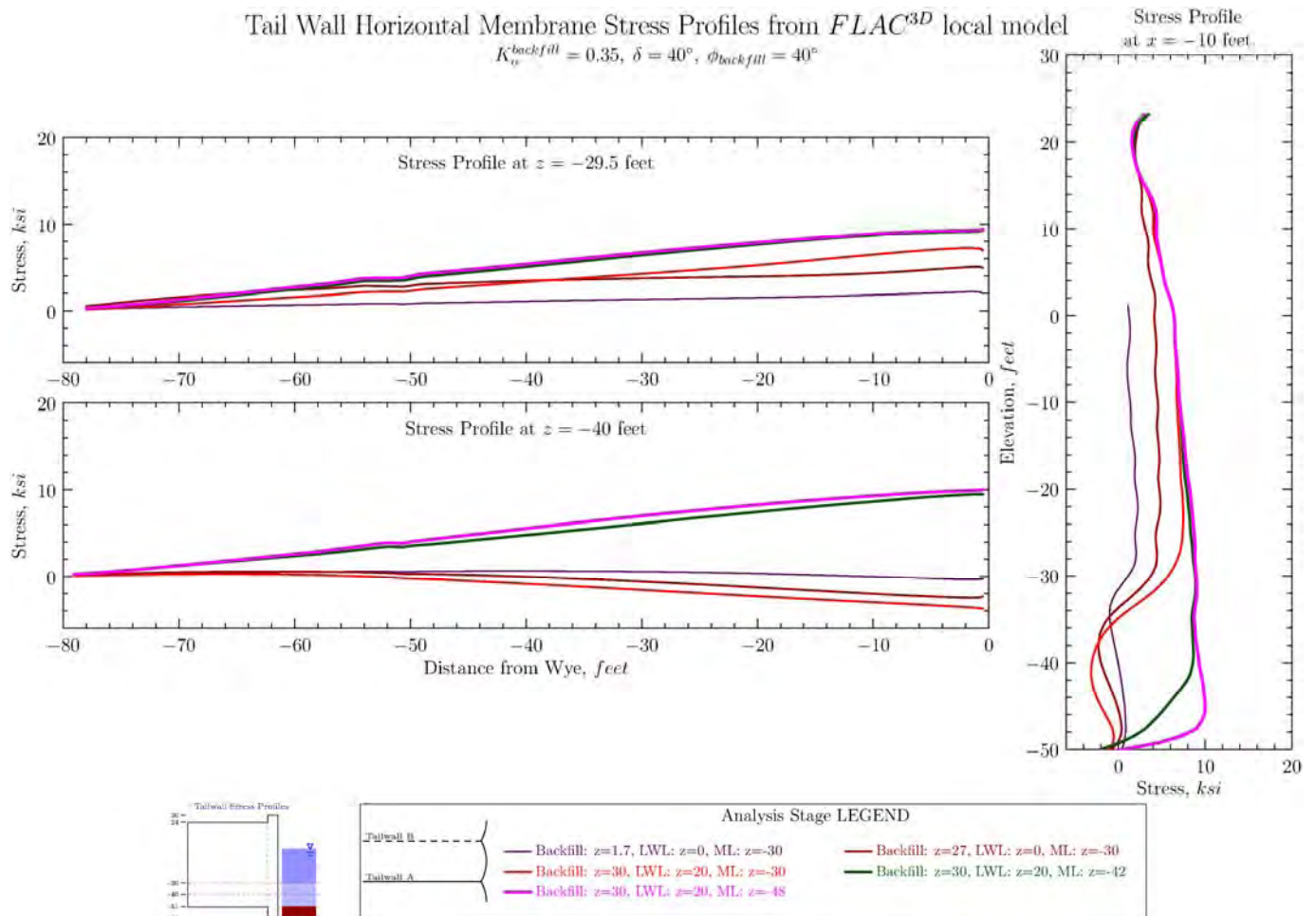


Figure G-1.20. Profiles of Tailwall Hoop Stresses for  $\delta=\phi=40^\circ$  with  $K_q=0.35$  for Fill Layer Parametric Case

Tail Wall Horizontal Membrane Stress Profiles from *FLAC<sup>3D</sup>* local model  
no slide wye

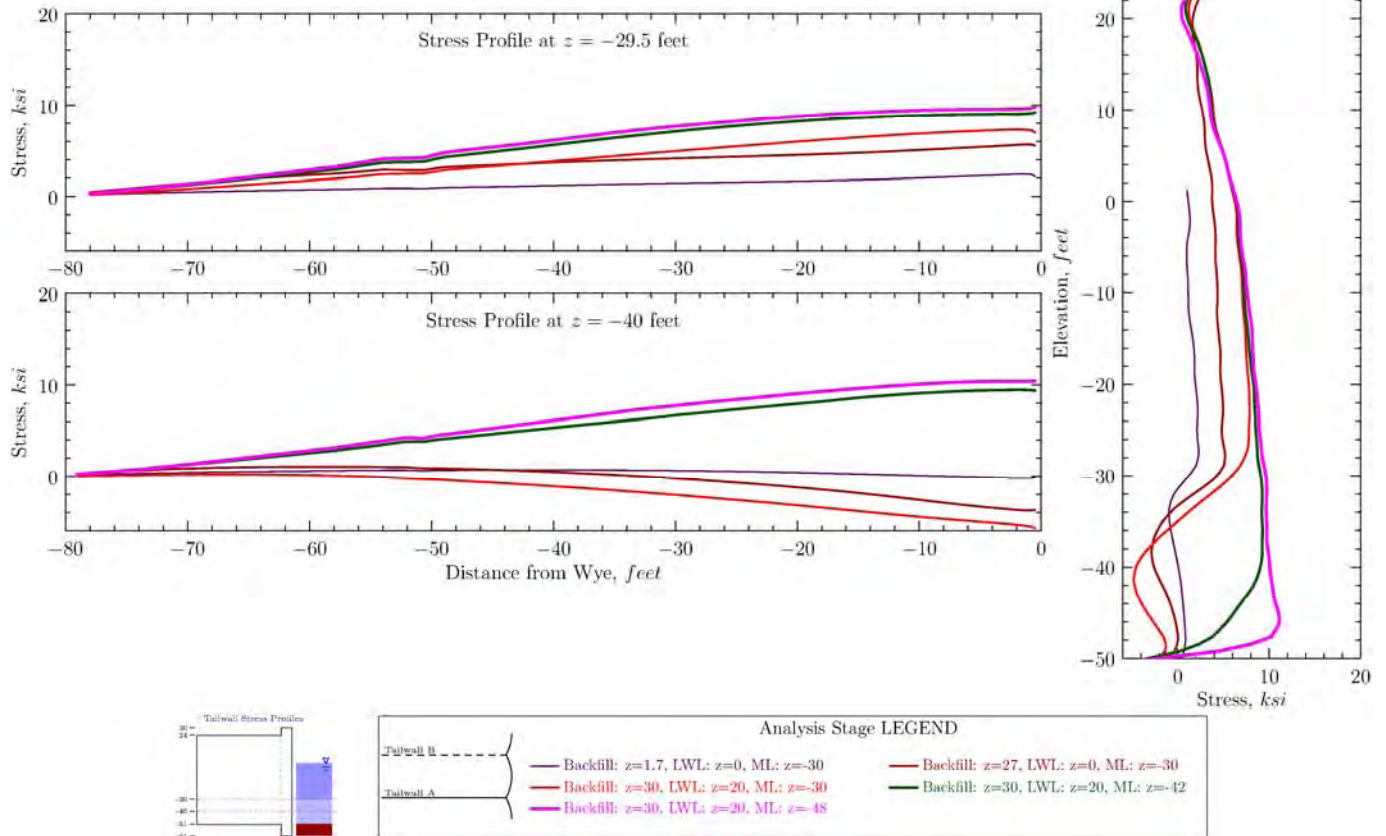


Figure G-1.21. Profiles of Tailwall Hoop Stresses for Fixed Wye Connector Parametric Case

Tail Wall Horizontal Membrane Stress Profiles from *FLAC<sup>3D</sup>* local model

$$K_o^{backfill} = 0.5, \delta = 40^\circ, \phi_{backfill} = 40^\circ$$

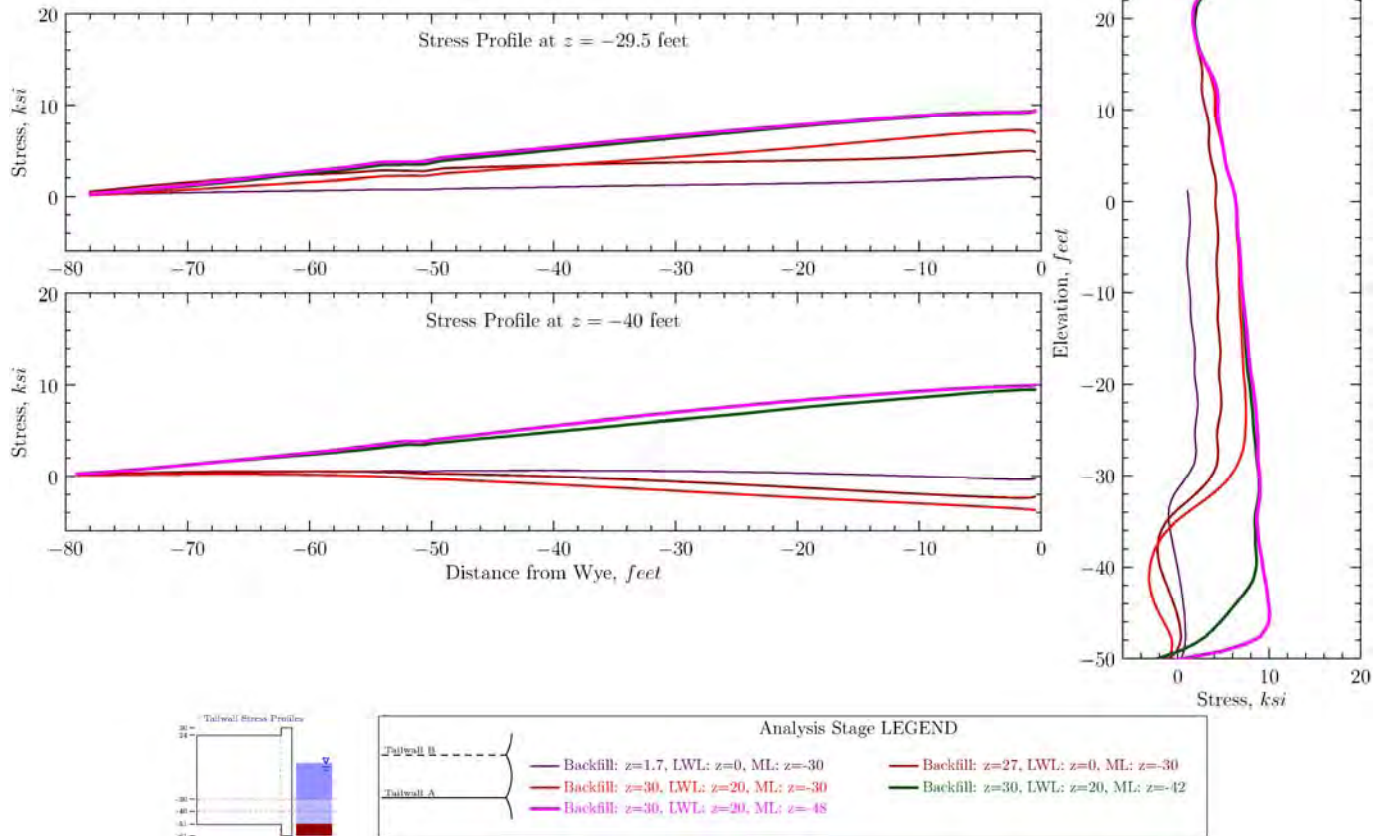


Figure G-1.22. Profiles of Tailwall Hoop Stresses for  $\delta=\phi=40^\circ$  Parametric Case

Tail Wall Horizontal Membrane Stress Profiles from *FLAC<sup>3D</sup>* local model

$$c_{33}^{tailwall} = 10 \times c_{33}^{base\ case}$$

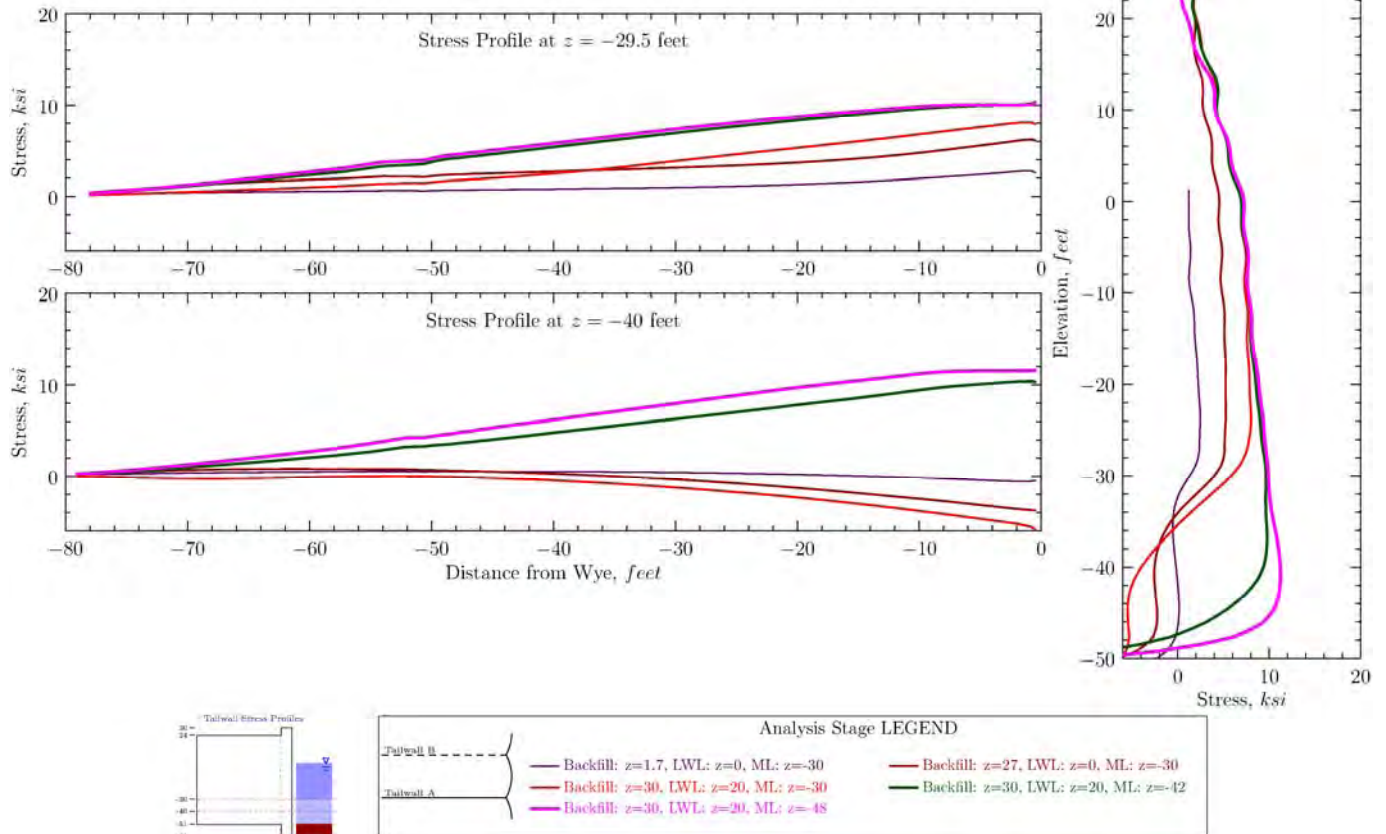


Figure G-1.23. Profiles of Tailwall Hoop Stresses for Increased Tailwall Shear Stiffness Parametric Case

Tail Wall Horizontal Membrane Stress Profiles from *FLAC*<sup>3D</sup> local model

$$\delta = 40^\circ, \phi_{backfill} = 40^\circ;$$

$$K_{backfill} = 1.67 \times K_{backfill}^{base\ case}$$

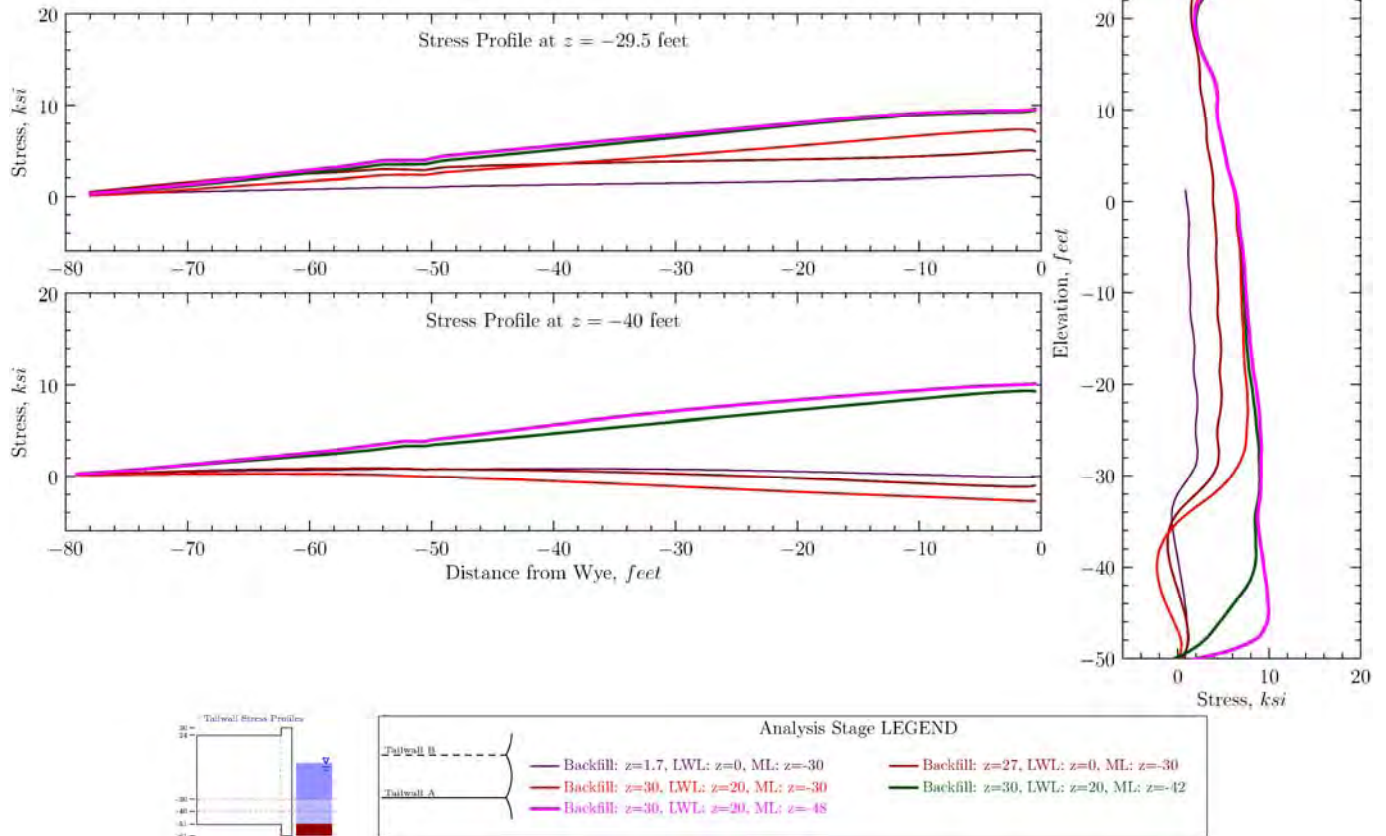


Figure G-1.24. Profiles of Tailwall Hoop Stresses For Increased Backfill Stiffness Number and  $\delta=\phi=40^\circ$  Parametric Case

Tail Wall Horizontal Membrane Stress Profiles from *FLAC<sup>3D</sup>* local model

$$k_{stailwall} = 10 \times k_{stailwall}^{base\ case}$$

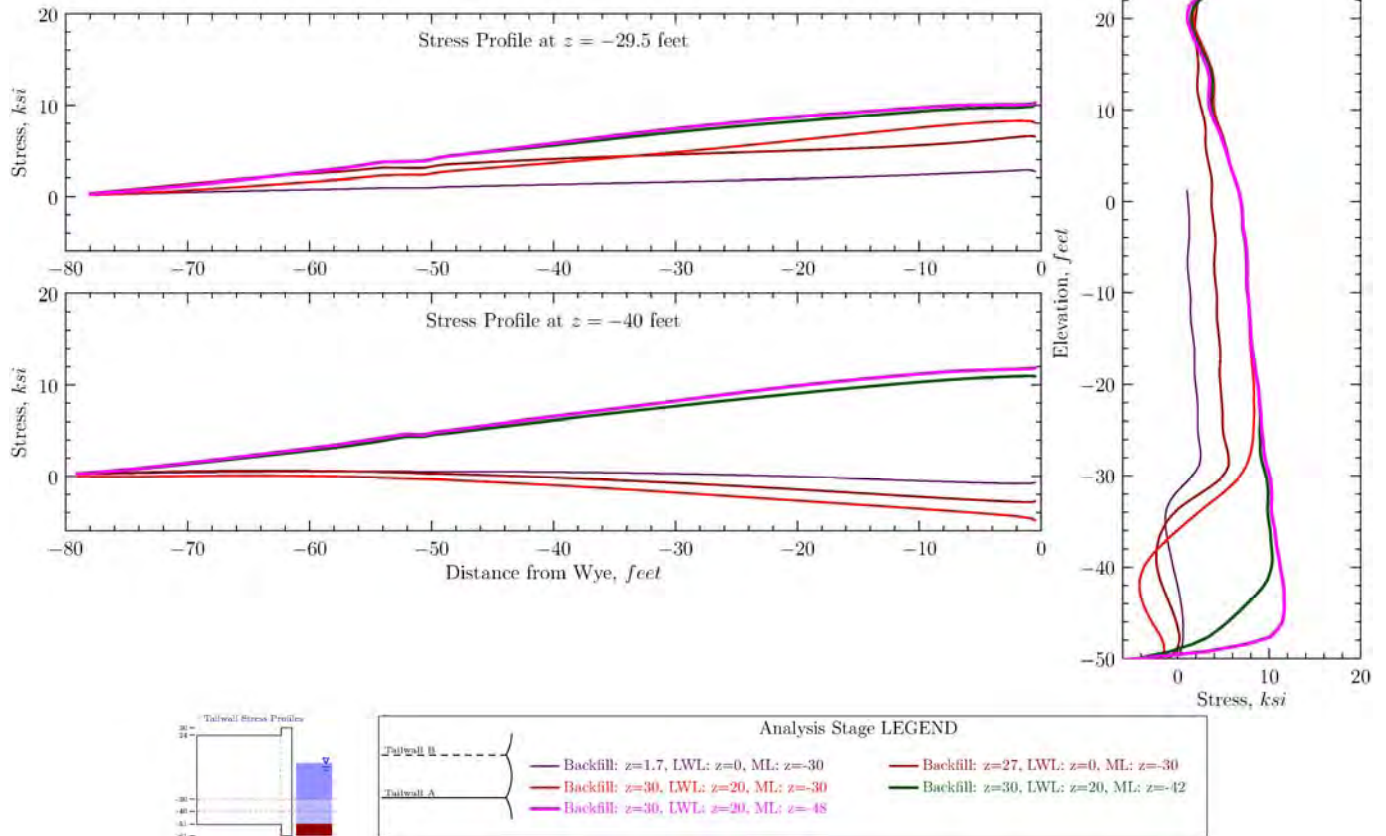


Figure G-1.25. Profiles of Tailwall Hoop Stresses for Increased Tailwall Shear Coupling Spring Stiffness Parametric Case

Tail Wall Horizontal Membrane Stress Profiles from *FLAC*<sup>3D</sup> local model

$$k_{stailwall} = 0.1 \times k_{stailwall}^{base\ case}$$

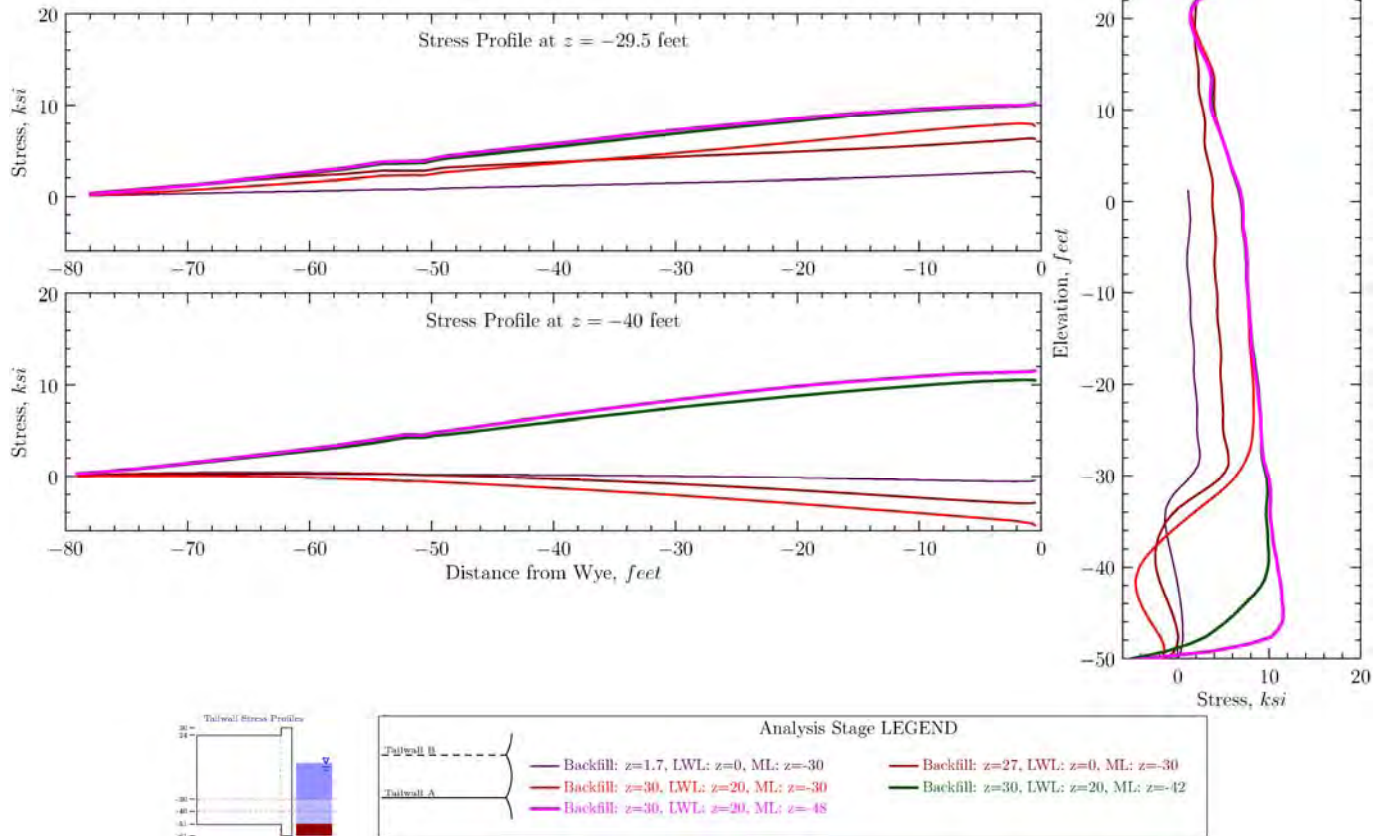


Figure G-1.26. Profiles of Tailwall Hoop Stresses for Reduced Tailwall Shear Coupling Spring Stiffness Parametric Case

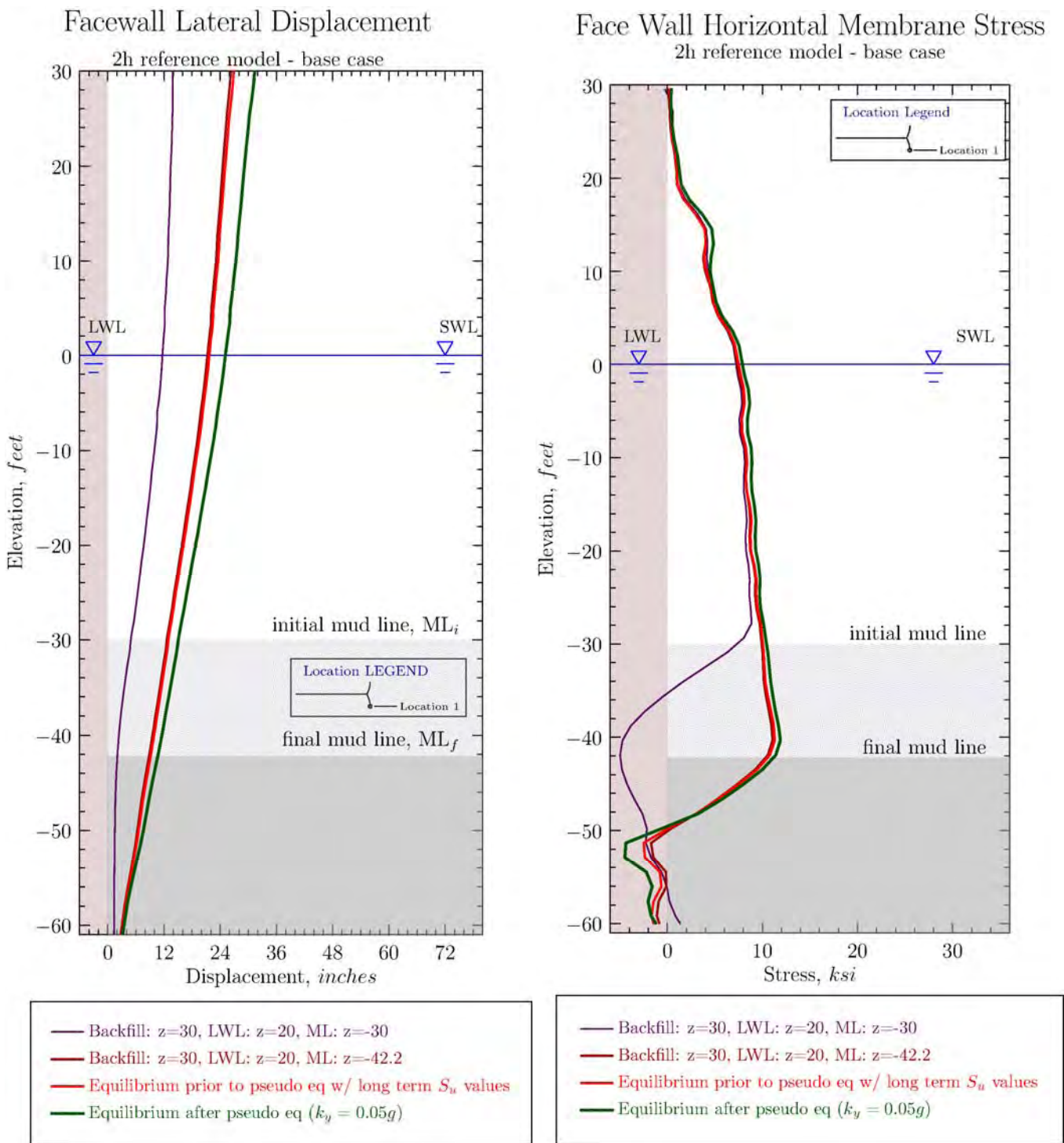


Figure G-1.27. Wall Displacements and Facewall Hoop Stresses for Pseudo-Static Earthquake Load, Base Case Model

Tail Wall Horizontal Membrane Stress Profiles from *FLAC*<sup>3D</sup> local model  
2h reference model, base case

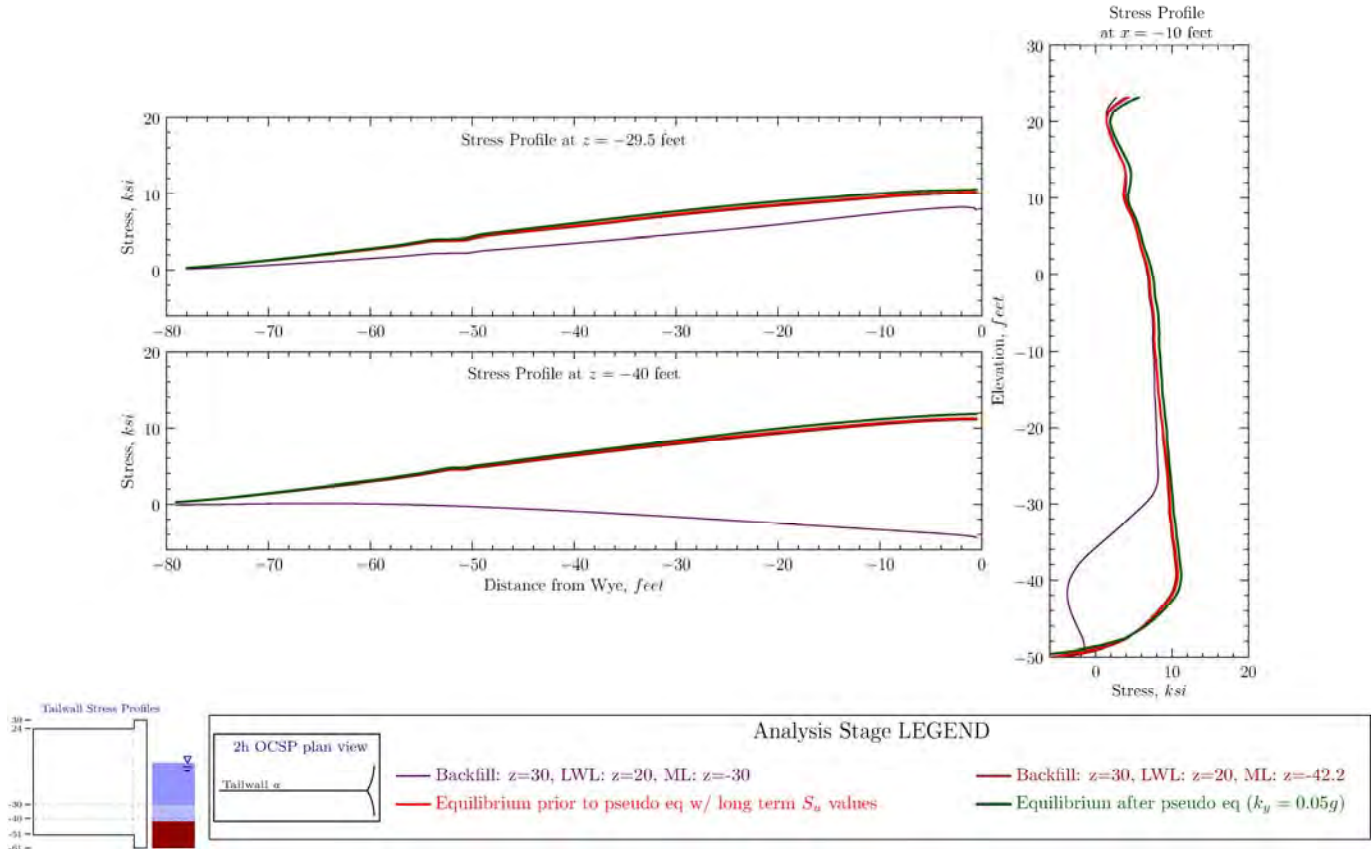


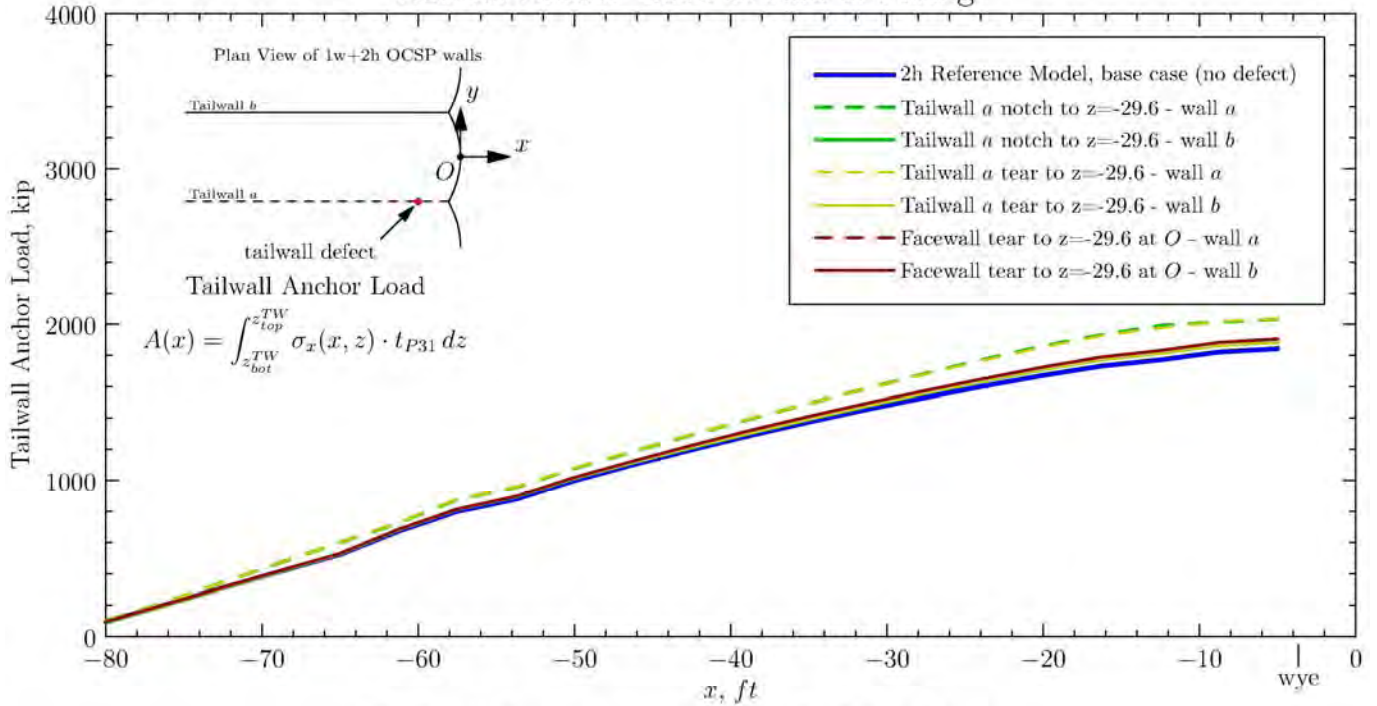
Figure G-1.28. Profiles of Tailwall Hoop Stresses for Pseudo-Static Earthquake Load, Base Case Model

**Attachment G-2**  
**Summary Figures for 1w + 2h Models**



## Defect Model Comparison

### Tailwall Anchor Load at End of Filling



### Tailwall Anchor Load at End of Dredging

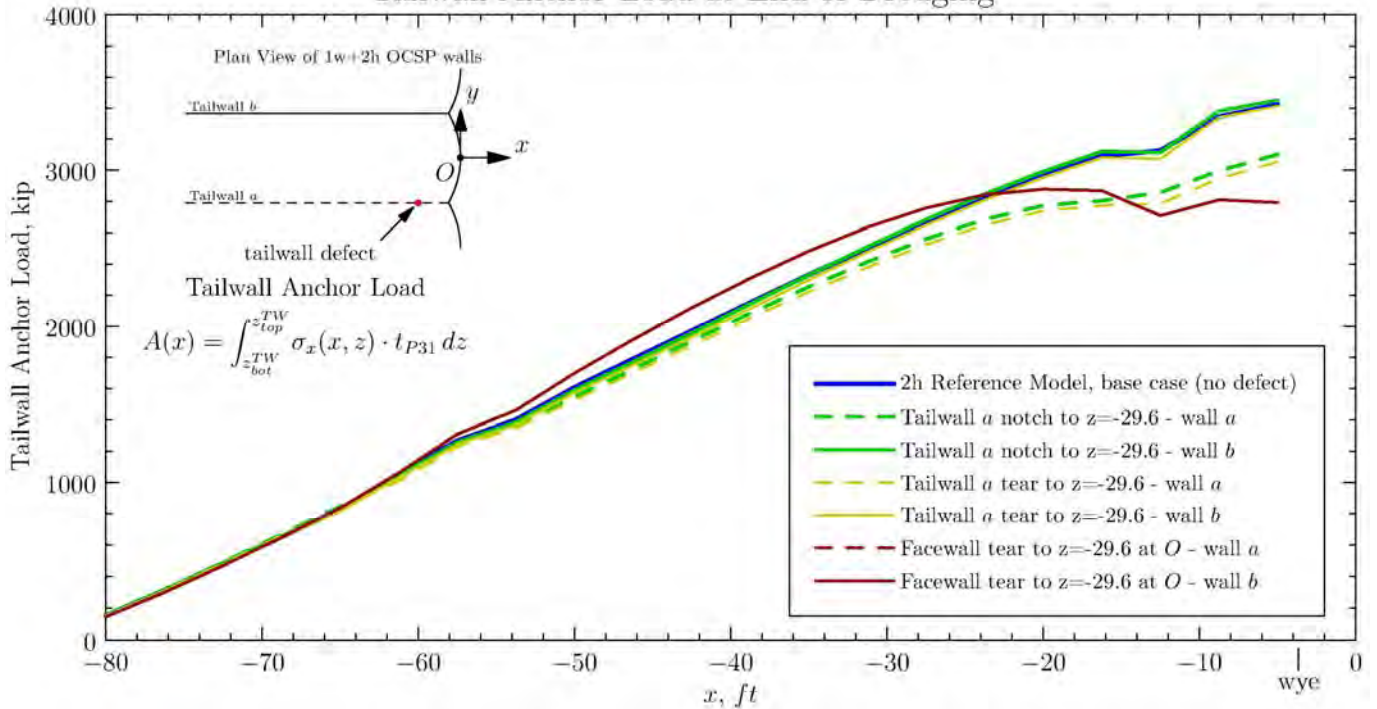
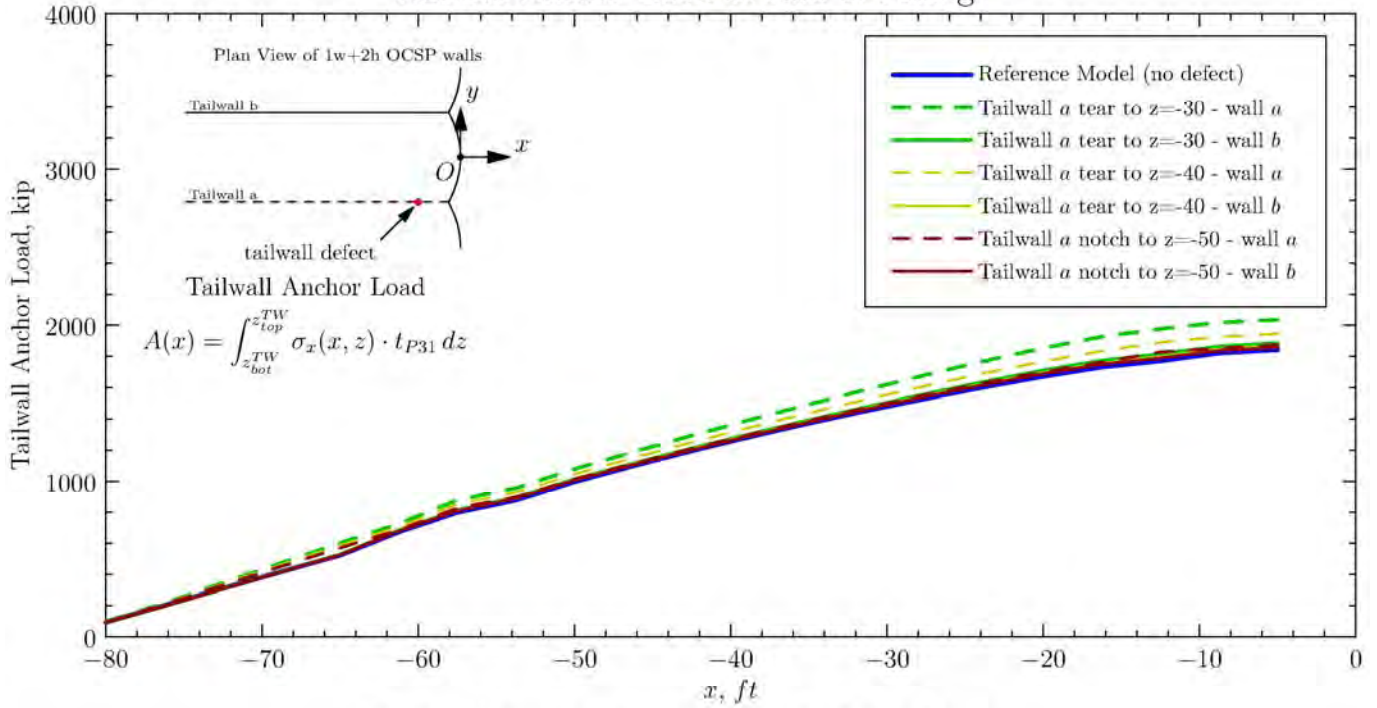


Figure G-2.1. Tailwall Anchor Loads from 1w+2h Defect Models

## Tailwall Defect Model Comparison

### Tailwall Anchor Load at End of Filling



### Tailwall Anchor Load at End of Dredging

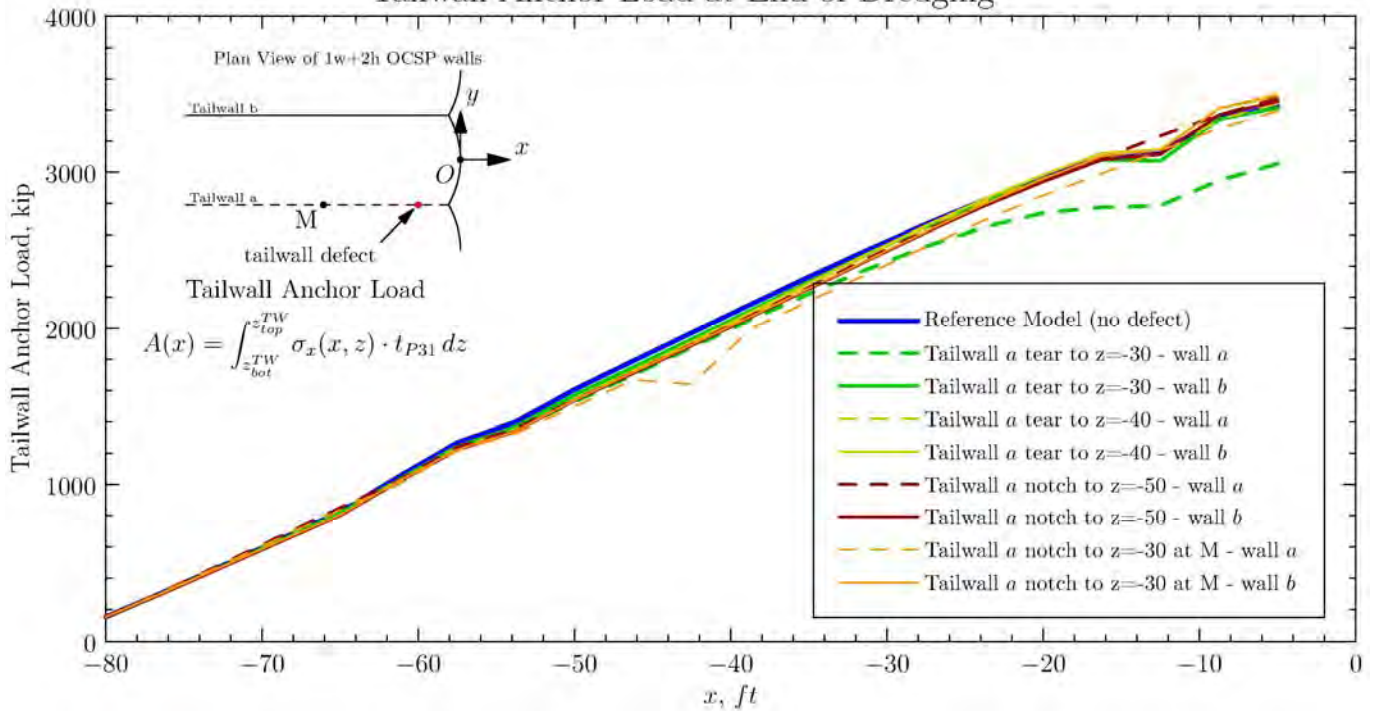


Figure G-2.2. Tailwall Anchor Loads for Tailwall Defect Models

# Facewall Lateral Displacement

## 1w+2h Defect Models

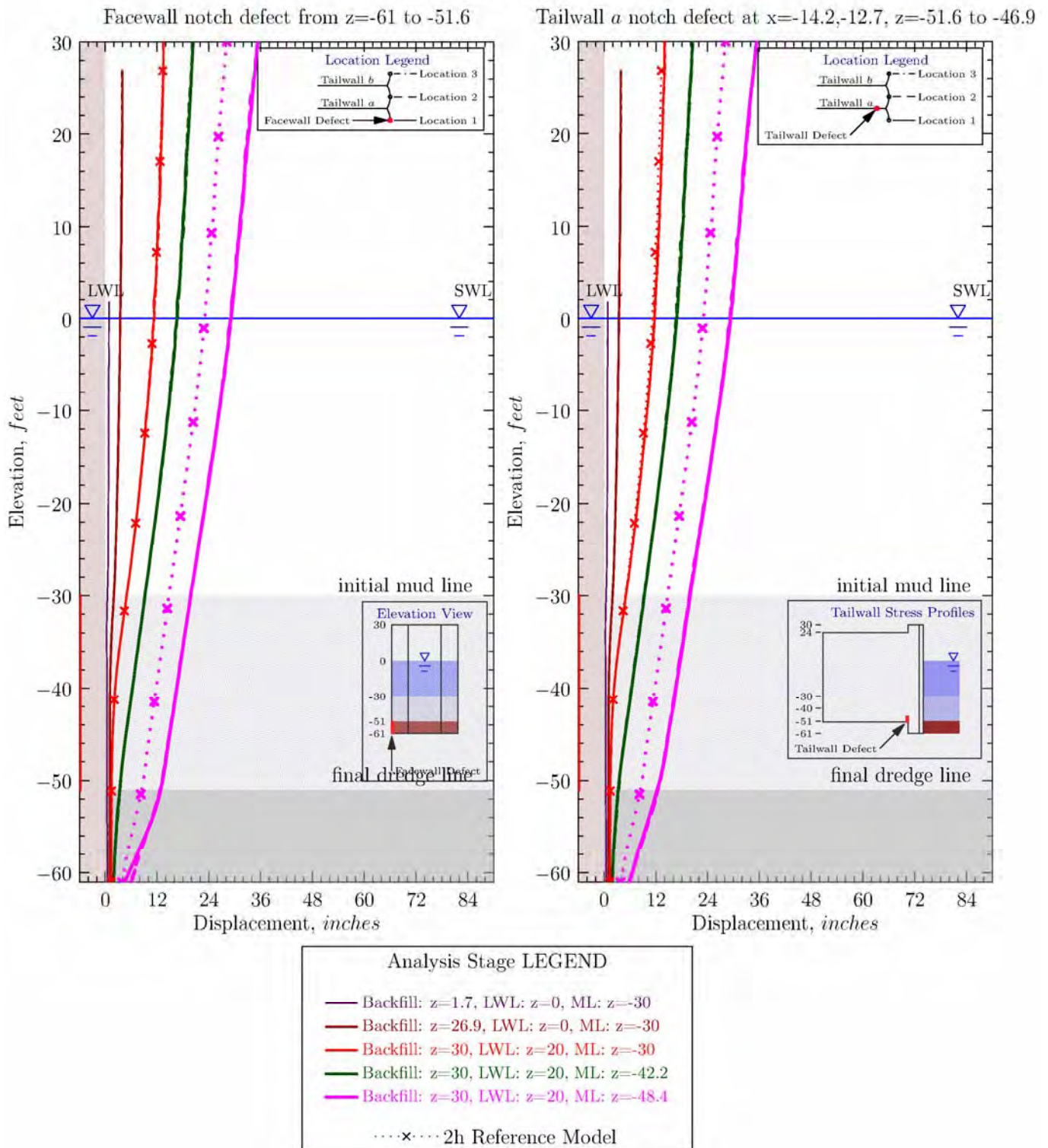


Figure G-2.3. Facewall Lateral Displacements from Short Facewall and Tailwall Defect Models

## Facewall Lateral Displacement 1w+2h Defect Models

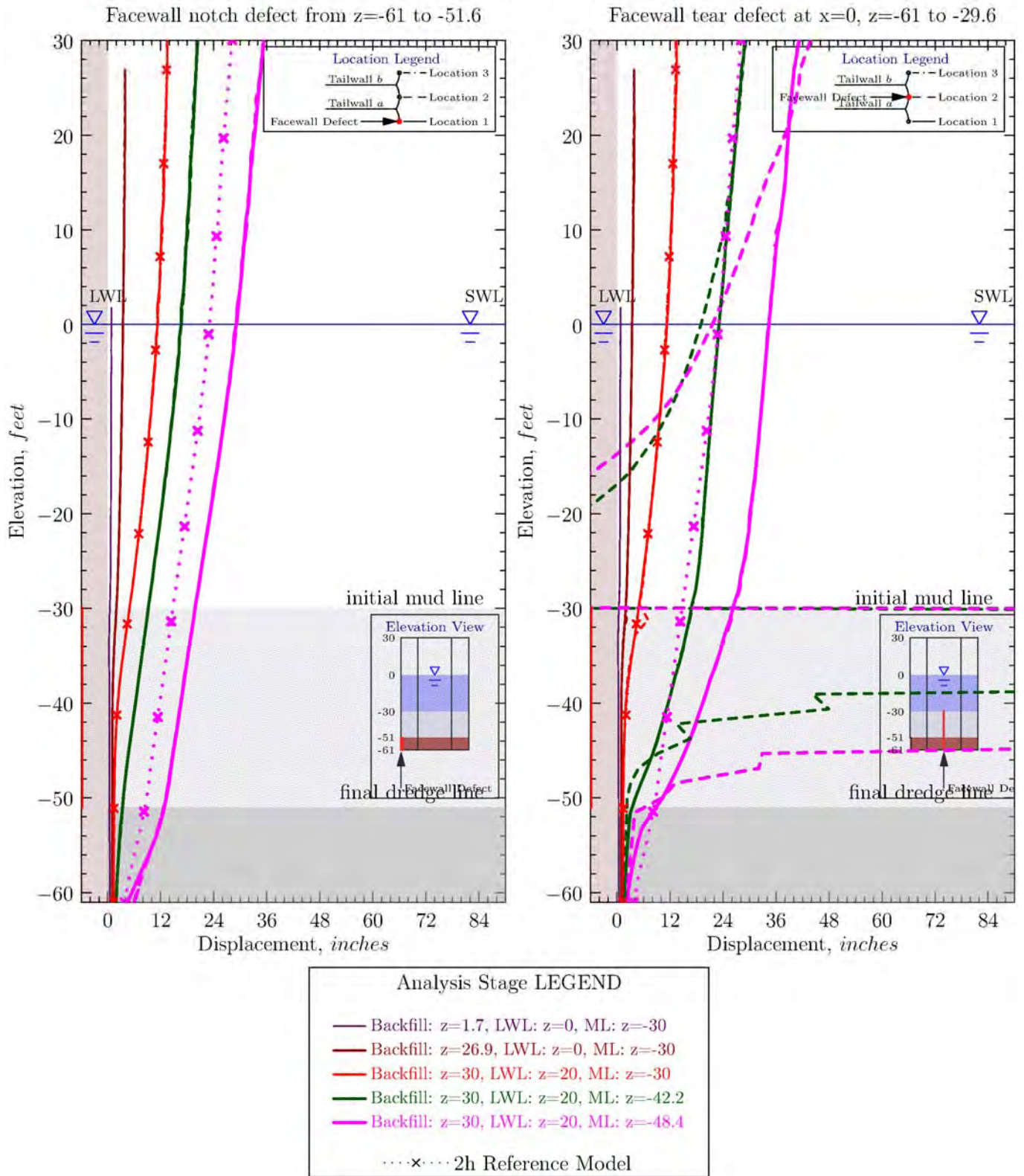


Figure G-2.4. Facewall Lateral Displacements from Short and Long Facewall Defect Models

# Facewall Lateral Displacement

## 1w+2h Defect Models

Tailwall *a* notch defect at  $x=-14.2, -12.7, z=-51.6$  to  $-46.9$

Tailwall *a* notch defect at  $x=-14.2, -12.7, z=-51.6$  to  $-29.6$

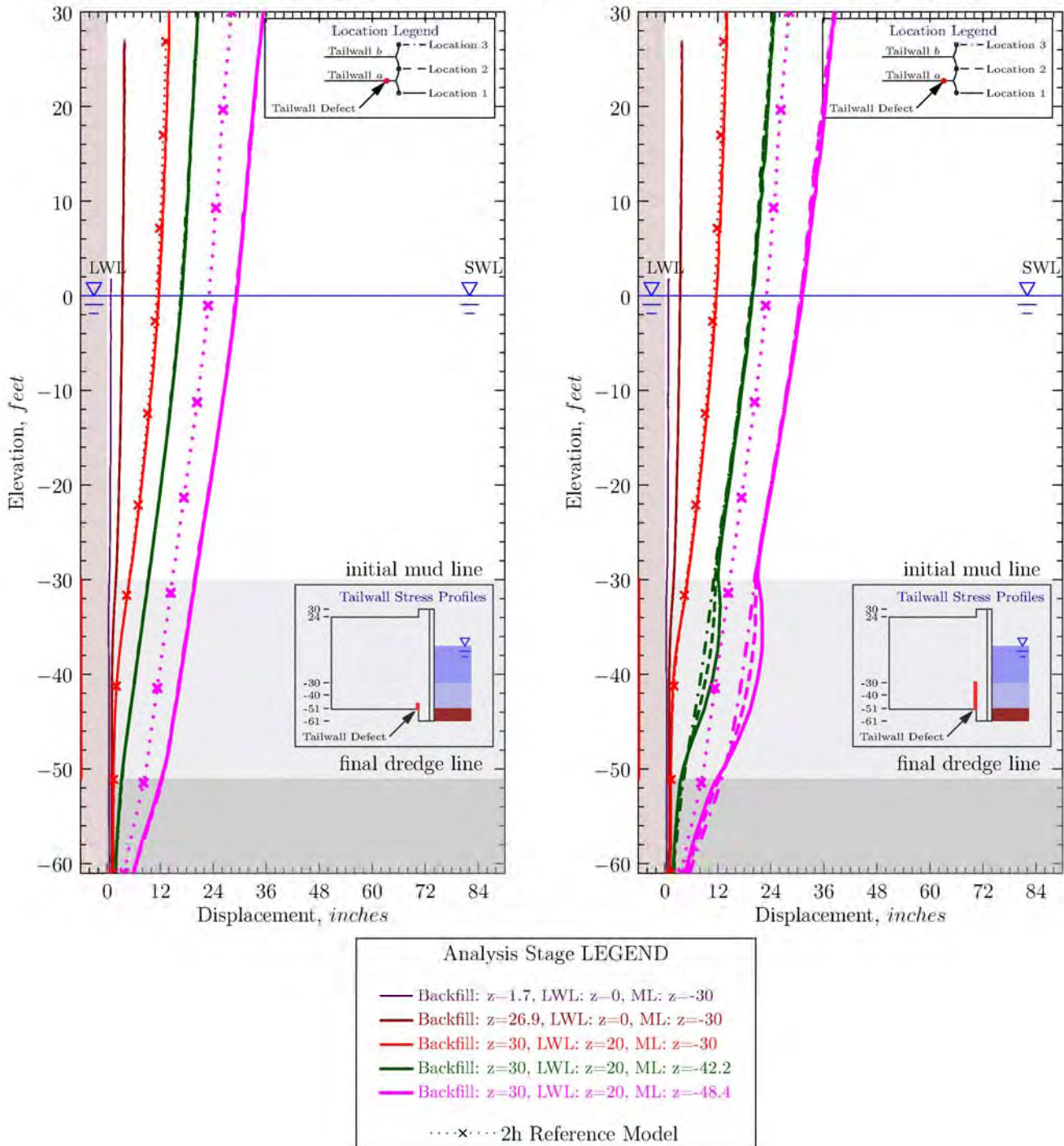


Figure G-2.5. Facewall Lateral Displacements from Short and Long Tailwall Defect Models

# Facewall Lateral Displacement

## 1w+2h Defect Models

Tailwall *a* notch defect at  $x=-14.2, -12.7$   $z=-51.6$  to  $-29.6$

Tailwall *a* tear defect at  $x=-12.7, z=-51.6$  to  $-29.6$

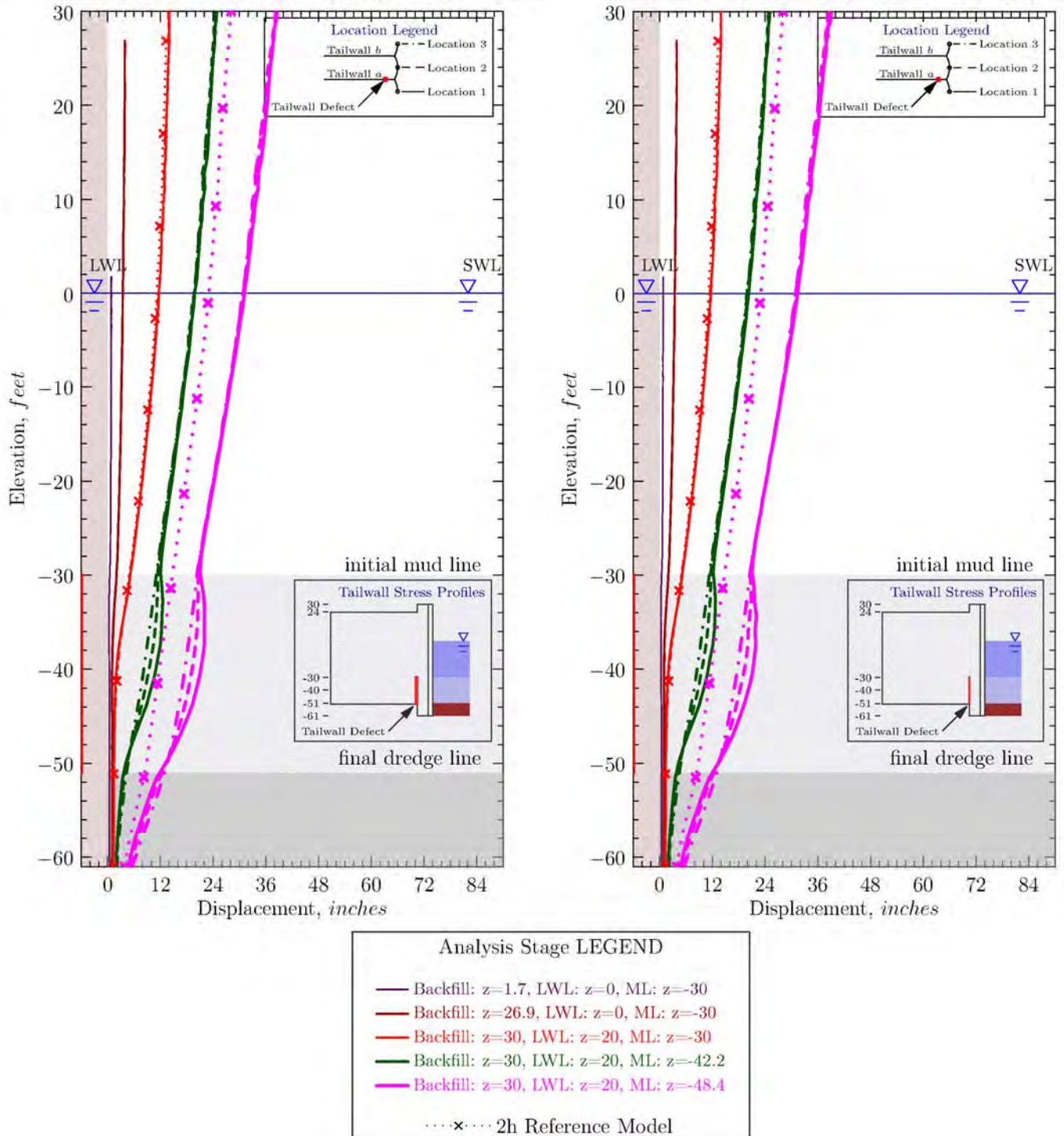
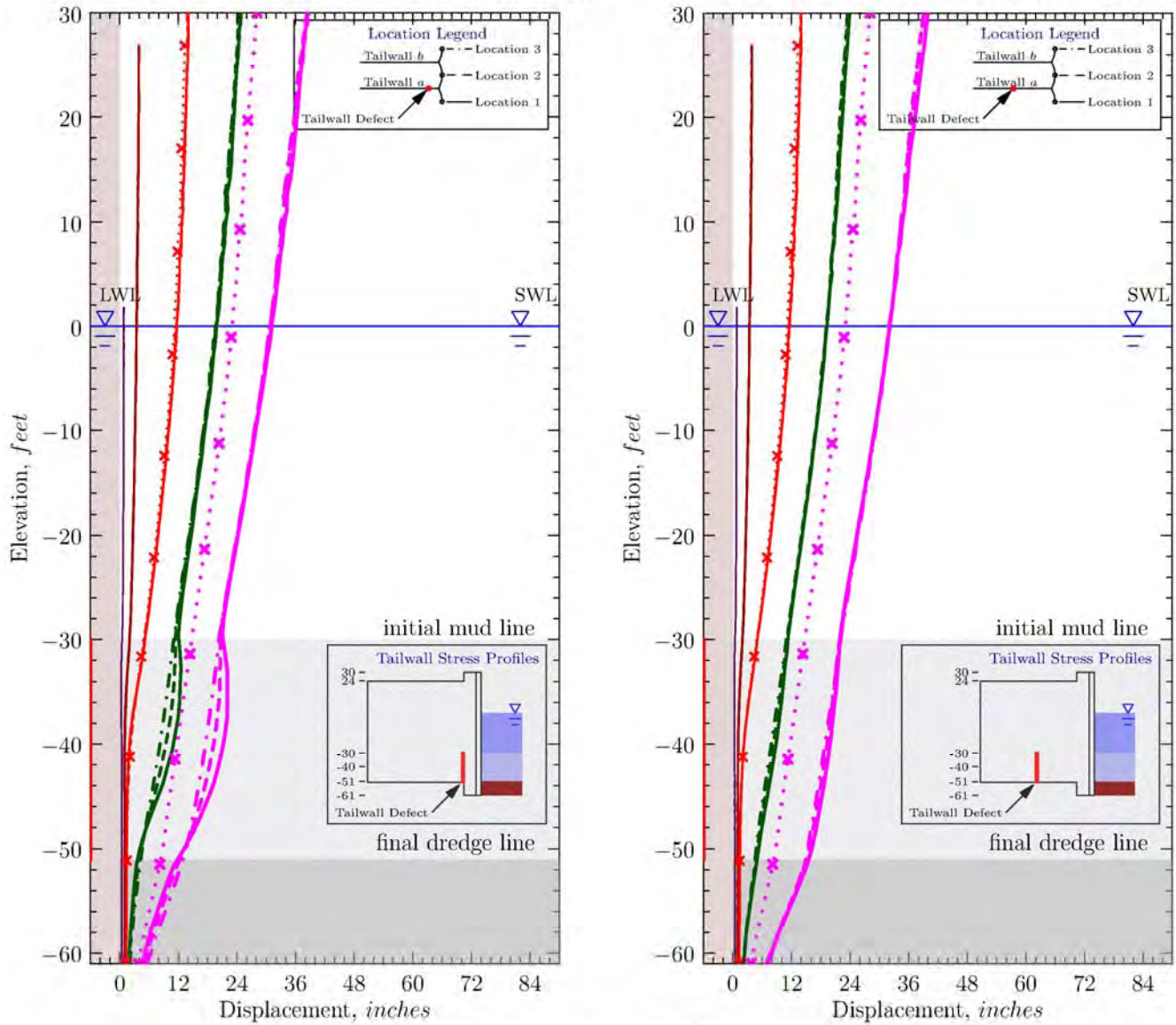


Figure G-2.6. Facewall Lateral Displacements from Long Tailwall Notch and Tear Defect Models

## Facewall Lateral Displacement 1w+2h Defect Models

Tailwall *a* notch defect at  $x=-14.2, -12.7$   $z=-51.6$  to  $-29.6$

Tailwall *a* notch defect at  $x=-42.9, -41.4$   $z=-51.6, -29.6$



Analysis Stage LEGEND	
—	Backfill: $z=1.7$ , LWL: $z=0$ , ML: $z=-30$
—	Backfill: $z=26.9$ , LWL: $z=0$ , ML: $z=-30$
—	Backfill: $z=30$ , LWL: $z=20$ , ML: $z=-30$
—	Backfill: $z=30$ , LWL: $z=20$ , ML: $z=-42.2$
—	Backfill: $z=30$ , LWL: $z=20$ , ML: $z=-48.4$
··· × ···	2h Reference Model

Figure G-2.7. Facewall Lateral Displacements from Long Tailwall Defects Near and Far From Wye Models

## Facewall Lateral Displacement 1w+2h Defect Models

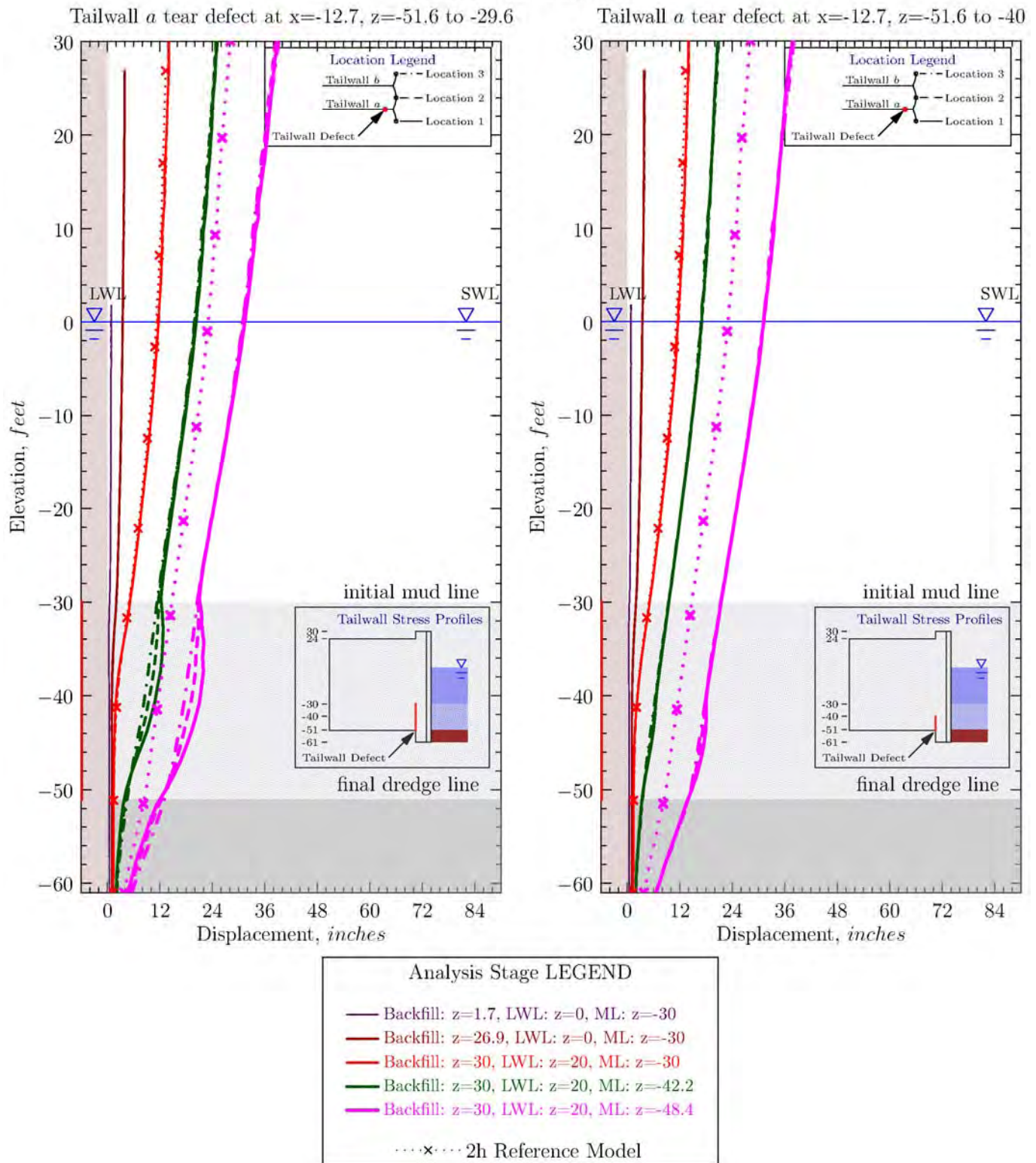


Figure G-2.8. Facewall Lateral Displacements from Short and Intermediate Tailwall Tear Defect Models

## Face Wall Horizontal Membrane Stress 1w+2h Defect Models

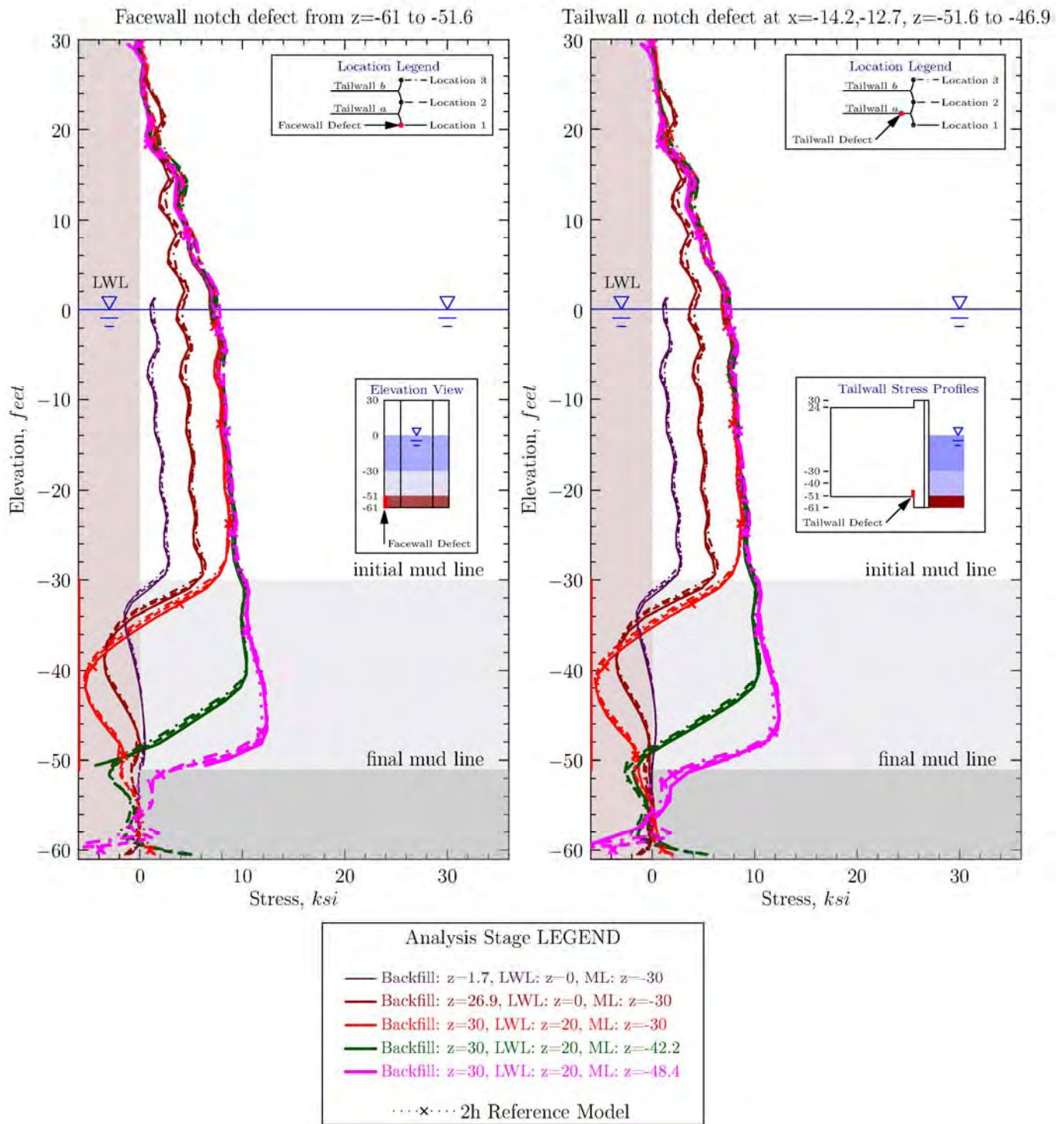


Figure G-2.9. Facewall Hoop Stresses from Short Facewall and Tailwall Defect Models

## Face Wall Horizontal Membrane Stress 1w+2h Defect Models

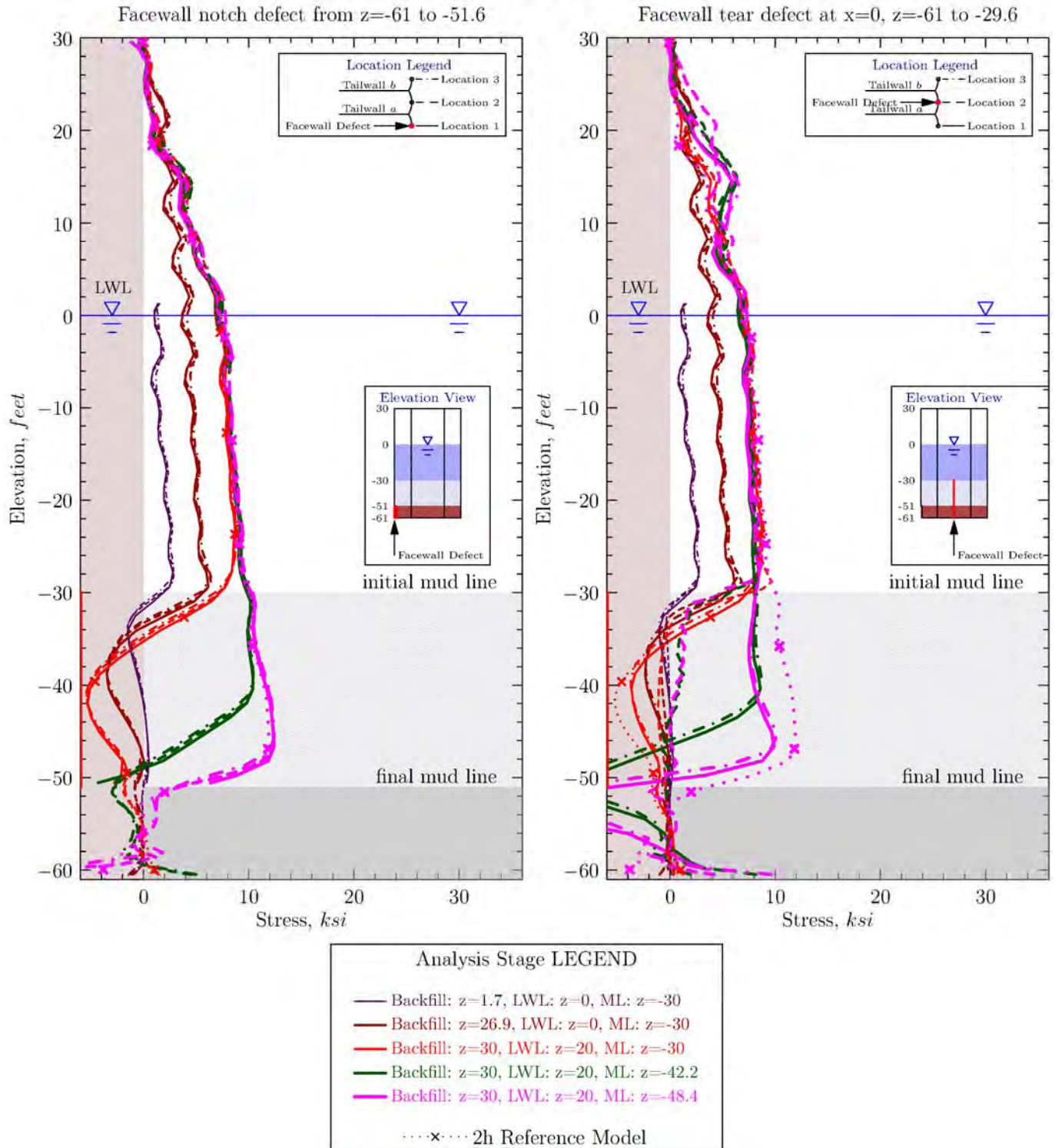


Figure G-2.10. Facewall Hoop Stresses from Short and Long Facewall Defect Models

### Face Wall Horizontal Membrane Stress 1w+2h Defect Models

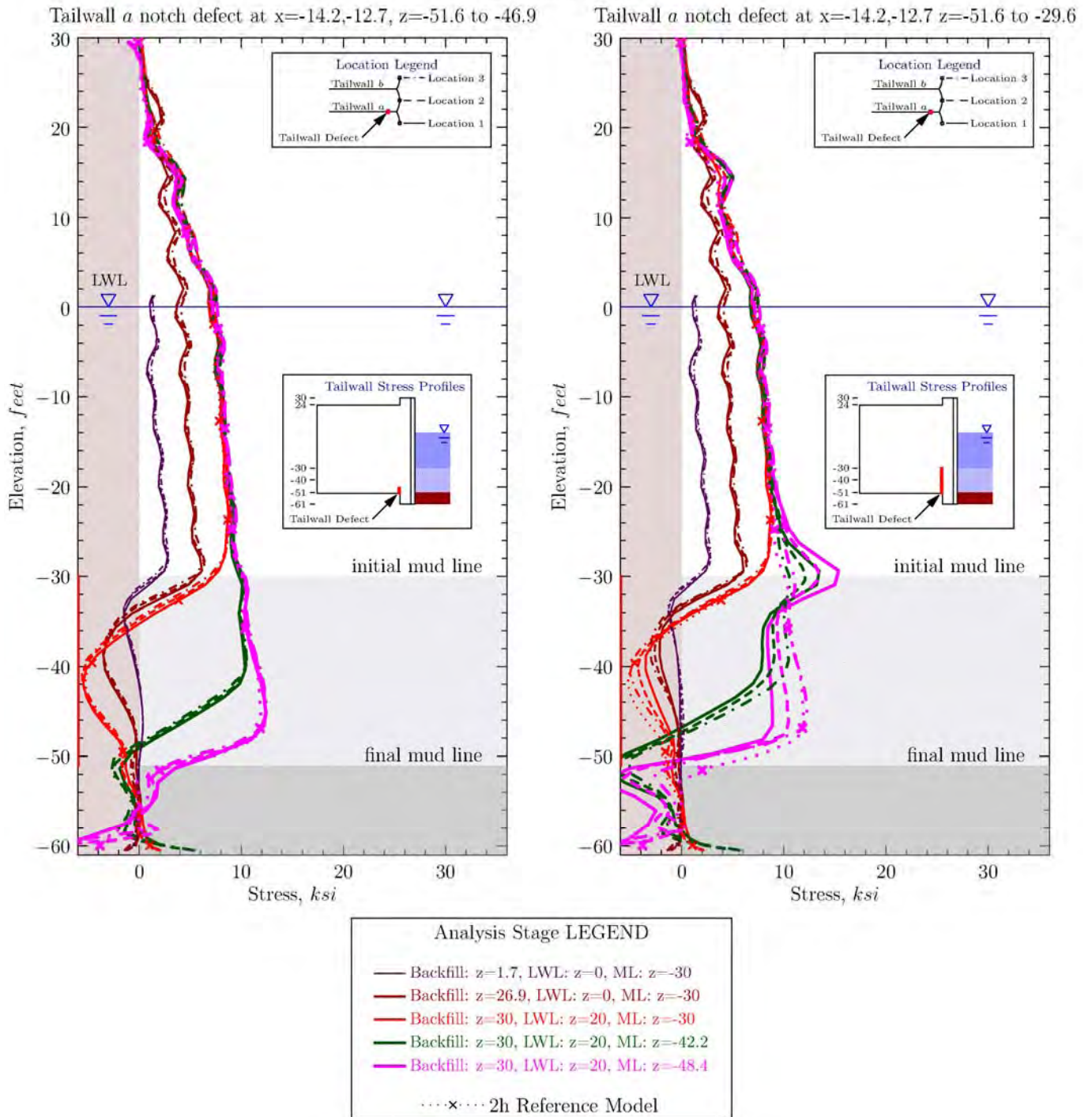


Figure G-2.11. Facewall Hoop Stresses from Short and Long Tailwall Notch Defect Models

## Face Wall Horizontal Membrane Stress 1w+2h Defect Models

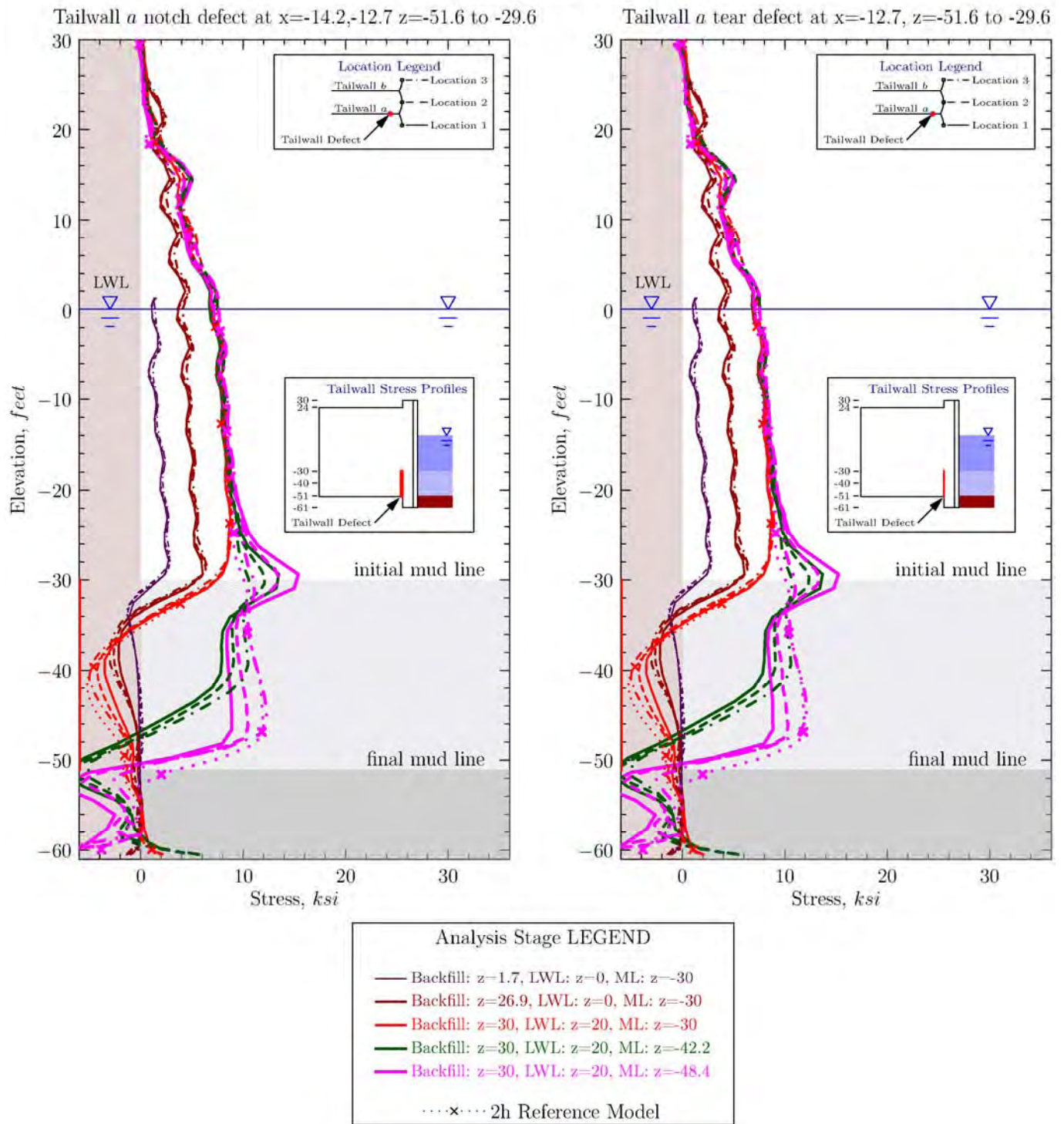


Figure G-2.12. Facewall Hoop Stresses from Long Tailwall Tear Defect Models

### Face Wall Horizontal Membrane Stress 1w+2h Defect Models

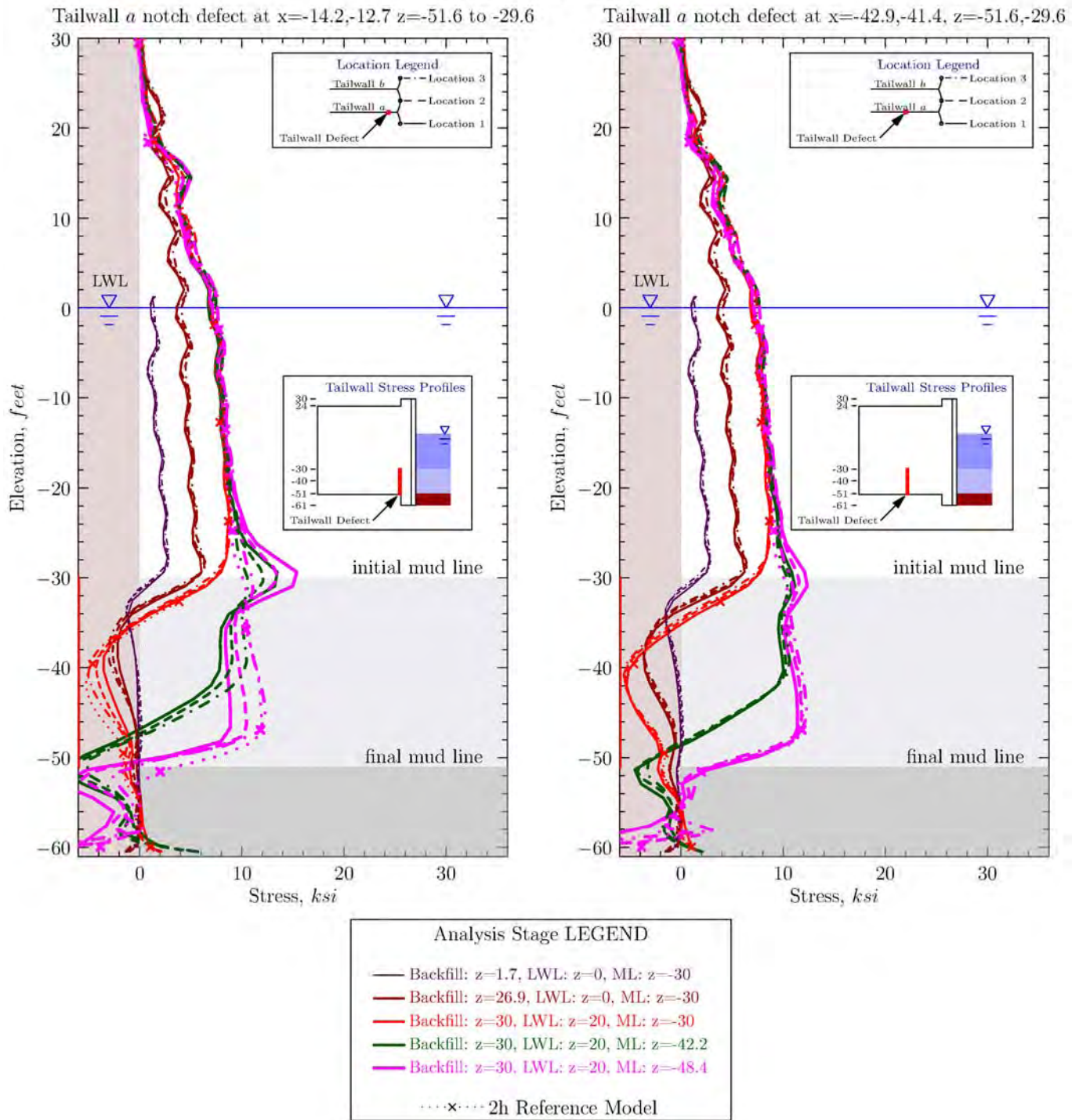


Figure G-2.13. Facewall Hoop Stresses from Long Tailwall Defects Near and Far From Wye Models

## Face Wall Horizontal Membrane Stress 1w+2h Defect Models

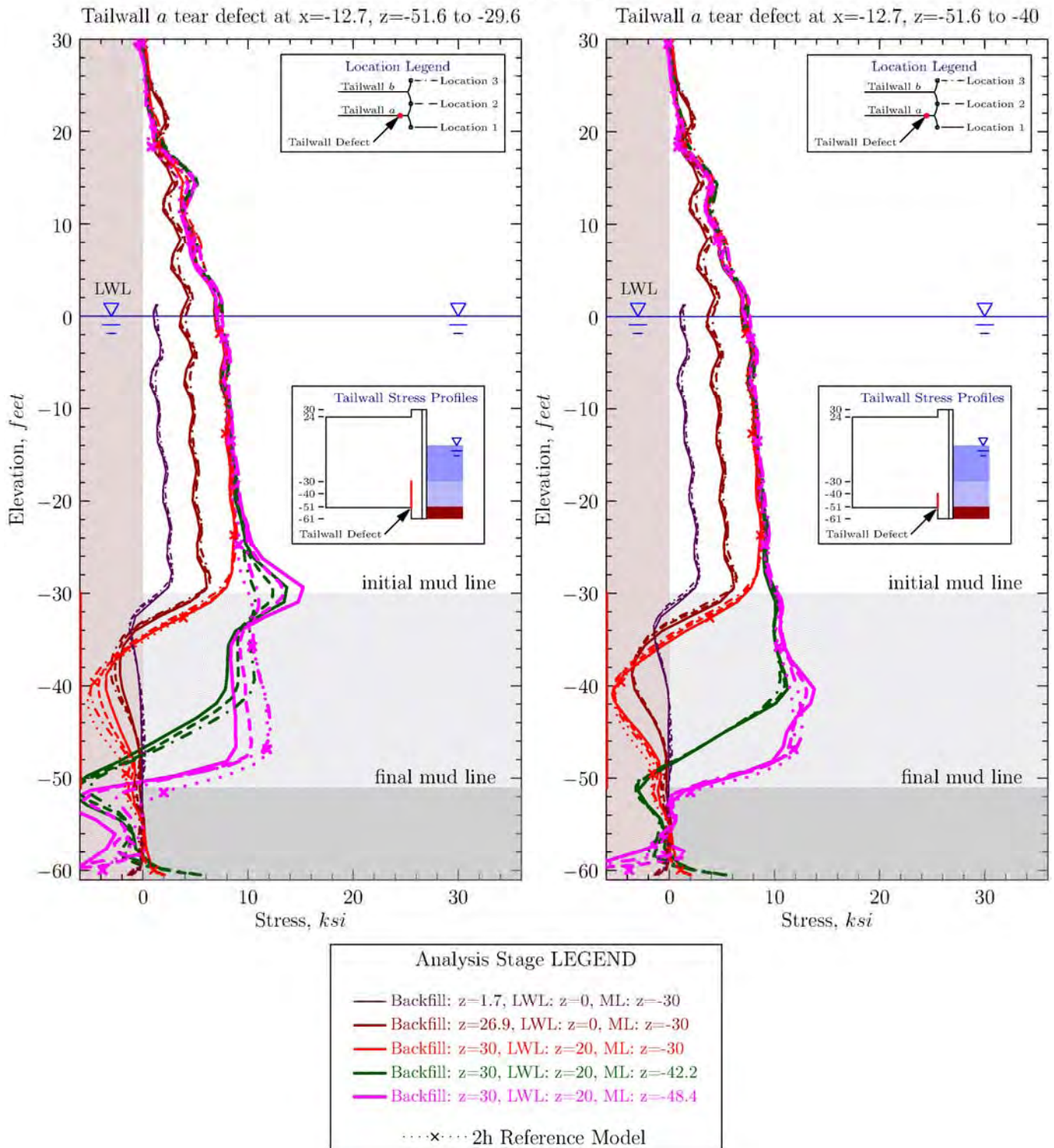


Figure G-2.14. Facewall Hoop Stresses from Long and Intermediate Tailwall Tear Defect Models

Tail Wall Horizontal Membrane Stress Profiles from *FLAC*<sup>3D</sup> local model  
 1w+2h defect model - Facewall notch defect from z=-61 to -51.6

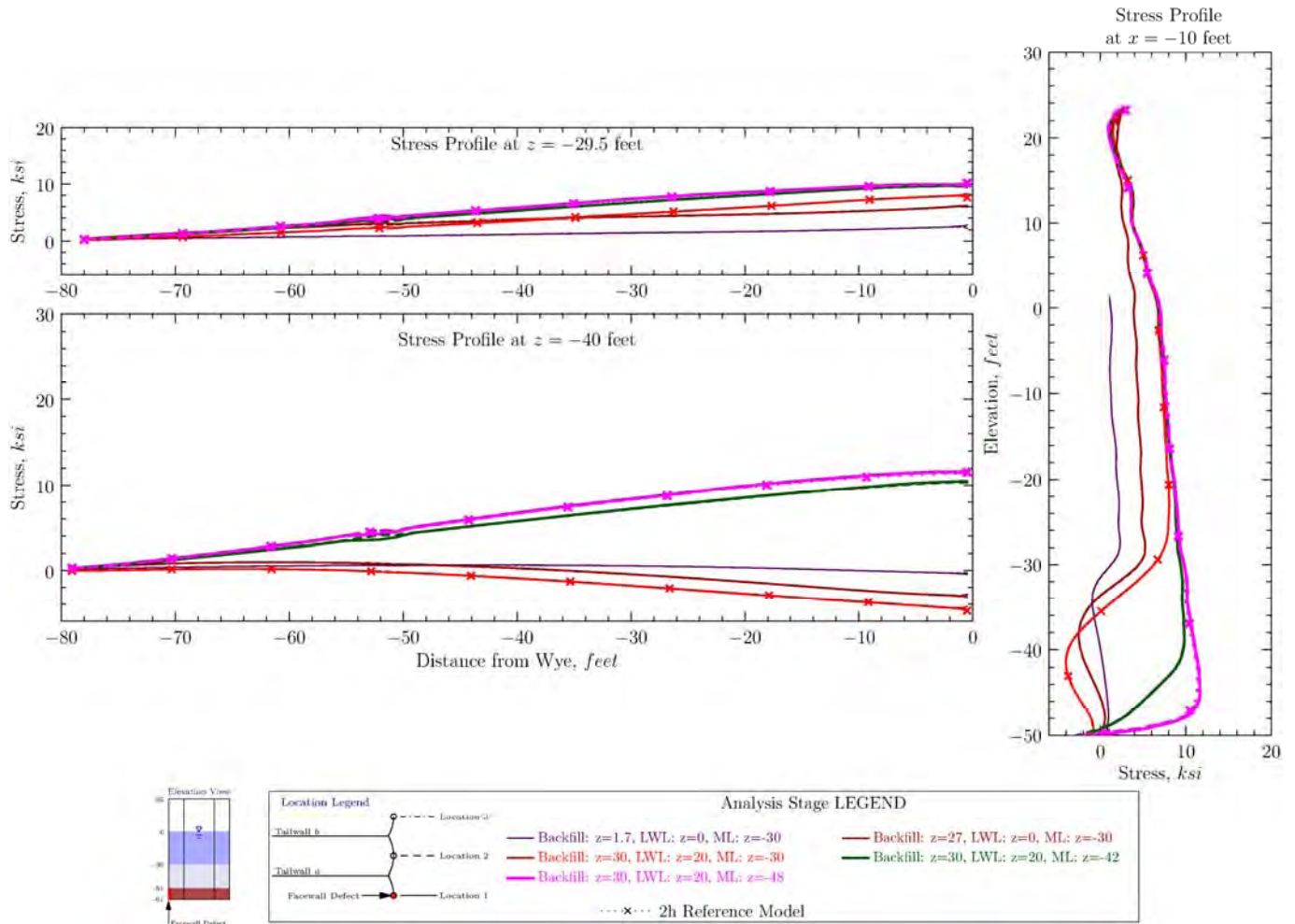


Figure G-2.15. Tailwall Horizontal (Hoop) Stresses from Short Facewall Defect Model

Tail Wall Horizontal Membrane Stress Profiles from *FLAC*<sup>3D</sup> local model  
 1w+2h defect model - Tailwall *a* notch defect at x=-14.2,-12.7, z=-51.6 to -46.9

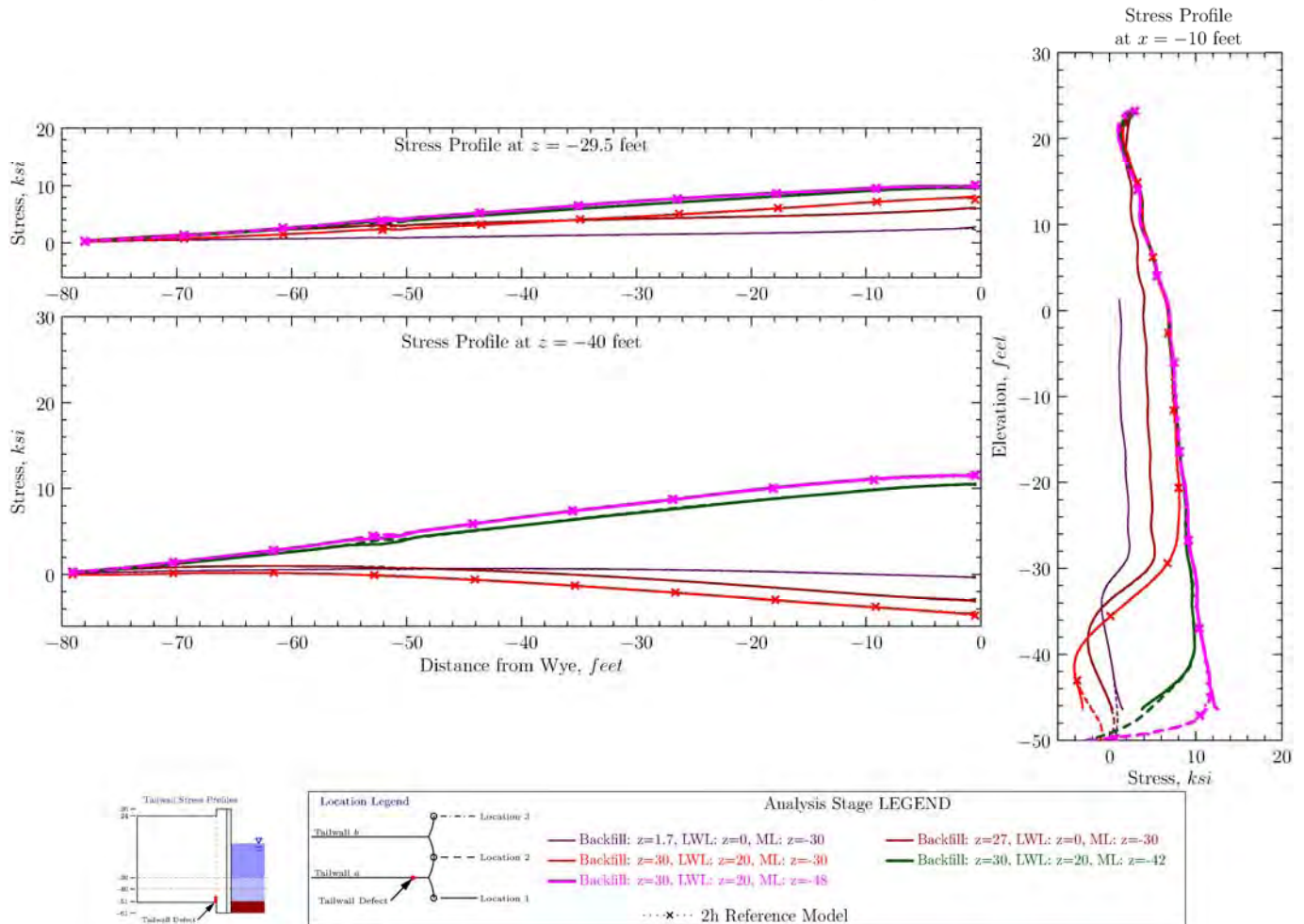


Figure G-2.16. Tailwall Horizontal (Hoop) Stresses from Short Tailwall Notch Defect Model

Tail Wall Horizontal Membrane Stress Profiles from *FLAC*<sup>3D</sup> local model  
 1w+2h defect model - Tailwall *a* notch defect at x=-14.2,-12.7 z=-51.6 to -29.6

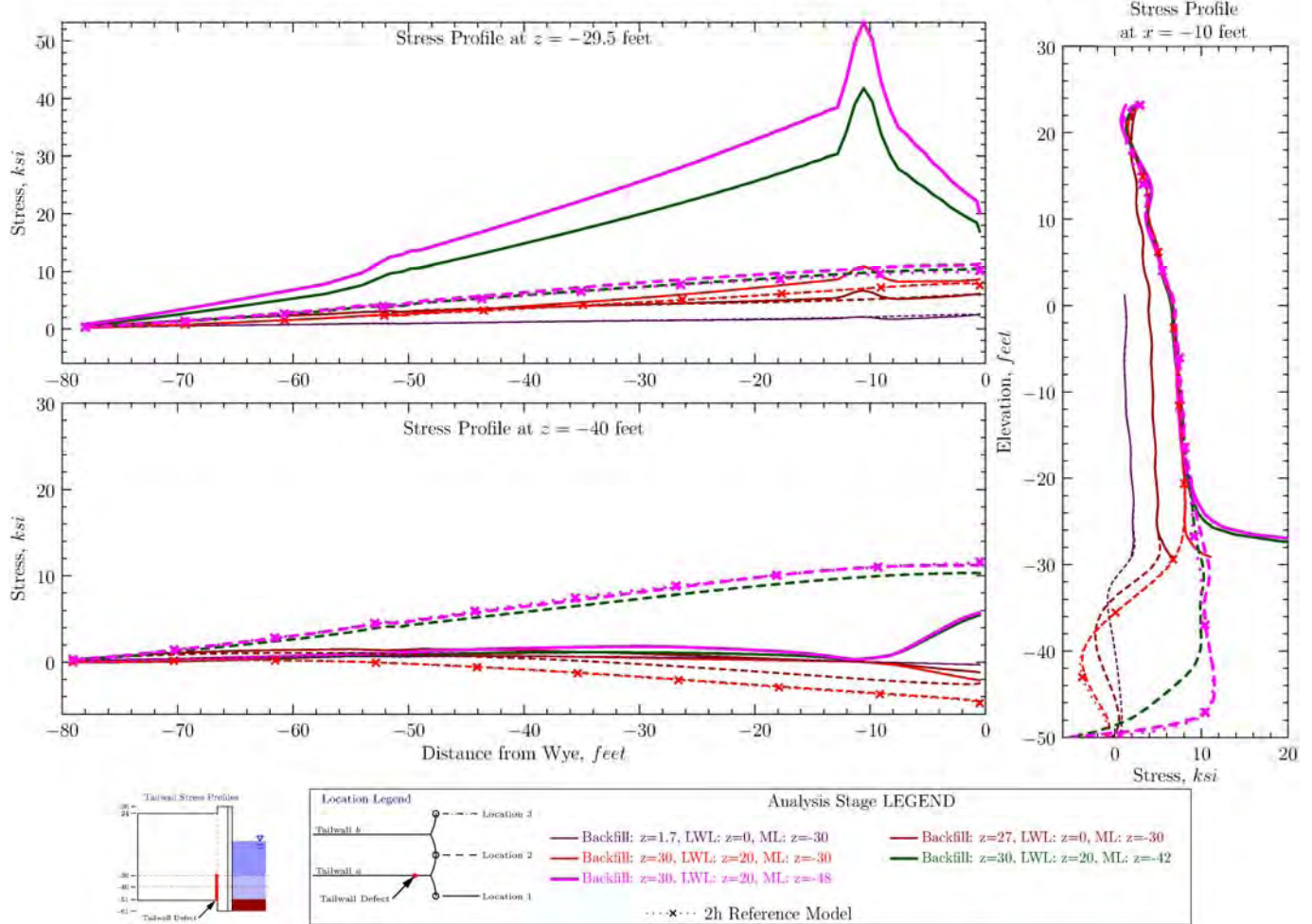


Figure G-2.17. Tailwall Horizontal (Hoop) Stresses from Long Tailwall Defect Model

Tail Wall Horizontal Membrane Stress Profiles from *FLAC*<sup>3D</sup> local model  
 1w+2h defect model - Tailwall *a* tear defect at  $x=-12.7, z=-51.6$  to  $-29.6$

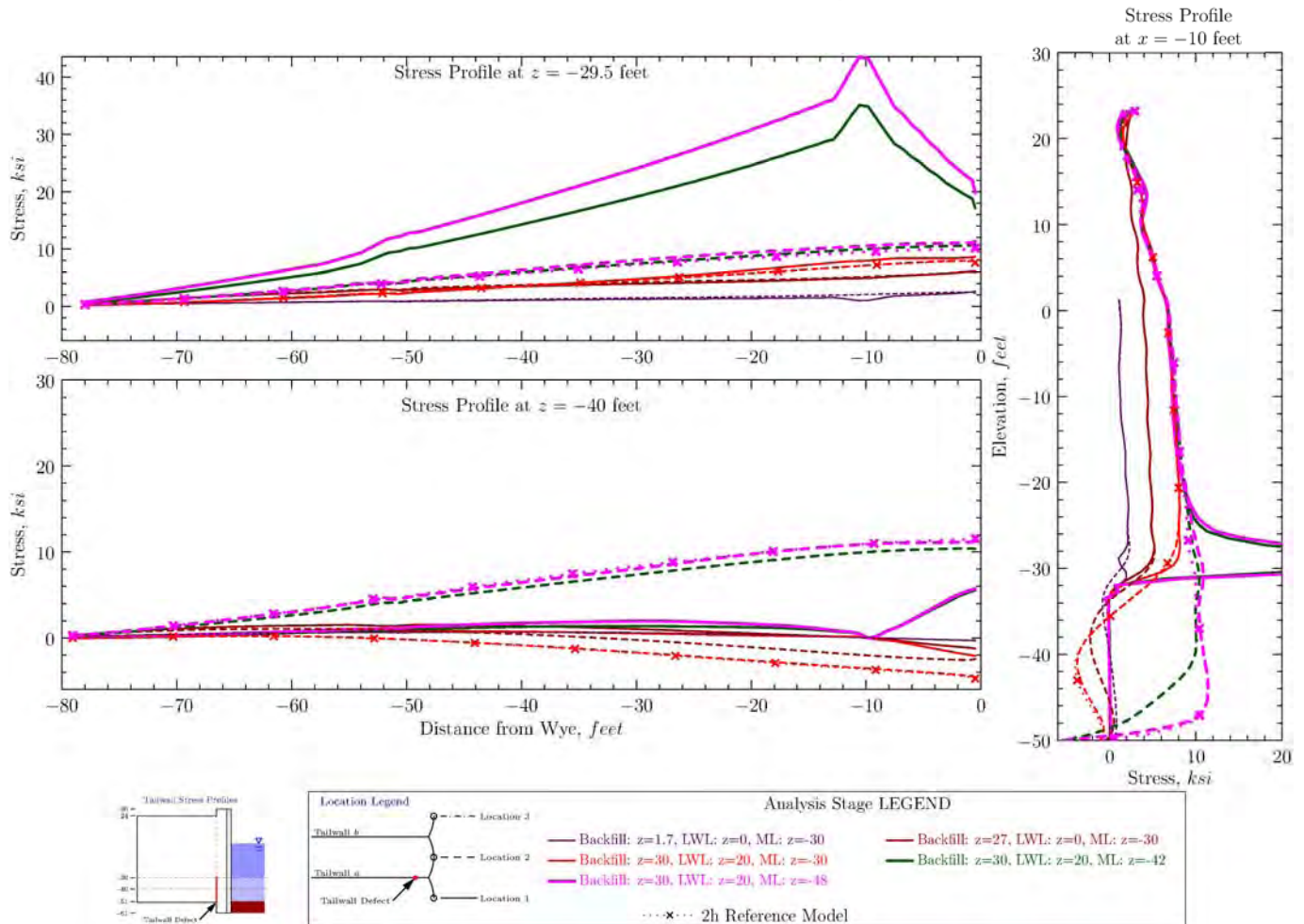


Figure G-2.18. Tailwall Horizontal (Hoop) Stresses from Long Tailwall Tear Defect Model

Tail Wall Horizontal Membrane Stress Profiles from *FLAC*<sup>3D</sup> local model  
 1w+2h defect model - Tailwall *a* tear defect at  $x=-12.7, z=-51.6$  to  $-40$

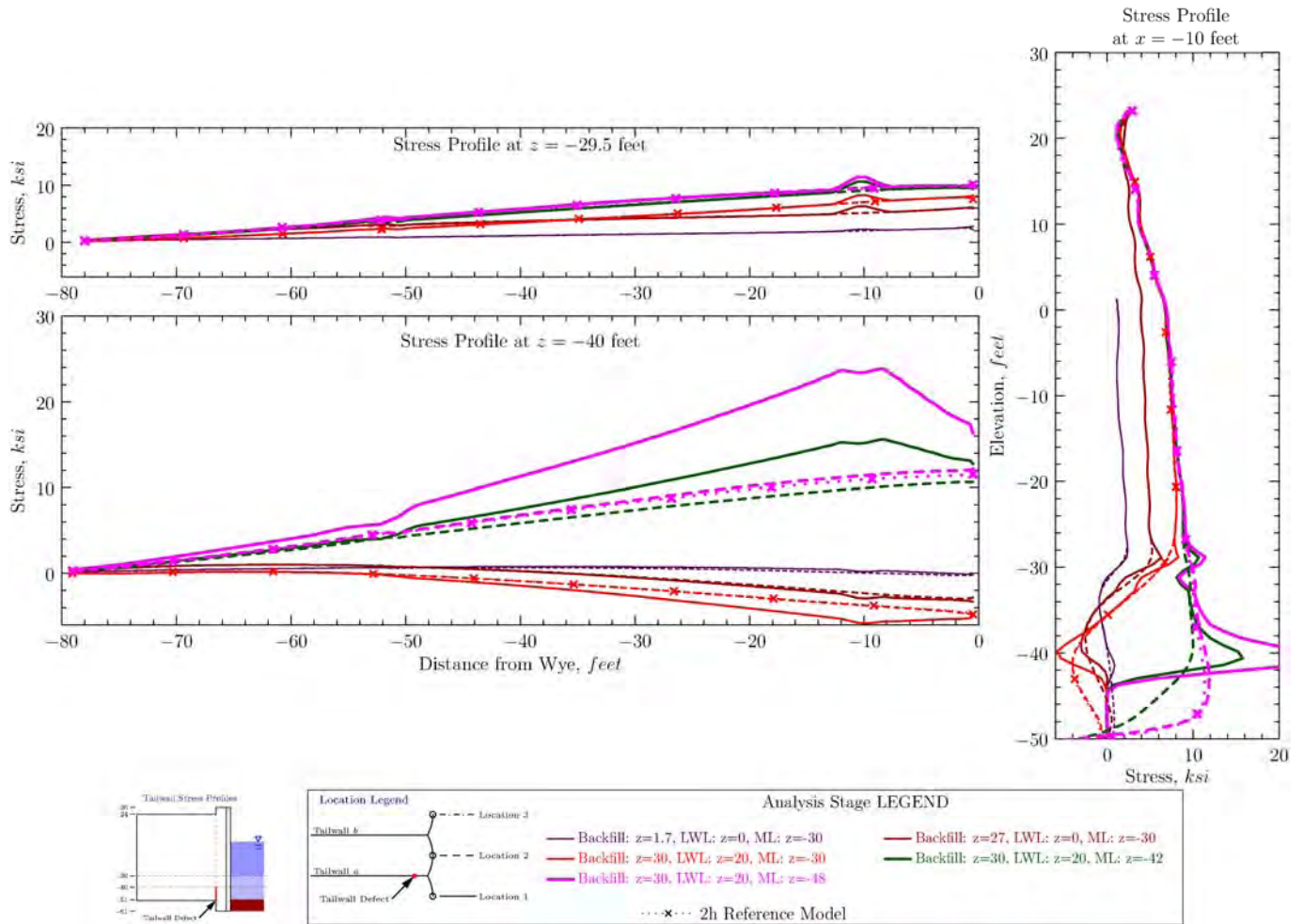


Figure G-2.19. Tailwall Horizontal (Hoop) Stresses from Intermediate Tailwall Tear Defect Model

Tail Wall Horizontal Membrane Stress Profiles from *FLAC*<sup>3D</sup> local model  
 1w+2h defect model - Tailwall *a* notch defect at x=-42.9,-41.4, z=-51.6,-29.6

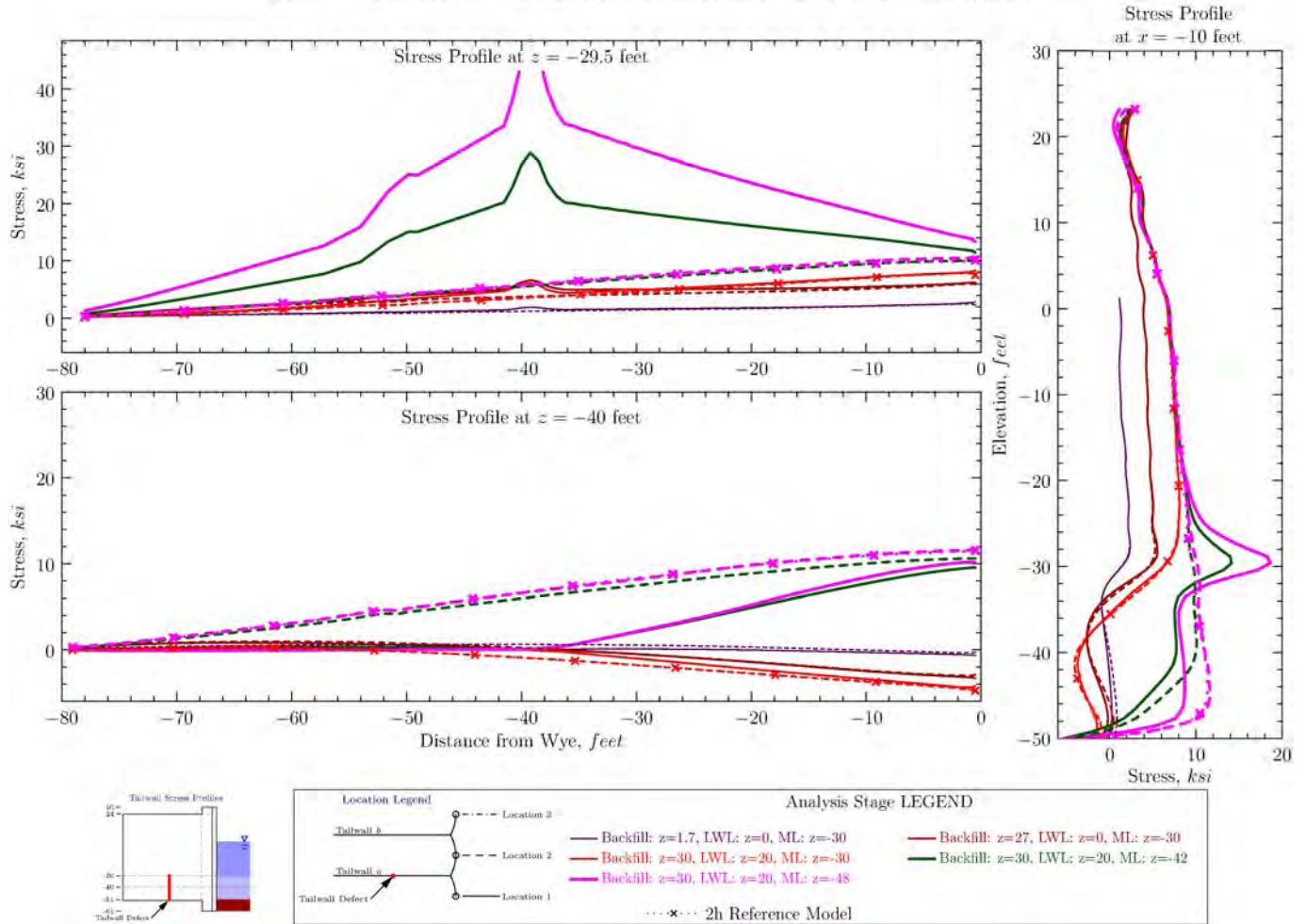


Figure G-2.20. Tailwall Horizontal (Hoop) Stresses from Long Tailwall Notch Defect Model

Tail Wall Horizontal Membrane Stress Profiles from *FLAC*<sup>3D</sup> local model  
 1w+2h defect model - Facewall tear defect at x=0, z=-61 to -29.6

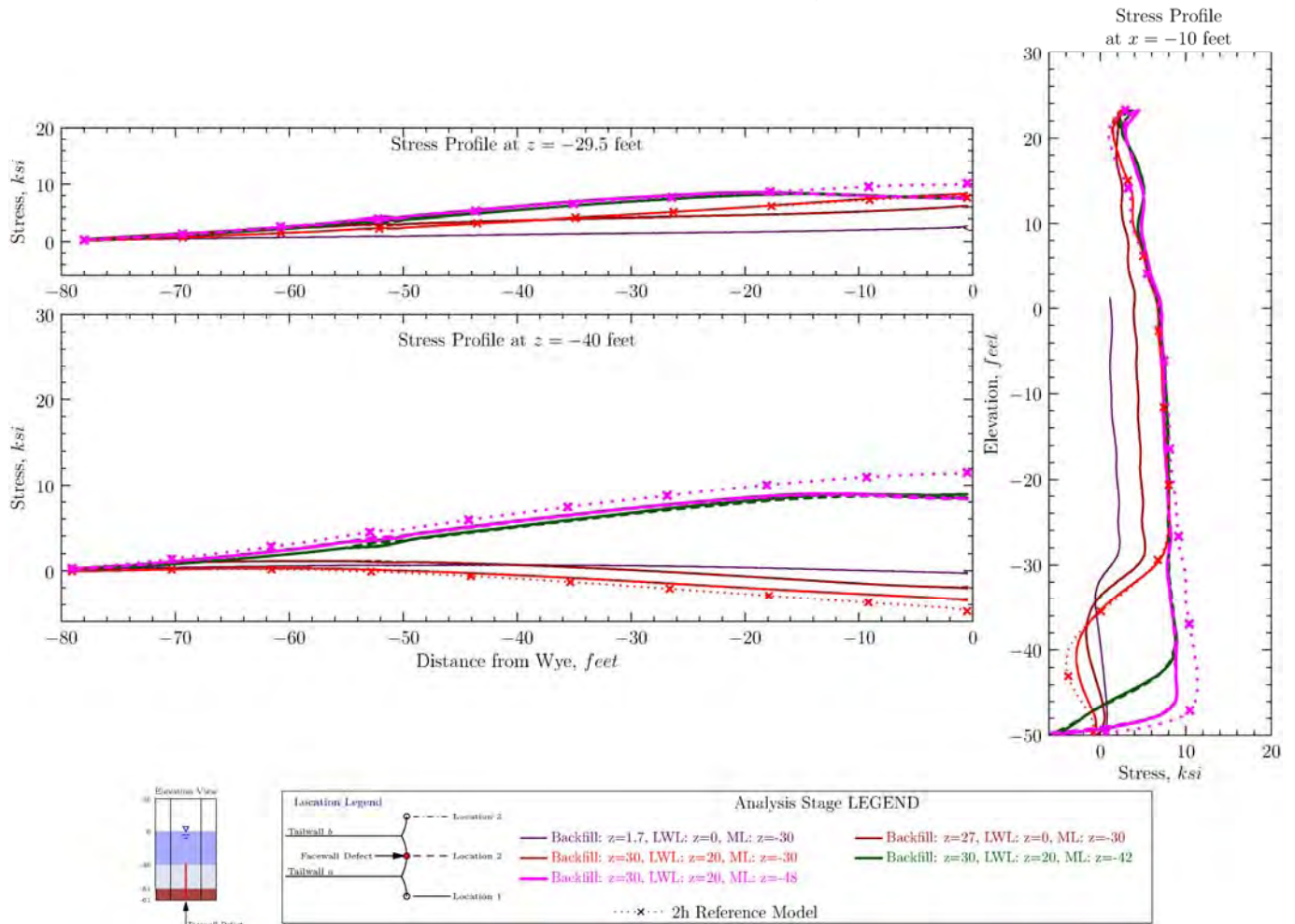


Figure G-2.21. Tailwall Horizontal (Hoop) Stresses from Long Facewall Tear Defect Model

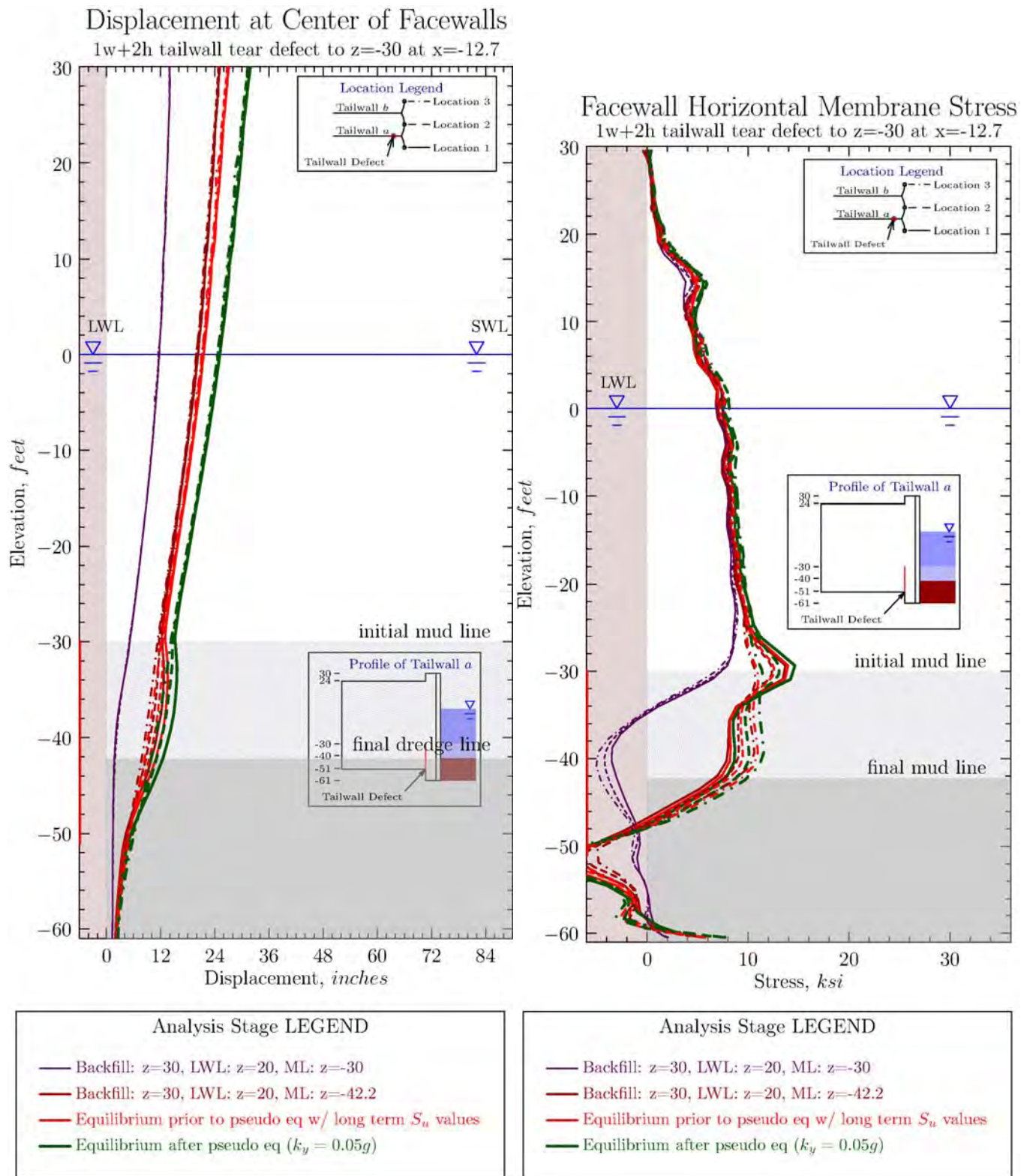


Figure G-2.22. Facewall Lateral Displacements and Hoop Stresses for Pseudo-Static Earthquake Load, Tailwall Tear Defect to -30 Feet Model

Tail Wall Horizontal Membrane Stress Profiles from *FLAC*<sup>3D</sup> local model  
 1w+2h tailwall tear defect to z=-30 at x=-12.7

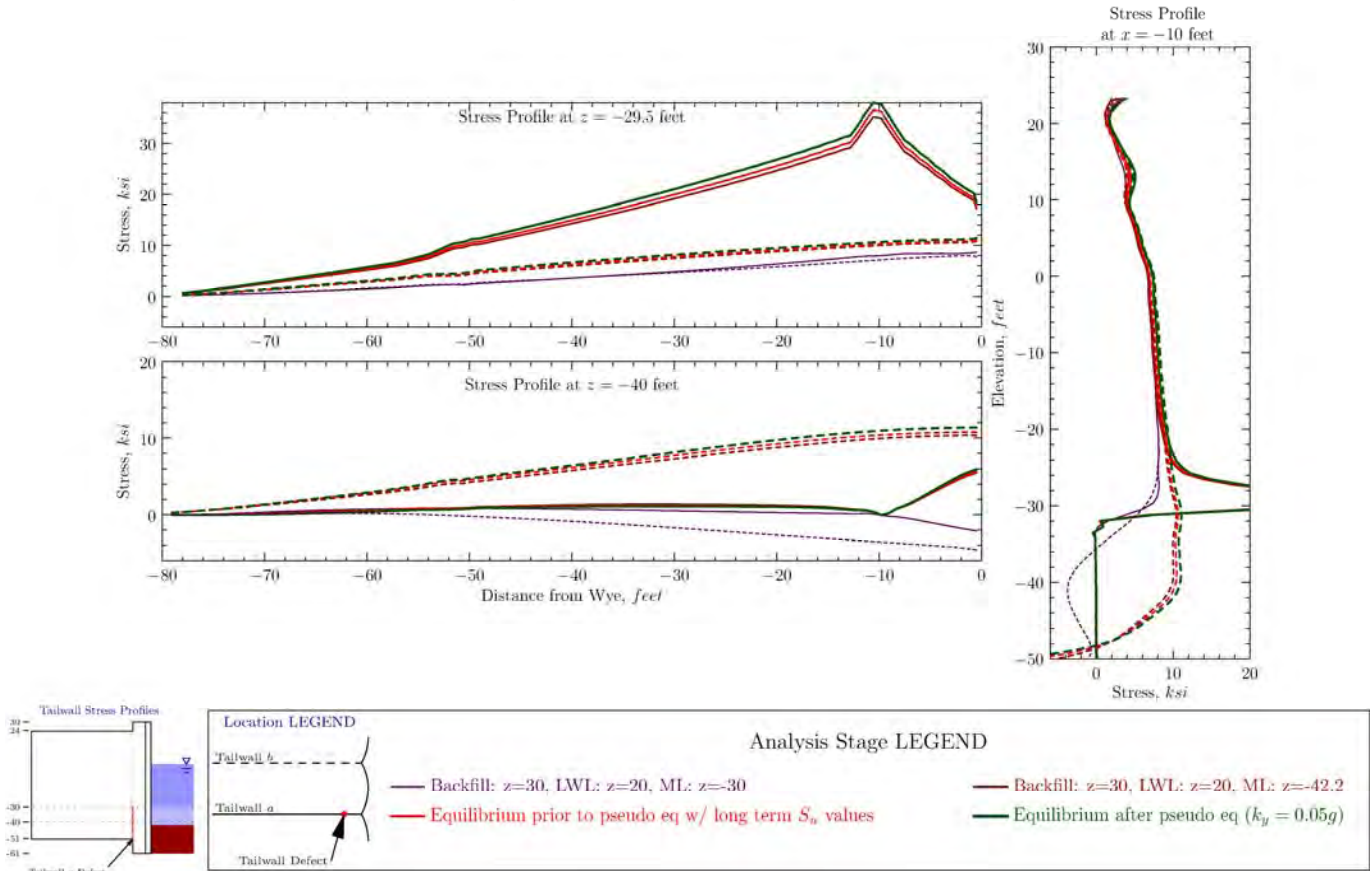


Figure G-2.23. Profiles of Tailwall Hoop Stresses for Pseudo-Static Earthquake Load, Tailwall Tear Defect to -30 Feet Model

